Experimental and machine learning tools to constrain pre-eruptive magmatic conditions and volcanoes with the potential for large-magnitude eruptions

Kyra S. Cutler

Department of Earth Sciences,
University of Oxford

A thesis submitted for the degree of
Doctor of Philosophy
Hilary Term 2025

Supervisors: Dr M. Cassidy and Prof. J. Blundy

Declaration of originality

I declare that the contents of this thesis are all my own work, except where otherwise stated. The views and interpretations expressed herein are mine and do not represent those of anyone else unless specifically stated.

Acknowledgements

I would like to thank my supervisors, Dr. Mike Cassidy and Prof. Jon Blundy, for their mentorship, guidance, and knowledge throughout my time at Oxford. I would also like to thank Matthew Beverley Smith, Steve Wyatt, James King, and Krzysztof Sokol for their assistance with all things lab-related and sample preparation. Additionally, I would like to thank Dr. Andrew Matzen for his support with electron microprobe analyses, Dr. Richard Brooker for his help with FTIR analyses, as well as Dr. John Craven and Dr. Cees-Jan de Hoog for their help in collecting SIMS data.

Abstract

This thesis aims to develop new or refined petrological tools (i.e., thermometry, barometry, and hygrometry) using plagioclase feldspars, with a secondary aim of exploring the factors (i.e., eruptive records, subduction zone characteristics, geochemistry, edifice morphology) that contribute to the generation of large-magnitude eruptions (M≥6).

Using random forest machine learning and a large compilation of plagioclase-bearing experimental petrology data (n = 1,152), new melt thermometers, hygrometers, barometers, and a plagioclase-melt equilibria model have been developed. Test set root mean square errors (RMSEs) for the T/H_2O-dependent and melt-only models are 25–35 °C, 0.65–1.00 wt.%, and 74–88 MPa for temperature, water content and pressure, respectively, while the test set RMSE for the plagioclase-melt equilibria model is 5.8 mol%. RMSEs for all melt models demonstrate greater prediction accuracy than earlier plagioclase-melt thermobarometers and hygrometers. In addition, the plagioclase-melt equilibria model enables straightforward calculation of equilibrium anorthite contents, irrespective of melt water content. Models can be easily used through the R scripts or the web application at https://github.com/kyra-cutler/Plag-saturated-melt-P-T-H2O-An.

Experiments were performed in cold seal pressure vessels at 780–850 °C at low pressures (<200 MPa) and variable water contents (<6.0 wt.%), using a haplogranitic starting material to determine hydrogen plagioclase-melt partition coefficients for silicic melts. Experimental plagioclase and glass were analysed by Secondary Ion Mass Spectrometry, with the resulting hydrogen partition coefficients ranging from 0.002 to 0.008 (± 0.001). Combined with literature data, these hydrogen partition

coefficients show a strong dependence on the H_2O content in the melt that can be described using a power-law relation ($D_{H_2O}^{plagioclase/melt} = 0.0071 \cdot C_{H_2O}^{melt^{-0.80}}$), resulting in non-Henrian behaviour between H_2O concentrations in plagioclase and the melt. Rearranging the equation to calculate melt H_2O contents forms a new H^+-in-plagioclase hygrometer ($C_{H_2O}^{melt} = (\frac{C_{H_2O}^{plagioclase}}{0.0071})^5$) that can be applied to lunar and terrestrial melts with water contents of 0.005–6.0 wt.%.

Given their potential environmental and socioeconomic impacts, identifying the factors that could contribute to high-magnitude eruptions is crucial for forecasting and hazard management. This aim is addressed using a data-driven approach. A dataset of 150 arc volcanoes with 22 variables (eruptive records, subduction zone characteristics, geochemistry, and edifice morphology) has been compiled to calibrate a classifier to predict whether a volcano has experienced a prior M≥6 eruption. The gradient-boosting machine algorithm produces the most effective model with a test set accuracy of 70%. The accurately classified volcanoes (i.e., true positives; n_{total} = 43) from the test sets indicate that larger, more mature volcanic systems exhibiting greater geochemical variability may act as proxies for the size, distribution, and thermal maturity of underlying magmatic systems. A hierarchical clustering analysis was performed using the true positive volcanoes to identify analogue volcanoes with similar characteristics. This produced a combined list of 64 volcanoes, derived from the true positive volcano list and clustering, which could be explored further to enhance short-term eruption forecasting and hazard assessments.

List of contents

Declaration	2
Acknowledgements	3
Abstract	4
List of figures	9
List of tables	10
Chapter 1: Introduction	11
1.1 Importance of temperature, pressure, and water	11
1.1.1 Plagioclase thermobarometry and hygrometry	13
1.1.2 Direct methods to determine melt H_2O concentrations	15
1.2 Large-magnitude eruptions	16
1.3 Machine learning	17
1.4 Aims and thesis structure	21
Chapter 2: Plagioclase-saturated melt hygrothermobarometry and plagioclase-melt equilibria using machine learning	41
Abstract	42
2.1 Introduction	43
2.2 Developing hygrothermobarometric and anorthite content models	46
2.2.1 Dataset compilation and filtering	46
2.2.2 Calibration range	47
2.2.3 Model training and cross-validation	50
2.3 P-T-H_2O-An models	51
2.3.1 Model calibration and validation	51
2.3.2 Thermometry	56
2.3.3 Hygrometry	57
2.3.4 Barometry	63
2.3.5 Anorthite content	64

2.3.6 Plagioclase saturation	65
2.3.7 Further model limitations	72
2.4 Model application	73
2.4.1 May–October 1980 eruption, Mount St Helens, USA	74
2.4.2 2014–2015 Holuhraun eruption, Bárðarbunga, Iceland	78
2.5 Conclusion	83
Supplementary Materials for Chapter Two	96
Chapter three: Experimental insights into the partitioning behaviour of hydrogen between plagioclase and melt	106
Abstract	106
3.1 Introduction	107
3.2 Experimental and analytical methods	109
3.2.1 Starting material	109
3.2.2 Secondary Ion Mass Spectrometry (SIMS)	115
3.2.3 Fourier Transform Infrared Spectroscopy	117
3.2.4 Electron Probe Microanalysis	119
3.3 Results	121
3.3.1 Experimental phases and major element compositions	121
3.3.2 H_2O contents of experimental glass and plagioclase	121
3.4 Discussion	124
3.4.1 Controls on hydrogen plagioclase-melt partitioning	124
3.4.2 Magmatic water contents estimated from Cerro Machín…	133
3.5 Conclusion	137
Chapter four: Identifying volcanoes with the potential for large-magnitude eruptions using supervised and unsupervised machine learning	149
Abstract	149
4.1 Introduction	150

4.2 Datasets and statistical methods	152
4.2.1 Dataset compilation and pre-processing	152
4.2.2 Classification workflow	155
4.2.3 Agglomerative hierarchical clustering	157
4.3 Results	158
4.3.1 Feature selection	158
4.3.2 Classification model performance	159
4.3.3 Analogues from clustering	164
4.4 Discussion	173
4.4.1 Criteria for volcanoes with large-magnitude eruption potential	173
4.4.2 Analogue volcanoes	176
4.5 Conclusion	178
Chapter five: Conclusions and future work	188
5.1 Machine learning-based thermobarometric and hygrometric models	188
5.2 Using plagioclase as a NAM hygrometer	190
5.3 Refining volcano candidates for future large-magnitude eruptions	193

List of figures

Figure 2.1	Calibration range of compiled plagioclase-saturated experiments…	48
Figure 2.2	Raincloud comparison plots of cross-validation RMSEs from the…	53
Figure 2.3	Plots of variable importance versus input variable for the H_2O-…	54
Figure 2.4	Examples of testing set performance for the melt-only models and…	59
Figure 2.5	Examples of testing set performance for the melt models with…	61
Figure 2.6	Testing set performance using other plagioclase-melt or melt models…	67
Figure 2.7	Monte Carlo simulations of electron microprobe analytical errors…	68
Figure 2.8	Investigation of appropriate filters for all testing set P-T-H_2O-An…	70
Figure 2.9	**a**) Filtered temperature (°C) vs. pressure (MPa) predictions of melt…	81
Figure 2.10	**a**) Stacked histogram displaying the composition of plagioclase…	82
Figure 3.1	Calibration curve for the April 2024 SIMS session.	117
Figure 3.2	SEM images of experimental runs. (a) HL_CoGL08 is a charge with dry...	120
Figure 3.3	Hydrogen partition coefficients obtained from experiments and…	125
Figure 3.4	Hydrogen partition coefficients versus fO2. fO_2 values recalculated to…	126
Figure 3.5	H_2O contents in hydrated plagioclase crystals (weight ppm of H_2O) and..	128
Figure 3.6	Power-law regression of water fugacity versus H_2O in plagioclase (ppm)..	131
Figure 3.7	Comparison of H_2O content values from H^+-in-plagioclase hygrometry,…	136
Figure 4.1	Distribution of arc volcanoes compiled in both datasets. world map…	154
Figure 4.2	Median accuracy scores of all 30 recursive feature elimination runs for…	159
Figure 4.3	Cross-validation training (**a**) and test set accuracy (**b**) scores for the…	163
Figure 4.4	Test set precision (**a**), recall (**b**), and F1 scores (**c**) for the random forest..	163
Figure 4.5	Raincloud plots illustrate the variation in the number of Pleistocene…	167
Figure 4.6	Dendrogram generated from agglomerative hierarchical clustering…	172
Figure 4.7	Distribution of volcanoes with the potential for large-magnitude eruptions..	175

List of tables

Table 1.1	Examples of machine learning applications in petrology. A reference…	20
Table 3.1	Experimental starting materials for hydrogen partitioning runs and…	111
Table 3.2	Compositions of experimental plagioclase seeds and plagioclase SIMS…	113
Table 3.3	Experimental run conditions, run products, and SIMS data of glass and…	114
Table 3.4	EPMA of glasses.	122
Table 3.5	EPMA of crystallised plagioclase.	123
Table 4.1	Results of recursive feature elimination. All 22 features are ranked in…	162
Table 4.2	Volcanoes classified as true positives (i.e., volcanoes with a prior M≥6…	165
Table 4.3	Volcanoes classified as false positives (i.e., volcanoes predicted to…	168
Table 4.4	Volcanoes classified as true negatives (i.e., volcanoes with no record…	169
Table 4.5	Volcanoes classified as false negatives (i.e., volcanoes with a prior ...	171

1 | Introduction

1.1 Importance of temperature, pressure, and water

An estimated 1 billion people reside within 100 km of an active volcano (Freire et al., 2019), highlighting the importance of monitoring volcanoes to forecast the onset of activity and mitigate associated risks. Arc volcanism is especially hazardous due to the wide variety of eruption styles observed (e.g., Brown et al., 2017). During a single eruption, shifts in eruption style (i.e., effusive to explosive or vice versa) are primarily driven by changes in shallow processes such as vesiculation, crystallisation, and outgassing (e.g., Boudon et al., 2008; Cioni et al., 2008); transitions in style across multiple eruptions, with observed repose periods, may indicate evolving conditions in magma storage and initial ascent (e.g., Cassidy et al., 2018). A now widely accepted model of magma storage in arc volcanoes is that magma resides within a mush system. This is supported by geophysical observations indicating that the quantity of silicate melt in the crust is relatively low (<15%; Magee et al., 2018; Ward et al., 2014; Paulatto et al., 2022), suggesting that melt-rich bodies are ephemeral and magma is predominantly stored as crystal mush (Cashman et al., 2017). These mush systems form through repeated intrusions of melt from depth and consist of a crystalline framework interlaced with melt containing dissolved volatiles, which are distributed in varying amounts throughout the crystal network (e.g., Annen et al., 2006; Cashman and Sparks, 2013; Sparks et al., 2019; Weinburg et al., 2021). The crystalline components of the mush are deformable, enabling melt and fluids to segregate within the system (McKenzie, 1984; Solano et al., 2012), with the strength of the crystalline framework depending on the melt fraction, which increases as the melt fraction decreases (Rosenberg and Handy, 2005). The shift from crystal mush to an eruptible magma takes place over a narrow

crystal content range (Caricchi et al., 2007; Burgisser and Bergantz, 2011; Sparks et al., 2019). The energy needed to remobilise a crystal mush depends on its initial melt content, with higher initial melt levels requiring less energy (Bachmann and Bergantz, 2006; Bergantz et al., 2017). The main drivers behind crystal mush remobilisation are considered to be magma recharge and the exsolution and migration of volatiles (e.g., Scandone et al., 2007; Rubin et al., 2017; Jackson et al., 2018; Humphreys et al., 2025). By constraining the conditions of magmatic storage and transport—specifically temperature (T), pressure (P), and water (H_2O) content —and examining how these variables evolve over time and space, we can improve our understanding of magma storage and eruptive dynamics, as well as build a better framework for developing realistic eruption scenarios for hazard assessments.

Estimating temperature reveals the thermal state and evolution of magmatic systems, serving as a key input for determining specific magmatic parameters. This includes determining the timescales of eruptive processes by analysing chemical gradients in crystal phases (i.e., diffusion chronometry; Costa et al., 2020), estimating the water content of melts (i.e., hygrometry; Waters and Lange, 2015), or the pressure (and therefore depth) at which magma occupies the lithosphere (e.g., Neave and Putirka, 2019). The latter provides a valuable spatial constraint that can be integrated with geophysical observations of plumbing systems, along with signs of ongoing unrest such as ground deformation, degassing, and seismicity (e.g., Edmonds, 2008; Greenfield et al., 2016; Hudson et al., 2017).

H_2O is the most prevalent volatile component in silicate melts, significantly influencing the physical and chemical characteristics of magma as it migrates from the mantle to the upper crust. It plays a critical role in generating arc magmas, where water drives melting by reducing the solidus temperature of the mantle (e.g., Asimow

and Langmuir, 2003; Grove et al., 2006; Kelley et al., 2010). The presence of water also influences the stability fields of various minerals, thereby affecting the liquid line of descent of evolving magmas (e.g., Sisson and Grove, 1993; Grove et al., 2003; Zimmer et al., 2010). At low pressures, water solubility decreases, driving the exsolution of H_2O from the melt to form a vapour phase (e.g., Baker and Aletti, 2012). This exsolution leads to the polymerisation of the melt structure, increasing melt viscosity and decreasing the bulk magma density (e.g., Dingwell et al., 1996). The interplay between water exsolution, changes to magma rheology, and volatile outgassing during ascent all play a key role in determining eruption style (e.g., Cassidy et al., 2018). Many external signs of volcanic systems, such as ground deformation and seismicity, can also be linked to changes in magmatic water content. For example, numerical models show that magmas at their H_2O solubility limit, along with those containing low CO_2 levels, generate the highest exsolution-driven overpressures; these magmas have great potential to trigger eruptions by promoting faster initial ascent rates, hindering efficient degassing, and encouraging explosive activity (Brookfield et al., 2023). In addition, magmas with higher water content increase their system compressibility and induce fluid exsolution, resulting in less ground deformation observed at arc volcanoes (Yip et al., 2022).

Given the fundamental role that temperature, pressure, and water content all play in controlling volcanic processes, quantifying these factors remains a vital objective in volcanology. Petrological analysis of rocks and minerals provides the most versatile method for determining T/P/H_2O conditions, and refining or developing existing techniques is the primary focus of this thesis.

1.1.1 Plagioclase thermobarometry and hygrometry

Records of crystallisation temperatures, pressures, and water contents can be obtained from various igneous crystal phases and/or melts saturated with specific minerals, as the major-element chemistry of crystals and melts serves as an archive of their crystallisation conditions. Plagioclase feldspar, defined by the general formula $(NaCa)(Al_{1-2})(Si_{2-3})O_8$, is commonly used to reconstruct crystallisation conditions across various tectonic settings, as it saturates in magmas across a wide bulk compositional range (e.g., Blatter et al., 2013; Melekhova et al., 2015; Ulmer et al., 2018; Marxer et al., 2023). Experimental studies on plagioclase-melt equilibria have highlighted that the composition of plagioclase depends on: 1) melt composition, especially the H_2O content, where higher H_2O concentrations in magma lower the liquidus temperature of plagioclase (e.g., Housh and Luhr 1991; Sisson and Grove 1993; Panjasawatwong et al. 1995; Lange et al. 2009; Feig et al. 2010); 2) the crystallisation temperature, as elevated temperatures favour the crystallisation of calcium-rich plagioclase (Kudo and Weill 1970; Lange et al. 2009), and 3) the pressure of crystallisation (e.g., Panjasawatwong et al. 1995; Longhi et al. 1993), where the stability field of plagioclase expands as magma ascends, resulting in decompression-driven crystallisation (e.g., Hammer et al., 2002; Riker et al., 2015). Collectively, these controls significantly influence the differentiation pathways of magmas, with calc-alkaline magmas often exhibiting plagioclase fractionation later in their evolution, contributing to Fe depletion and oxidation (Sisson and Grove, 1993). In contrast, tholeiitic magmas tend to show early plagioclase saturation and Fe enrichment (Grove and Baker, 1984). The chemical sensitivity of plagioclase has resulted in the development of several plagioclase-melt hygrometers, thermometers, and barometers, which are based on the plagioclase-melt exchange reaction

of albite (Ab; $NaAlSi_3O_8$) and anorthite (An; $CaAl_2Si_2O_8$) components (e.g., Lange et al., 2009; Waters and Lange, 2015; Putirka, 2008). The primary limitations of plagioclase-melt hygrometers and thermobarometers relate to the assessment of equilibrium (e.g., Putirka, 2008) and require at least one independent constraint for T, P, or H_2O to derive estimates, which can often lead to higher uncertainties if errors are not propagated (Wieser et al., 2024). Creating models that do not rely on other intensive parameters (T, P, or H_2O) would significantly help to provide estimates with smaller error margins. With the wide range of plagioclase-bearing experiments now available, there is an opportunity to refine models.

1.1.2 Direct methods to determine melt H_2O concentrations

Melt inclusions (MIs) are the most popular direct technique for measuring H_2O; they act as small archives (1–100 μm in diameter) of entrapped melt during crystal growth (e.g., Kent, 2008) and may preserve the original H_2O content of the magma. However, melt inclusions may undergo various modification processes, including post-entrapment crystallisation (PEC), vapour bubble formation, vapour leakage, elemental diffusion at the host mineral/MI interface, and boundary layer processes (e.g., Bulcholz et al., 2013; Maclennan, 2017). Additionally, the availability and size of melt inclusions often limit the scope of analysis. An alternative approach is to constrain H_2O concentrations by directly measuring hydrogen (H^+) in hydrous minerals (e.g., apatite; Humphreys et al., 2021; Li et al., 2021) or in nominally anhydrous minerals (NAMS; e.g., Radu et al., 2023). In the case of NAMs, these minerals contain trace concentrations of hydrogen as structural defects within their crystal lattices, and this can be related to melt H_2O content if the relevant mineral-melt partition coefficients have been experimentally constrained (i.e., garnet, olivine, clinopyroxene, plagioclase). However, NAMs can be challenging to measure due to

the lack of well-defined standards (e.g., Kumamoto et al., 2017) and re-equilibration resulting from rapid hydrogen diffusion, which destroys the primary H_2O content record (e.g., Demouchy et al., 2006). Previous experimental studies have focused on establishing constraints on hydrogen partitioning coefficients for minerals such as clinopyroxene and olivine (e.g., O'Leary et al., 2010; Peterson et al., 2025). However, since plagioclase exhibits slower hydrogen diffusivity (Johnson and Rossman, 2013), conducting new experiments to investigate plagioclase hydrogen partitioning offers an opportunity to broaden its application.

1.2 Large magnitude eruptions

The size of an eruption can be classified using the magnitude scale, which uses a logarithmic index to describe explosivity based on erupted mass (magnitude = $\log_{10}$ (erupted mass in kg) – 7; Pyle, 2015). Explosive eruptions of large magnitude (M≥6) pose catastrophic risks to local environments and can cause temporary global climate impacts due to the extensive ejection of volcanic material. For instance, the 1991 Mount Pinatubo eruption (M6.1) in the Philippines ejected approximately 5 km³ of magma and is one of the largest eruptions recorded in the past 100 years (Newhall et al., 1998). This eruption and its aftermath, particularly the lahars during the monsoon season, caused significant socioeconomic impacts, totalling 12 billion pesos ($443 million; Mercado et al. 1996), affecting millions and damaging infrastructure, agriculture, and livelihoods in Central Luzon. In addition, the eruption was associated with the release of over 12 Tg of SO_2 into the stratosphere (Bluth et al., 1997; Fisher et al., 2019), which converted into sulphate aerosol, causing a decrease in global temperatures of 0.5 °C for the following 2–3 years (Hansen et al., 1992; Minnis et al., 1993). Although these high-magnitude eruptions are powerful

events, they occur infrequently—about once every 110 years for M6, every 1,200 years for M7, and roughly every 17,000 years for M8 eruptions (Rougier et al., 2018). These highly explosive magmatic events, known as Plinian eruptions, are often linked with highly silicic magmas and are characterised by high magma discharge rates and pyroclastic material rich in bubbles (e.g., Walker, 1981; Gardner et al., 1996). There is increasing consensus that large silicic magmatic systems exist as vertically extensive and predominantly crystalline mush states (e.g., Cashman et al., 2017), from which melts are extracted and transported into shallower melt bodies as precursors to silicic eruptions (e.g., Wilson et al., 2021). Furthermore, many volcanic systems that have undergone large-magnitude eruptions and caldera formation have experienced this process multiple times throughout their eruptive histories, leading to the hypothesis that these volcanic systems undergo caldera cycles, which include pre-collapse activity, caldera formation, post-collapse resurgence, and recovery (Maisonneuve et al., 2021). Large-magnitude, caldera-forming eruptions have not yet been monitored using modern geophysical methods. However, based on experience with more minor large-magnitude explosive eruptions (e.g., Pinatubo in 1991), short-term warning signals (e.g., increased degassing, surface deformation, seismic activity) are likely to be detected (e.g., Girona et al., 2021). Identifying proxies for underlying magmatic systems that have experienced M≥6 eruptions could improve monitoring strategies for potential M≥6 eruptions, particularly in regions of heightened vulnerability to volcanic risk (Cassidy and Mani, 2022).

1.3 Machine learning

Machine learning is a subfield of artificial intelligence (AI) that involves creating algorithms and statistical models that enable computers to perform specific tasks

without explicit instructions, instead relying on data-driven insights and inferences (Bishop, 2006; Zhou, 2021). Over the past few decades, machine learning has been widely adopted across various scientific disciplines. In the geosciences, it has been applied in many fields such as geophysics (e.g., Falcin et al., 2021; Manley et al., 2021), remote sensing (e.g., Cracknell and Reading, 2014; Mohan et al., 2021), and palaeobiology (e.g., Matthews et al., 2018; Romero et al., 2020; Wills et al., 2021). However, machine learning has only recently been applied to datasets in igneous petrology; Table 1.1 summarises the various petrological applications using machine learning.

In the learning process, where a machine learning model acquires knowledge and improves its performance on a specific task over time (Hastie et al., 2009), two main approaches can be used, depending on the data available: supervised and unsupervised learning. Supervised learning algorithms are always trained on labelled datasets and are primarily used for regression or classification tasks. The goal of regression tasks is to use an algorithm to predict a continuous value (e.g., the pressure of mineral formation based on mineral composition; Jorgenson et al., 2022), while classification aims to predict a class label (e.g., the type of volcanic ash particle based on images; Benet et al., 2024). Unsupervised learning uses algorithms to analyse and cluster unlabelled datasets, identifying patterns within the data without external guidance. It is predominantly used for two tasks in petrology: clustering and dimensionality reduction. Clustering aims to group unlabelled data according to similarities or differences, (e.g., correlating macrotephra layers within a stratigraphy based on tephra major element glass chemistry and the componentry of ash particles; Liu et al., 2015), whereas dimensionality reduction minimises the number of data inputs to a manageable size while preserving data integrity (e.g.,

identifying differentiation processes using principal component analysis; Ueki and Iwamori, 2017).

Table 1.1. Examples of machine learning applications in petrology. A reference manuscript is provided for each algorithm.

Topic	Aim	Algorithm(s)	Data input	References
Thermobarometry	Estimation pre-eruptive temperatures and magma storage depths	Random forest (Breiman, 2001); gradient boosting (Friedman, 2002); decision trees (Breiman et al., 1984); K-nearest neighbours (Bentley, 1975); extremely randomised trees (Simm et al., 2014)	Major element mineral and/or melt composition	E.g., Petrelli et al., 2020; Higgins et al., 2022; Jorgenson et al., 2022; Thomson et al., 2021; Li and Zhang, 2022; Weber and Blundy, 2024
Thermodynamics	Estimation of melt and glass properties	Grey-box neural network (Willard et al., 2020)	Melt composition	E.g., Le Losq et al., 2021; Le Losq and Baldoni, 2023
Tephra correlation	Classification of volcanic source from geochemical data	Ensemble models (Kittler & Roli, 2000)	Major & trace element melt composition	E.g., Bolton et al., 2020; Lubbers et al., 2023
Volcanic rock nomenclature	Classification of volcanic rocks	Random forest (Breiman, 2001)	Trace element melt composition	E.g., Lang et al., 2023
Characterisation of eruptive record	Identification of compositional patterns within crystal cargoes	Hierarchical cluster analysis (Köhn and Hubert, 2014)	Major element mineral composition	E.g. Boschetty et al., 2022; Costa et al., 2023; Musu et al., 2023
Textural studies	Image segmentation for crystal size distribution	Convolutional neural network (Qiao et al., 2021); random forest (Breiman, 2001)	Thin section images	E.g., Toth and Maclennan, 2024; Lormand et al., 2018
Componentry	Classification of volcanic ash particles	Gradient boosting (Chen and Guestrin, 2016)	Binocular microscope images	E.g., Benet et al., 2024

1.4 Aims and thesis structure

This thesis aims to develop new or refined petrological tools (i.e., thermometry, barometry, and hygrometry) using plagioclase feldspars. A secondary aim looks to explore the factors (i.e., eruptive records, subduction zone characteristics, geochemistry, edifice morphology) that contribute to producing large-magnitude eruptions (M≥6). A brief overview of each chapter is provided below.

Chapter Two: *Plagioclase-saturated melt hygrothermobarometry and plagioclase-melt equilibria using machine learning* tests whether existing plagioclase-based thermobarometers, hygrometers and plagioclase-melt equilibria models can be refined using supervised machine learning. To achieve this, a database of plagioclase-bearing experimental data was compiled and filtered, then used to calibrate several models to predict the T, P, and H_2O content of melts and the equilibrium anorthite content of plagioclase. Two versions of a thermometer, a hygrometer and a barometer were tested using a plagioclase-melt or a melt-only compositional input. Models are then applied to two eruption case studies of Mount St Helens (1980; USA) and Holuhraun (2014-2015; Iceland) to compare the results of the new plagioclase-saturated melt models with estimates derived from other petrological or geophysical methods.

Chapter Three: *Experimental insights into the partitioning behaviour of hydrogen between plagioclase and melt* aims to determine new hydrogen partition coefficients between plagioclase and highly silicic melts. Partitioning experiments were conducted under various P-T-H_2O conditions on a haplogranitic starting material. Hydrogen was analysed in the experimental glass and plagioclase using Secondary

Ion Mass Spectrometry (SIMS). From the compilation of our experimental and literature data, two empirical equations are proposed to calculate the melt water concentrations of equilibrium melts based on measured H_2O values from plagioclase crystals. One of the empirical hygrometers is tested on plagioclase crystals from the dacitic deposits of Cerro Machín volcano (Colombia; Castilla et al., 2024) to compare the estimates of melt water content with previous H^+-in-plagioclase hygrometers; the T-independent melt hygrometer from Chapter Two, and plagioclase- and quartz-hosted melt inclusions.

Chapter Four: *Identifying volcanoes with the potential for large-magnitude eruptions using supervised and unsupervised machine learning* explores what factors could contribute to large-magnitude eruptions and develops a list of volcano candidates that could produce a large-magnitude eruption in the future. A dataset of 150 arc volcanoes was compiled, featuring different variables such as subduction zone characteristics, geochemistry, edifice morphometry, and eruptive records. Recursive feature elimination was used to identify the optimal variables that produced the best model for classifying volcanoes that had experienced prior M≥6 eruptions. Two supervised classification machine learning algorithms (random forest and gradient boosting machine) were tested and refined to determine which one provides the most effective performance. Using the correctly classified volcanoes (i.e., those with prior M≥6 eruptions) from the classifier test sets, we apply hierarchical clustering to determine analogue volcanoes with similar characteristics, generating a list of volcano candidates that could be investigated further to aid hazard assessments.

Chapter Five summarises the key findings of this thesis and highlights possible directions for future research based on the work presented in this thesis.

References

Annen, C., Blundy, J. D., & Sparks, R. S. J. (2006). The genesis of intermediate and silicic magmas in deep crustal hot zones. *Journal of petrology*, *47*(3), 505-539. DOI: https://doi.org/10.1093/petrology/egi084

Asimow, P. D., & Langmuir, A. C. (2003). The importance of water to oceanic mantle melting regimes. *Nature*, *421*(6925), 815-820. DOI: https://doi.org/10.1038/nature01429

Bachmann, O., & Bergantz, G. W. (2006). Gas percolation in upper-crustal silicic crystal mushes as a mechanism for upward heat advection and rejuvenation of near-solidus magma bodies. *Journal of Volcanology and Geothermal Research*, *149*(1-2), 85-102. DOI: https://doi.org/10.1016/j.jvolgeores.2005.06.002

Baker, D. R., & Alletti, M. (2012). Fluid saturation and volatile partitioning between melts and hydrous fluids in crustal magmatic systems: The contribution of experimental measurements and solubility models. *Earth-Science Reviews, 114*(3-4), 298-324.

Benet, D., Costa, F., & Widiwijayanti, C. (2024). Volcanic ash classification through Machine Learning. *Geochemistry, Geophysics, Geosystems*, *25*(3), e2023GC011224. DOI: https://doi.org/10.1029/2023GC011224

Bentley, J. L. (1975). Multidimensional binary search trees used for associative searching. *Communications of the ACM*, *18*(9), 509-517.

Bergantz, G. W., Schleicher, J. M., & Burgisser, A. (2017). On the kinematics and dynamics of crystal-rich systems. *Journal of Geophysical Research: Solid Earth*, *122*(8), 6131-6159. DOI: https://doi.org/10.1002/2017JB014218

Bishop, C. M., & Nasrabadi, N. M. (2006). *Pattern recognition and machine learning* (Vol. 4, No. 4, p. 738). Springer.

Blatter, D. L., Sisson, T. W., & Hankins, W. B. (2013). Crystallization of oxidized, moderately hydrous arc basalt at mid-to lower-crustal pressures: implications for andesite genesis. *Contributions to Mineralogy and Petrology*, *166*(3), 861-886. DOI: https://doi.org/10.1007/s00410-013-0920-3

Bluth, G. J., Rose, W. I., Sprod, I. E., & Krueger, A. J. (1997). Stratospheric loading of sulfur from explosive volcanic eruptions. *The Journal of Geology*, *105*(6), 671-684.

Bolton, M. S., Jensen, B. J., Wallace, K., Praet, N., Fortin, D., Kaufman, D., & De Batist, M. (2020). Machine learning classifiers for attributing tephra to source volcanoes: an evaluation of methods for Alaska tephras. *Journal of Quaternary Science*, *35*(1-2), 81-92. DOI: https://doi.org/10.1002/jqs.3170

Boschetty, F. O., Ferguson, D. J., Cortés, J. A., Morgado, E., Ebmeier, S. K., Morgan, D. J., ... & Silva Parejas, C. (2022). Insights into magma storage beneath a frequently erupting arc volcano (Villarrica, Chile) from unsupervised machine learning analysis of mineral compositions. *Geochemistry, Geophysics, Geosystems*, *23*(4), e2022GC010333. DOI: https://doi.org/10.1029/2022GC010333

Boudon, G., Komorowski, J. C., Villemant, B., & Semet, M. P. (2008). A new scenario for the last magmatic eruption of La Soufrière of Guadeloupe (Lesser Antilles) in 1530 AD Evidence from stratigraphy radiocarbon dating and magmatic evolution of erupted products. *Journal of Volcanology and Geothermal Research*, *178*(3), 474-490. DOI: https://doi.org/10.1016/j.jvolgeores.2008.03.006

Breiman, L., Friedman, J., Olshen, R. A., & Stone, C. J. (1984). *Classification and regression trees*. Chapman and Hall/CRC.

Breiman, L. (2001). Random forests. *Machine learning*, *45*(1), 5-32.

Brookfield, A., Cassidy, M., Weber, G., Popa, R. G., Bachmann, O., & Stock, M. J. (2023). Magmatic volatile content and the overpressure 'sweet spot': Implications for volcanic eruption triggering and style. *Journal of Volcanology and Geothermal Research*, *444*, 107916. DOI: https://doi.org/10.1016/j.jvolgeores.2023.107916

Brown, S. K., Jenkins, S. F., Sparks, R. S. J., Odbert, H., & Auker, M. R. (2017). Volcanic fatalities database: analysis of volcanic threat with distance and victim classification. *Journal of Applied Volcanology*, *6*(1), 15. DOI: https://doi.org/10.1186/s13617-017-0067-4

Bucholz, C. E., Gaetani, G. A., Behn, M. D., & Shimizu, N. (2013). Post-entrapment modification of volatiles and oxygen fugacity in olivine-hosted melt inclusions. *Earth and Planetary Science Letters*, *374*, 145-155. DOI: https://doi.org/10.1016/j.epsl.2013.05.033

Burgisser, A., & Bergantz, G. W. (2011). A rapid mechanism to remobilize and homogenise highly crystalline magma bodies. *Nature*, *471*(7337), 212-215. DOI: https://doi.org/10.1038/nature09799

Caricchi, L., Burlini, L., Ulmer, P., Gerya, T., Vassalli, M., & Papale, P. (2007). Non-Newtonian rheology of crystal-bearing magmas and implications for magma ascent dynamics. *Earth and Planetary Science Letters*, *264*(3-4), 402-419. DOI: https://doi.org/10.1016/j.epsl.2007.09.032

Cashman, K. V., & Sparks, R. S. J. (2013). How volcanoes work: A 25-year perspective. *Bulletin*, *125*(5-6), 664-690. DOI: https://doi.org/10.1130/B30720.1

Cashman, K. V., Sparks, R. S. J., & Blundy, J. D. (2017). Vertically extensive and unstable magmatic systems: a unified view of igneous processes. *Science*, *355*(6331), eaag3055.

Casadevall, T. J., Delos Reyes, P. J., & Schneider, D. J. (1996). The 1991 Pinatubo eruptions and their effects on aircraft operations. *Fire and Mud: eruptions and lahars of Mount Pinatubo, Philippines*, 625-636.

Cassidy, M., Manga, M., Cashman, K., & Bachmann, O. (2018). Controls on explosive-effusive volcanic eruption styles. *Nature communications*, *9*(1), 2839. DOI: https://doi.org/10.1038/s41467-018-05293-3

Castilla, S. C., Newcombe, M. E., Piccoli, P. M., & Peterson, L. D. (2024). Crystals and melt inclusions record deep storage of superhydrous magma prior to the largest known eruption of Cerro Machín volcano, Colombia. *Journal of Petrology*, *65*(9), egae095. DOI: https://doi.org/10.1093/petrology/egae095

Cassidy, M., & Mani, L. (2022). Prepare now for big eruptions. *Nature*, *608*(7923), 469-71. DOI: https://doi.org/10.1038/d41586-022-02177-x

Chen, T., & Guestrin, C. (2016). XGBoost: A Scalable Tree Boosting System. *Proceedings of the 22nd ACM SIGKDD International Conference on Knowledge Discovery and Data Mining - KDD '16*, *1*(1), 785–794. DOI: https://doi.org/10.1145/2939672.2939785

Cioni, R., Bertagnini, A., Santacroce, R., & Andronico, D. (2008). Explosive activity and eruption scenarios at Somma-Vesuvius (Italy): towards a new classification scheme. *Journal of Volcanology and Geothermal Research*, *178*(3), 331-346. DOI: https://doi.org/10.1016/j.jvolgeores.2008.04.024

Costa, F., Shea, T., & Ubide, T. (2020). Diffusion chronometry and the timescales of magmatic processes. *Nature Reviews Earth & Environment*, *1*(4), 201-214. DOI: https://doi.org/10.1038/s43017-020-0038-x

Costa, S., Caricchi, L., Pistolesi, M., Gioncada, A., Masotta, M., Bonadonna, C., & Rosi, M. (2023). A data driven approach to mineral chemistry unveils magmatic processes associated with long-lasting, low-intensity volcanic activity. *Scientific Reports*, *13*(1), 1314. DOI: https://doi.org/10.1038/s41598-023-28370-0

Cracknell, M. J., & Reading, A. M. (2014). Geological mapping using remote sensing data: A comparison of five machine learning algorithms, their response to variations in the spatial distribution of training data and the use of explicit spatial information. *Computers & Geosciences*, *63*, 22-33. DOI: https://doi.org/10.1016/j.cageo.2013.10.008

Demouchy, S., Jacobsen, S. D., Gaillard, F., & Stern, C. R. (2006). Rapid magma ascent recorded by water diffusion profiles in mantle olivine. *Geology*, *34*(6), 429-432. DOI: https://doi.org/10.1130/G22386.1

Dingwell, D. B., Romano, C., & Hess, K. U. (1996). The effect of water on the viscosity of a haplogranitic melt under PTX conditions relevant to silicic volcanism. *Contributions to Mineralogy and Petrology, 124*, 19-28.

Edmonds, M. (2008). New geochemical insights into volcanic degassing. *Philosophical Transactions of the Royal Society A: Mathematical, Physical and Engineering Sciences, 366*(1885), 4559-4579.

Falcin, A., Métaxian, J. P., Mars, J., Stutzmann, É., Komorowski, J. C., Moretti, R., ... & Lemarchand, A. (2021). A machine-learning approach for automatic classification of volcanic seismicity at La Soufrière Volcano, Guadeloupe. *Journal of Volcanology and Geothermal Research*, *411*, 107151. DOI: https://doi.org/10.1016/j.jvolgeores.2020.107151

Feig, S. T., Koepke, J., & Snow, J. E. (2010). Effect of oxygen fugacity and water on phase equilibria of a hydrous tholeiitic basalt. *Contributions to Mineralogy and Petrology*, *160*(4), 551-568. DOI: https://doi.org/10.1007/s00410-010-0493-3

Fisher, B. L., Krotkov, N. A., Bhartia, P. K., Li, C., Carn, S. A., Hughes, E., & Leonard, P. J. (2019). A new discrete wavelength backscattered ultraviolet algorithm for consistent volcanic SO 2 retrievals from multiple satellite missions. *Atmospheric Measurement Techniques*, *12*(9), 5137-5153. DOI: https://doi.org/10.5194/amt-12-5137-2019

Freire, S., Florczyk, A. J., Pesaresi, M., & Sliuzas, R. (2019). An improved global analysis of population distribution in proximity to active volcanoes, 1975–2015. *ISPRS International Journal of Geo-Information*, *8*(8), 341. DOI: https://doi.org/10.3390/ijgi8080341

Friedman, J. H. (2002). Stochastic gradient boosting. *Computational Statistics & Data Analysis*, *38*(4), 367-378. DOI: https://doi.org/10.1016/S0167-9473(01)00065-2

Gardner, J. E., Thomas, R. M., Jaupart, C., & Tait, S. (1996). Fragmentation of magma during Plinian volcanic eruptions. *Bulletin of Volcanology*, *58*(2), 144-162. DOI: https://doi.org/10.1007/s004450050132

Girona, T., Realmuto, V., & Lundgren, P. (2021). Large-scale thermal unrest of volcanoes for years prior to eruption. *Nature Geoscience*, *14*(4), 238-241. DOI: https://doi.org/10.1038/s41561-021-00705-4

Greenfield, T., White, R. S., & Roecker, S. (2016). The magmatic plumbing system of the Askja central volcano, Iceland, as imaged by seismic tomography. *Journal of Geophysical Research: Solid Earth*, *121*(10), 7211-7229.

Grove, T. L., & Baker, M. B. (1984). Phase equilibrium controls on the tholeiitic versus calc-alkaline differentiation trends. *Journal of Geophysical Research: Solid Earth*, *89*(B5), 3253-3274. DOI: https://doi.org/10.1029/JB089iB05p03253

Grove, T. L., Chatterjee, N., Parman, S. W., & Médard, E. (2006). The influence of H2O on mantle wedge melting. *Earth and Planetary Science Letters*, *249*(1-2), 74-89. DOI: https://doi.org/10.1016/j.epsl.2006.06.043

Hammer, J. E., & Rutherford, M. J. (2002). An experimental study of the kinetics of decompression-induced crystallization in silicic melt. *Journal of Geophysical Research: Solid Earth*, *107*(B1), ECV-8. DOI: https://doi.org/10.1029/2001JB000281

Hansen, J., Lacis, A., Ruedy, R., & Sato, M. (1992). Potential climate impact of Mount Pinatubo eruption. *Geophysical Research Letters*, *19*(2), 215-218. DOI: https://doi.org/10.1029/91GL02788

Hastie, T., Tibshirani, R., & Friedman, J. (2009). *The Elements of Statistical Learning: Data Mining, Inference, and Prediction, Second Edition*. Springer.

Higgins, O., Sheldrake, T., & Caricchi, L. (2022). Machine learning thermobarometry and chemometry using amphibole and clinopyroxene: a window into the roots of an arc volcano (Mount Liamuiga, Saint Kitts). *Contributions to Mineralogy and Petrology*, *177*(1), 10. DOI: https://doi.org/10.1007/s00410-021-01874-6

Housh, T. B., & Luhr, J. F. (1991). Plagioclase-melt equilibria in hydrous systems. *American Mineralogist*, *76*(3-4), 477-492.

Hudson, T. S., White, R. S., Greenfield, T., Ágústsdóttir, T., Brisbourne, A., & Green, R. G. (2017). Deep crustal melt plumbing of Bárðarbunga volcano, Iceland. *Geophysical Research Letters*, *44*(17), 8785-8794.

Humphreys, M. C., Smith, V. C., Coumans, J. P., Riker, J. M., Stock, M. J., de Hoog, J. C. M., & Brooker, R. A. (2021). Rapid pre-eruptive mush reorganisation and atmospheric volatile emissions from the 12.9 ka Laacher See eruption, determined using apatite. *Earth and Planetary Science Letters*, *576*, 117198. DOI: https://doi.org/10.1016/j.epsl.2021.117198

Humphreys, M. C., Namur, O., Bohrson, W. A., Bouilhol, P., Cooper, G. F., Cooper, K. M., ... & Spera, F. J. (2025). Crystal mush processes and crustal magmatism. *Nature Reviews Earth & Environment*, 1-16. DOI: https://doi.org/10.1038/s43017-025-00682-x

Jackson, M. D., Blundy, J., & Sparks, R. S. J. (2018). Chemical differentiation, cold storage and remobilization of magma in the Earth's crust. *Nature*, *564*(7736), 405-409. DOI: https://doi.org/10.1038/s41586-018-0746-2

Johnson, E. A., & Rossman, G. R. (2013). The diffusion behavior of hydrogen in plagioclase feldspar at 800–1000 C: Implications for re-equilibration of hydroxyl in volcanic phenocrysts. *American Mineralogist*, *98*(10), 1779-1787. DOI: https://doi.org/10.2138/am.2013.4521

Jorgenson, C., Higgins, O., Petrelli, M., Bégué, F., & Caricchi, L. (2022). A machine learning-based approach to clinopyroxene thermobarometry: Model optimization and

distribution for use in Earth sciences. *Journal of Geophysical Research: Solid Earth*, *127*(4), e2021JB022904. DOI: https://doi.org/10.1029/2021JB022904

Kelley, K. A., Plank, T., Newman, S., Stolper, E. M., Grove, T. L., Parman, S., & Hauri, E. H. (2010). Mantle melting as a function of water content beneath the Mariana Arc. *Journal of Petrology*, *51*(8), 1711-1738. DOI: https://doi.org/10.1093/petrology/egq036

Kent, A. J. (2008). Melt inclusions in basaltic and related volcanic rocks. *Reviews in Mineralogy and Geochemistry*, *69*(1), 273-331. DOI: https://doi.org/10.2138/rmg.2008.69.8

Kittler, J., & Roli, F. (2000). Multiple classifier systems. *Lecture notes in Computer Science*, *1857.*

Köhn, H. F., & Hubert, L. J. (2014). Hierarchical cluster analysis. *Wiley StatsRef: statistics reference online*, 1-13.

Kudo, A. M., & Weill, D. F. (1970). An igneous plagioclase thermometer. *Contributions to Mineralogy and Petrology*, *25*(1), 52-65. DOI: https://doi.org/10.1007/BF00383062

Kumamoto, K. M., Warren, J. M., & Hauri, E. H. (2017). New SIMS reference materials for measuring water in upper mantle minerals. *American Mineralogist*, *102*(3), 537-547. DOI: https://doi.org/10.2138/am-2017-5863CCBYNCND

Lang, M., Zhang, Z., Chen, Z., Cheng, Z., Santosh, M., & Kusky, T. M. (2023). Classification and nomenclature of volcanic rocks using immobile elements: a novel approach based on big data analysis. *Lithos*, *454*, 107274. DOI: https://doi.org/10.1016/j.lithos.2023.107274

Lange, R. A., Frey, H. M., & Hector, J. (2009). A thermodynamic model for the plagioclase-liquid hygrometer/thermometer. *American Mineralogist*, *94*(4), 494-506.

Le Losq, C., Valentine, A. P., Mysen, B. O., & Neuville, D. R. (2021). Structure and properties of alkali aluminosilicate glasses and melts: Insights from deep learning. *Geochimica et Cosmochimica Acta*, *314*, 27-54. DOI: https://doi.org/10.1016/j.gca.2021.08.023

Le Losq, C., & Baldoni, B. (2023). Machine learning modeling of the atomic structure and physical properties of alkali and alkaline-earth aluminosilicate glasses and melts. *Journal of Non-Crystalline Solids*, *617*, 122481. DOI: https://doi.org/10.1016/j.jnoncrysol.2023.122481

Li, W., Costa, F., & Nagashima, K. (2021). Apatite crystals reveal melt volatile budgets and magma storage depths at Merapi volcano, Indonesia. *Journal of Petrology*, *62*(4), egaa100. DOI: https://doi.org/10.1093/petrology/egaa100

Li, X., & Zhang, C. (2022). Machine learning thermobarometry for biotite-bearing magmas. *Journal of Geophysical Research: Solid Earth*, *127*(9), e2022JB024137. DOI: https://doi.org/10.1029/2022JB024137

Liu, E. J., Oliva, M., Antoniades, D., Giralt, S., Granados, I., Pla-Rabes, S., ... & Geyer, A. (2016). Expanding the tephrostratigraphical framework for the South Shetland Islands, Antarctica, by combining compositional and textural tephra characterisation. *Sedimentary Geology*, *340*, 49-61. DOI: https://doi.org/10.1016/j.sedgeo.2015.08.002

Longhi, J., Fram, M. S., Vander Auwera, J., & Montieth, J. N. (1993). Pressure effects, kinetics, and rheology of anorthositic and related magmas. *American Mineralogist*, *78*(9-10), 1016-1030.

Lormand, C., Zellmer, G. F., Németh, K., Kilgour, G., Mead, S., Palmer, A. S., ... & Moebis, A. (2018). Weka trainable segmentation plugin in ImageJ: a semi-automatic tool applied to crystal size distributions of microlites in volcanic rocks. *Microscopy and Microanalysis*, *24*(6), 667-675. DOI:https://doi.org/10.1017/S1431927618015428

Lubbers, J., Loewen, M., Wallace, K., Coombs, M., & Addison, J. (2023). Probabilistic source classification of large tephra producing eruptions using supervised machine learning: An example from the Alaska-Aleutian arc. *Geochemistry, Geophysics, Geosystems*, *24*(11), e2023GC011037. DOI: https://doi.org/10.1029/2023GC011037

Maclennan, J. (2017). Bubble formation and decrepitation control the CO 2 content of olivine-hosted melt inclusions. *Geochemistry, Geophysics, Geosystems*, *18*(2), 597-616. DOI: https://doi.org/10.1002/2016GC006633

Magee, C., Stevenson, C. T., Ebmeier, S. K., Keir, D., Hammond, J. O., Gottsmann, J. H., ... & Jackson, M. D. (2018). Magma plumbing systems: a geophysical perspective. *Journal of Petrology*, *59*(6), 1217-1251. DOI: https://doi.org/10.1093/petrology/egy064

Maisonneuve, C. B., Forni, F., & Bachmann, O. (2021). Magma reservoir evolution during the build up to and recovery from caldera-forming eruptions–a generalizable model?. *Earth-Science Reviews*, *218*, 103684. DOI: https://doi.org/10.1016/j.earscirev.2021.103684

Manley, G. F., Mather, T. A., Pyle, D. M., Clifton, D. A., Rodgers, M., Thompson, G., & Roman, D. C. (2021). Machine learning approaches to identifying changes in eruptive state using multi-parameter datasets from the 2006 eruption of Augustine volcano, Alaska. *Journal of Geophysical Research: Solid Earth*, *126*(12), e2021JB022323. DOI: https://doi.org/10.1029/2021JB022323

Marxer, F., Ulmer, P., & Müntener, O. (2023). Ascent-driven differentiation: a mechanism to keep arc magmas metaluminous?.*Contributions to Mineralogy and Petrology*, *178*(8), 51. DOI: https://doi.org/10.1007/s00410-023-02035-7

Matthews, G. J., Brophy, J. K., Luetkemeier, M., Gu, H., & Thiruvathukal, G. K. (2018). A comparison of machine learning techniques for taxonomic classification of

teeth from the Family Bovidae. *Journal of Applied Statistics*, *45*(15), 2773-2787. DOI: https://doi.org/10.1080/02664763.2018.1441381

McKenzie, D. A. N. (1984). The generation and compaction of partially molten rock. *Journal of Petrology*, *25*(3), 713-765. DOI: https://doi.org/10.1093/petrology/25.3.713

Melekhova, E., Blundy, J., Robertson, R., & Humphreys, M. C. (2015). Experimental evidence for polybaric differentiation of primitive arc basalt beneath St. Vincent, Lesser Antilles. *Journal of Petrology*, *56*(1), 161-192. DOI: https://doi.org/10.1093/petrology/egu074

Mercado, R. A., Lacsamana, J. B. T., & Pineda, G. L. (1999). Socioeconomic impacts of the Mount Pinatubo eruption. In C. G. Newhall & R. S. Punongbayan (Eds.), *Fire and mud: Eruptions and lahars of Mount Pinatubo, Philippines* (pp. 1163–1182). University of Washington Press.

Minnis, P., Harrison, E. F., Stowe, L. L., Gibson, G. G., Denn, F. M., Doelling, D. R., & Smith Jr, W. L. (1993). Radiative climate forcing by the Mount Pinatubo eruption. *Science*, *259*(5100), 1411-1415.

Mohan, A., Singh, A. K., Kumar, B., & Dwivedi, R. (2021). Review on remote sensing methods for landslide detection using machine and deep learning. *Transactions on Emerging Telecommunications Technologies*, *32*(7), e3998. DOI: https://doi.org/10.1002/ett.3998

Müntener, O., Kelemen, P. B., & Grove, T. L. (2001). The role of H2O during crystallization of primitive arc magmas under uppermost mantle conditions and genesis of igneous pyroxenites: an experimental study. *Contributions to Mineralogy and Petrology*, *141*(6), 643-658. DOI: https://doi.org/10.1007/s004100100266

Musu, A., Corsaro, R. A., Higgins, O., Jorgenson, C., Petrelli, M., & Caricchi, L. (2023). The magmatic evolution of South-East Crater (Mt. Etna) during the February–April 2021 sequence of lava fountains from a mineral chemistry

perspective. *Bulletin of Volcanology*, *85*(5), 33. DOI: https://doi.org/10.1007/s00445-023-01643-2

Neave, D. A., Bali, E., Guðfinnsson, G. H., Halldórsson, S. A., Kahl, M., Schmidt, A. S., & Holtz, F. (2019). Clinopyroxene–liquid equilibria and geothermobarometry in natural and experimental tholeiites: the 2014–2015 Holuhraun eruption, Iceland. *Journal of Petrology*, *60*(8), 1653-1680. DOI: https://doi.org/10.1093/petrology/egz042

Newhall, C.G., Hendley, J.W.I., Stauffer, P.H. (1998). The cataclysmic 1991 eruption of Mount Pinatubo, Philippines. https://pubs.usgs.gov/fs/1997/fs113-97/fs113-97.pdf.

O'Leary, J. A., Gaetani, G. A., & Hauri, E. H. (2010). The effect of tetrahedral Al3+ on the partitioning of water between clinopyroxene and silicate melt. *Earth and Planetary Science Letters*, *297*(1-2), 111-120. DOI: https://doi.org/10.1016/j.epsl.2010.06.011

Panjasawatwong, Y., Danyushevsky, L. V., Crawford, A. J., & Harris, K. L. (1995). An experimental study of the effects of melt composition on plagioclase-melt equilibria at 5 and 10 kbar: implications for the origin of magmatic high-An plagioclase. *Contributions to Mineralogy and Petrology*, *118*(4), 420-432. DOI: https://doi.org/10.1007/s004100050024

Paulatto, M., Hooft, E. E., Chrapkiewicz, K., Heath, B., Toomey, D. R., & Morgan, J. V. (2022). Advances in seismic imaging of magma and crystal mush. *Frontiers in Earth Science*, *10*, 970131. DOI: https://doi.org/10.3389/feart.2022.970131

Peterson, L. D., Newcombe, M. E., Piccoli, P. M., Gion, A., Nielsen, S. G., Gaetani, G. A., ... & Wang, J. (2026). The partitioning of H between olivine and melt at low pressures (10–200 MPa). *American Mineralogist*, *111*(1), 29-46.

Petrelli, M., Caricchi, L., & Perugini, D. (2020). Machine learning thermo-barometry: Application to clinopyroxene-bearing magmas. *Journal of Geophysical Research: Solid Earth*, *125*(9), e2020JB020130. DOI: https://doi.org/10.1029/2020JB020130

Putirka, K. D. (2008). Thermometers and barometers for volcanic systems. *Reviews in Mineralogy and Geochemistry, 69*(1), 61-120. DOI: https://doi.org/10.2138/rmg.2008.69.3

Pyle, D. M. (2015). Sizes of volcanic eruptions. In *The encyclopedia of volcanoes* (pp. 257-264). Academic Press.

Qiao, S., Chen, L. C., & Yuille, A. (2021). Detectors: Detecting objects with recursive feature pyramid and switchable atrous convolution. In *Proceedings of the IEEE/CVF conference on computer vision and pattern recognition* (pp. 10213-10224).

Radu, I. B., Skogby, H., Troll, V. R., Deegan, F. M., Geiger, H., Müller, D., & Thordarson, T. (2023). Water in clinopyroxene from the 2021 Geldingadalir eruption of the Fagradalsfjall Fires, SW-Iceland. *Bulletin of Volcanology*, *85*(5), 31. DOI: https://doi.org/10.1007/s00445-023-01641-4

Riker, J. M., Cashman, K. V., Rust, A. C., & Blundy, J. D. (2015). Experimental constraints on plagioclase crystallization during H 2 O-and H 2 O–CO 2-saturated magma decompression. *Journal of Petrology*, *56*(10), 1967-1998. DOI: https://doi.org/10.1093/petrology/egv059

Romero, I. C., Kong, S., Fowlkes, C. C., Jaramillo, C., Urban, M. A., Oboh-Ikuenobe, F., ... & Punyasena, S. W. (2020). Improving the taxonomy of fossil pollen using convolutional neural networks and superresolution microscopy. *Proceedings of the National Academy of Sciences*, *117*(45), 28496-28505. DOI: https://doi.org/10.1073/pnas.2007324117

Rosenberg, C. L., & Handy, M. R. (2005). Experimental deformation of partially melted granite revisited: implications for the continental crust. *Journal of metamorphic Geology*, *23*(1), 19-28. DOI: https://doi.org/10.1111/j.1525-1314.2005.00555.x

Rougier, J., Sparks, R. S. J., Cashman, K. V., & Brown, S. K. (2018). The global magnitude–frequency relationship for large explosive volcanic eruptions. *Earth and Planetary Science Letters*, *482*, 621-629. DOI: https://doi.org/10.1016/j.epsl.2017.11.015

Rubin, A. E., Cooper, K. M., Till, C. B., Kent, A. J., Costa, F., Bose, M., ... & Cole, J. (2017). Rapid cooling and cold storage in a silicic magma reservoir recorded in individual crystals. *Science*, *356*(6343), 1154-1156. DOI: https://doi.org/10.1126/science.aam8720

Scandone, R., Cashman, K. V., & Malone, S. D. (2007). Magma supply, magma ascent and the style of volcanic eruptions. *Earth and Planetary Science Letters*, *253*(3-4), 513-529. DOI: https://doi.org/10.1016/j.epsl.2006.11.016

Sigl, M., Winstrup, M., McConnell, J. R., Welten, K. C., Plunkett, G., Ludlow, F., ... & Woodruff, T. E. (2015). Timing and climate forcing of volcanic eruptions for the past 2,500 years. *Nature*, *523*(7562), 543-549. DOI: https://doi.org/10.1038/nature14565

Simm, J., De Abril, I. M., & Sugiyama, M. (2014). Tree-based ensemble multi-task learning method for classification and regression. *IEICE TRANSACTIONS on Information and Systems*, *97*(6), 1677-1681. https://doi.org/10.1587/transinf.E97.D.1677

Sisson, T. W., and Grove, T. L. (1993). Experimental investigations of the role of H 2 O in calc-alkaline differentiation and subduction zone magmatism. *Contributions to Mineralogy and Petrology.* 113, 143–166. DOI: https://doi.org/10.1007/BF00283225

Solano, J. M. S., Jackson, M. D., Sparks, R. S. J., Blundy, J. D., & Annen, C. (2012). Melt segregation in deep crustal hot zones: a mechanism for chemical differentiation, crustal assimilation and the formation of evolved magmas. *Journal of Petrology*, *53*(10), 1999-2026. DOI: https://doi.org/10.1093/petrology/egs041

Sparks, R. S. J., Annen, C., Blundy, J. D., Cashman, K. V., Rust, A. C., & Jackson, M. D. (2019). Formation and dynamics of magma reservoirs. *Philosophical*

Transactions of the Royal Society A, *377*(2139), 20180019. DOI: https://doi.org/10.1098/rsta.2018.0019

Thomson, A. R., Kohn, S. C., Prabhu, A., & Walter, M. J. (2021). Evaluating the formation pressure of diamond-hosted majoritic garnets: A machine learning majorite barometer. *Journal of Geophysical Research: Solid Earth*, *126*(3), e2020JB020604. DOI: https://doi.org/10.1029/2020JB020604

Toth, N., & Maclennan, J. (2024). MinDet1: A deep learning-enabled approach for plagioclase textural studies. *Volcanica*, *7*(1), 135-151. DOI: https://doi.org/10.30909/vol.07.01.135151

Ueki, K., & Iwamori, H. (2017). Geochemical differentiation processes for arc magma of the Sengan volcanic cluster, Northeastern Japan, constrained from principal component analysis. *Lithos*, *290*, 60-75. DOI: https://doi.org/10.1016/j.lithos.2017.08.001

Ulmer, P., Kaegi, R., & Müntener, O. (2018). Experimentally derived intermediate to silica-rich arc magmas by fractional and equilibrium crystallization at 1· 0 GPa: an evaluation of phase relationships, compositions, liquid lines of descent and oxygen fugacity. *Journal of Petrology*, *59*(1), 11-58. DOI: https://doi.org/10.1093/petrology/egy017

Walker, G. P. L. (1981). Plinian eruptions and their products. *Bulletin Volcanologique*, *44*(3), 223-240.

Ward, K. M., Zandt, G., Beck, S. L., Christensen, D. H., & McFarlin, H. (2014). Seismic imaging of the magmatic underpinnings beneath the Altiplano-Puna volcanic complex from the joint inversion of surface wave dispersion and receiver functions. *Earth and Planetary Science Letters*, *404*, 43-53. DOI: https://doi.org/10.1016/j.epsl.2014.07.022

Waters, L. E., & Lange, R. A. (2015). An updated calibration of the plagioclase-liquid hygrometer-thermometer applicable to basalts through rhyolites. *American Mineralogist*, *100*(10), 2172-2184.

Weber, G., & Blundy, J. (2024). A machine learning-based thermobarometer for magmatic liquids. *Journal of Petrology*, *65*(4), egae020. DOI: https://doi.org/10.1093/petrology/egae020

Weinberg, R. F., Vernon, R. H., & Schmeling, H. (2021). Processes in mushes and their role in the differentiation of granitic rocks. *Earth-Science Reviews*, *220*, 103665. DOI: https://doi.org/10.1016/j.earscirev.2021.103665

Wieser, P. E., Gleeson, M., Matthews, S., DeVitre, C. L., & Gazel, E. (2023). Determining the pressure–temperature–composition (PTX) conditions of magma storage.

Wills, S., Underwood, C. J., & Barrett, P. M. (2021). Learning to see the wood for the trees: machine learning, decision trees, and the classification of isolated theropod teeth. *Palaeontology*, *64*(1), 75-99. DOI: https://doi.org/10.1111/pala.12512

Willard, J., Jia, X., Xu, S., Steinbach, M., & Kumar, V. (2022). Integrating scientific knowledge with machine learning for engineering and environmental systems. *ACM Computing Surveys*, *55*(4), 1-37. DOI: https://doi.org/10.1145/3514228

Wilson, C. J., Cooper, G. F., Chamberlain, K. J., Barker, S. J., Myers, M. L., Illsley-Kemp, F., & Farrell, J. (2021). No single model for supersized eruptions and their magma bodies. *Nature Reviews Earth & Environment*, *2*(9), 610-627. DOI: https://doi.org/10.1038/s43017-021-00191-7

Yip, S. T. H., Biggs, J., Edmonds, M., Liggins, P., & Shorttle, O. (2022). Contrasting volcanic deformation in arc and ocean island settings due to exsolution of magmatic water. *Geochemistry, Geophysics, Geosystems*, *23*(7), e2022GC010387. DOI: https://doi.org/10.1029/2022GC010387

Zimmer, M. M., Plank, T., Hauri, E. H., Yogodzinski, G. M., Stelling, P., Larsen, J., ... & Nye, C. J. (2010). The role of water in generating the calc-alkaline trend: new volatile data for Aleutian magmas and a new tholeiitic index. *Journal of Petrology, 51*(12), 2411-2444. DOI: https://doi.org/10.1093/petrology/egq062

Zhou, Z. H. (2021). *Machine learning*. Springer nature.

2 | Plagioclase-saturated melt hygrothermobarometry and plagioclase-melt equilibria using machine learning

K. S. Cutler[1*], M. Cassidy[1,2], and J.D. Blundy[1]

1 Department of Earth Sciences, University of Oxford, South Parks Road, Oxford, OX1 3AN, UK

2 School of Geography, Earth and Environmental Sciences, University of Birmingham, Edgbaston, Birmingham, B15 2TT, UK

As published in Geochemistry, Geophysics, Geosystems (DOI: https://doi.org/10.1029/2023GC011357)

Abstract

Compositions of plagioclase-melt pairs are commonly used to constrain temperatures (T), dissolved water contents (H_2O) and pressures (P) of pre-eruptive magma storage and transport. However, previous plagioclase-based thermometers, hygrometers, and barometers can have significant errors, leading to imprecise reconstructions of conditions during plagioclase growth. Here, we explore whether we can refine existing plagioclase-based hygrothermobarometers with either plagioclase-melt or melt-only chemistry (± T/H_2O), calibrated using random forest machine learning on experimental petrology data (n= 1152). We find that both the plagioclase-melt and melt-only models return similar cross-validation root-mean-square errors (RMSEs), as the melt holds most of the P-T-H_2O information rather than the plagioclase. T/H_2O-dependent melt models have test set RMSEs of 25 °C, 0.70 wt.% and 76 MPa for temperature, H_2O content and pressure, respectively, while T/H_2O-independent models have RMSEs of 38 °C, 0.97 wt.% and 91 MPa. The melt thermometer and hygrometer are applicable to a wide range of plagioclase-bearing melts at temperatures between 664 and 1355 °C, and with H_2O concentrations up to 11.2 wt.%, while the melt barometer is suitable for pressures of ≤500 MPa. An updated plagioclase-melt equilibrium model has also been calibrated, allowing equilibrium anorthite content to be predicted with an error of 5.8 mol%. The new P-T-H_2O-An models were applied to matrix glasses and melt inclusions from the 1980 Mount St Helens (USA) and 2014-2015 Holuhraun (Iceland) eruptions, corroborating previous independent estimates and observations. Models are available at: https://github.com/kyra-cutler/Plag-saturated-melt-P-T-H2O-An, enabling

assessment of plagioclase-melt equilibrium and characterisation of last-equilibrated P-T-H_2O conditions of plagioclase-saturated magmas.

2.1 Introduction

Temperature (T), pressure (P) and melt water contents (H_2O) collectively control various physiochemical properties of magmas by influencing the crystallisation and stability of mineral phases (e.g., Feig et al., 2010; Krawczynski et al., 2012), as well as the density and viscosity of melts (e.g., Giordano et al., 2008). Placing constraints on the thermal state, volatile concentration, and depths of magma crystallisation thereby enables a critical insight into pre-eruptive storage conditions and magma transport properties, informing our understanding of controls on eruption dynamics and the crustal architecture of sub-volcanic systems (e.g., Cassidy et al., 2018; Bamber et al., 2022; Caricchi et al., 2021; Giordano and Caricchi, 2022). Furthermore, integrating petrological constraints with potential signs of volcanic unrest (i.e., seismicity, surface deformation, gas emissions; e.g., Saunders et al., 2012; Stock et al., 2018; Cassidy et al., 2019; Liu et al., 2020; Yip et al., 2022) can facilitate monitoring and hazard management at restless volcanoes (e.g., Pritchard et al., 2019).

Plagioclase is an abundant mineral found in volcanic rocks across a wide compositional range, with its chemistry sensitive to temperature, melt composition – including water content – and pressure (e.g., Housh and Luhr, 1991; Longhi et al., 1993; Panjasawatong et al., 1995; Lange et al., 2009; Namur et al., 2012). This has led to the development of a range of plagioclase-melt thermometers, hygrometers and barometers (e.g., Putirka, 2005; Putirka, 2008; Lange et al., 2009; Waters and Lange, 2015;

Masotta and Mollo, 2019), with expressions based on the equilibrium exchange of albite (Ab; $NaAlSi_3O_8$) and anorthite (An; $CaAl_2Si_2O_8$) components between plagioclase and melt (Equation 1):

$$CaAl_2Si_2O_8^{crystal} + NaAlSi_3O_8^{melt} = CaAl_2Si_2O_8^{melt} + NaAlSi_3O_8^{crystal} \quad (1)$$

Temperature and melt water contents recovered with plagioclase-melt thermometers and hygrometers have relatively small errors (e.g., Equation 24a, ± 36 °C; Putirka, 2008; ± 0.29 wt.% (trachyte-specific) Masotta and Mollo, 2019; 0.35 wt.%, Waters and Lange, 2015; 1.1 wt.%, Putirka, 2008 (Equation 25b)), although such models are dependent on at least one independently-constrained intensive variable (i.e., T, H_2O or P), yielding higher errors when errors are propagated or iterative calculations are performed (Wieser et al., 2023a). The only plagioclase-melt barometer available is a formulation by Putirka (2005, 2008), which returns a significantly large Standard Error Estimate (SEE: 380 MPa; which is equivalent to ± 10.5 km depth uncertainty using a 2700 kg/m^3 crustal density), resulting from the negligible volume change of reaction (Equation 1) at low pressures (c.f. ≤300 MPa; Lange et al., 2009). Similarly, other mineral-based barometer calibrations are associated with comparably poor accuracy and precision (e.g., clinopyroxene: 200–500 MPa, ± 5.5–14 km depth, Wieser et al., 2023b; amphibole: 300–400 MPa, ± 8–11 km, Putirka, 2016), sufficient only for outlining broad depth ranges of magma crystallisation. Establishing a precise and accurate barometer is thus a key petrological target for obtaining high-resolution images of magmatic systems, as identified by the SZ4 initiative (Hilley et al., 2022). The poor performance prevalent in the current scope of barometers may derive from various factors, including low precision electron microprobe measurements on pressure-

sensitive analytes (i.e., Na_2O in clinopyroxene; Wieser et al., 2023a), disequilibrium textures in experimental products (e.g., clinopyroxene sector zoning; Neave et al., 2019), or a weak pressure dependency on compositional variables (e.g., Putirka, 2016). Another factor that can contribute to the large uncertainty of pressure estimates is the strategy used to calibrate barometric models (Higgins et al., 2022). Recently, supervised machine learning (ML) algorithms have proven to be a successful approach to obtain T and P predictions (e.g., Petrelli et al., 2020; Higgins et al., 2022; Thomson et al., 2021; Jorgenson et al., 2022), as the algorithms are not reliant on any a priori thermodynamic knowledge and can capture non-linearity between variables.

Over the past 50 years, several empirical or thermodynamic-based models have been developed to predict the equilibrium compositions of plagioclase (An = [molar Ca/(Ca + Na + K)]) crystallising from silicate melts. Although the majority of plagioclase-melt equilibria models primarily examine the effect of H_2O and pressure on plagioclase composition (e.g., Panjasawatong et al., 1995; Housh and Luhr, 1991), limited studies have focussed on anhydrous systems or combined (hydrous and anhydrous) datasets (e.g., Fuhrman and Lindsley, 1988; Namur et al., 2012; Putirka, 2005). This necessitates creating an updated plagioclase-melt equilibria model, applicable to modelling an extensive range of differentiated liquids irrespective of melt water content.

In this study, our aims are two-fold. With the large number of plagioclase-bearing experiments available, we first use machine learning (ML) to test whether we can refine the existing range (i.e., Putirka, 2005; Putirka, 2008; Waters and Lange, 2015; Masotta and Mollo, 2019) of plagioclase-based hygrothermobarometers, either by using plagioclase-melt or melt-only chemistry. Secondly, we aim to create an ML model for

predicting equilibrium plagioclase compositions solely as a function of melt chemistry. We then test the capability of the models to recover magma crystallisation conditions at two well-studied volcanic systems, comparing P-T-H_2O-An estimates with melt inclusion analyses, geophysical data, and independent hygrothermobarometric and plagioclase-melt equilibria calculations.

2.2 Developing hygrothermobarometric and anorthite content models

2.2.1 Dataset compilation and filtering

Experimental plagioclase-melt pairs were extracted from the Library of Experimental Phase Relations (LEPR) database (Hirschmann et al., 2008) and supplemented by an extensive literature search to calibrate all plagioclase-melt and melt-only versions of models. The final dataset (n=1152) includes anhydrous/nominally anhydrous, fluid-saturated and fluid-undersaturated experiments; the full calibration dataset can be accessed in Supplementary Table S2.1. We applied a set of filters to the experimental data to ensure coexisting plagioclase-melt pairs were in equilibrium (e.g., Lange et al., 2009; Namur et al., 2012; Waters and Lange, 2015): (1) only experiments with a quenched liquid (i.e. glass) fraction of ≥50% were selected, as high crystallinity charges are subject to slower diffusion rates in minerals compared to the melt, requiring longer timescales to reach equilibrium. Experiments were excluded if phase or crystallinity proportions were not reported. (2) Only experiments with electron microprobe analytical totals between 97 and 101.5 wt.% (including H_2O) were incorporated. This filter ensures that any potential analytical errors are minimised. (3) Experiments were removed if papers reported evidence for significant sodium and/or iron loss (≥10 wt.% relative

Na_2O or FeOt). It must be noted that some plagioclase-saturated melt compositions in the literature lack compositions of coexisting plagioclases. For the hygrometry models, only experiments with well-constrained water analyses (i.e., Fourier-Transform InfraRed spectroscopy, Secondary Ion Mass Spectroscopy, Raman spectroscopy) were used as the water content values for calibration. However, only ~35% of hydrous experiments have measured water content estimates. Therefore, MagmaSat (Ghiorso and Gualda, 2015) in VESIcal (Iacovino et al. 2021) was used to calculate the water content in the remaining water-saturated and undersaturated (if fluid $X H_2O$ value was reported) experiments.

2.2.2 Calibration range

The calibration dataset covers a range of terrestrial and non-terrestrial analogue melts (SiO_2: 37.1–79.9 wt.%; $Na_2O + K_2O$: 0.3–14.6 wt.%) that crystallised plagioclase (An_{16-100}) at conditions from 0–2000 MPa, 664–1355 °C, and H_2O concentrations up to 11.2 wt.% (Figure 2.1). Temperature displays a bimodal distribution with peaks at 850–900 °C (felsic melts) and 1100–1200 °C (mafic melts), whereas plagioclase compositions are symmetrically distributed. Pressure and H_2O have strong positively-skewed distributions. Excluding the experiments undertaken at 1 atm, 85% of the experiments occur at pressures of ≤500 MPa. There is minimal variation in T and H_2O at pressures >500 MPa within the overall P range, except for the 700 MPa experiments (Figure 2.1b). From all the hydrous experimental data, there is an evident lack of experiments with higher H_2O (>7 wt.%) contents, although 9 ± 1 wt.% represents the maximum limit to which H_2O in experimental mafic melts can be quenched to glass (Gavrilenko et al., 2019). Experiments with lower H_2O (<2 wt.%) are also

underrepresented, reflecting limited studies that measure water content in near-anhydrous experimental glasses (i.e., Whittaker et al., 2007; Husen et al., 2016) and/or undertaking water-saturated runs at low pressures.

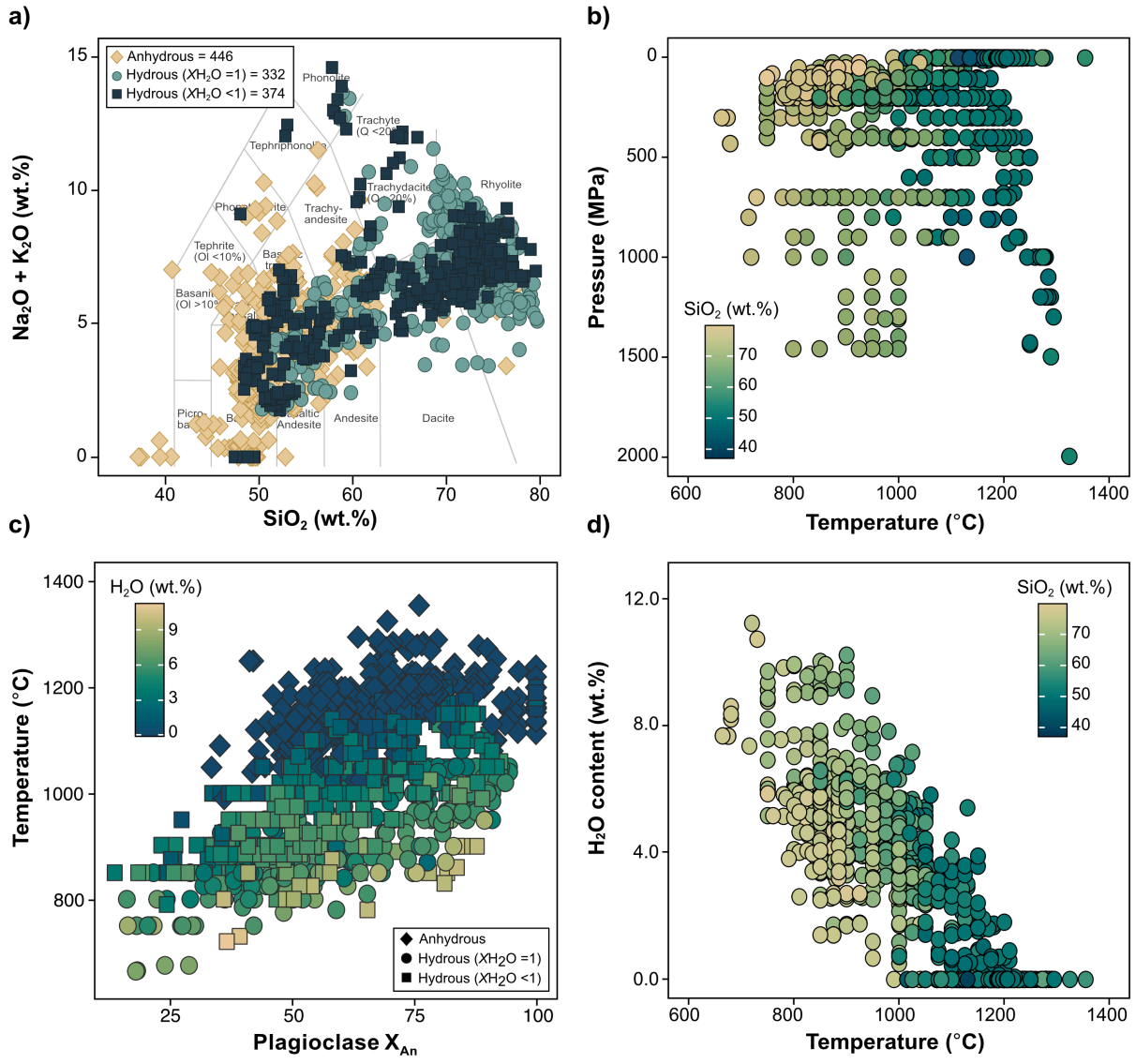

Figure 2.1 Calibration range of compiled plagioclase-saturated experiments. **a**) Total alkali silica classification diagram after Le Maitre et al. (1989) of experimental glass compositions (*n*=1152; Supplementary Table 2.1). The anhydrous experimental total includes nominally anhydrous experiments (*n*=17). **b**) Temperature (°C) versus pressure (MPa) of experiments. Colour coding indicates SiO_2 (wt.%) of the melt. **c**) Plagioclase composition in terms of temperature for all experimental data with plagioclase-melt compositions (*n*=1063) with colour coding highlighting melt H_2O (wt.%) content. **d**) H_2O (wt.%) versus temperature (°C) of experiments. Colour coding reflects SiO_2 (wt.%) of the melt.

2.2.3 Model training and cross-validation

A type of random forest machine learning algorithm, Extremely Randomised Trees, was used to train all the models using the package 'ranger' and the *splitrule* 'extratrees' (Wright and Ziegler, 2017) in R (R Core Team, 2013), as it has been shown to have the highest predictive capability among a selection of supervised learning algorithms (e.g. Petrelli et al., 2020, Li and Zhang, 2022). In short, random forest algorithms are an ensemble machine learning approach involving multiple decision trees, where the output of all individual trees is aggregated to form an averaged prediction. Each target variable (P-T-H_2O-An) is predicted using normalised major element oxide compositions as dependent variables (melt: SiO_2, TiO_2, Al_2O_3, FeO_t, MgO, CaO, Na_2O, K_2O; plagioclase: SiO_2, Al_2O_3, FeO_t, CaO, Na_2O, K_2O) for the plagioclase-melt or melt-only models. MnO in the melt and MnO, TiO_2 and MgO in plagioclase were not considered as input variables since numerous experiments do not report one or more of these oxides and since they are uniformly at very low concentrations in plagioclase. The whole dataset was split into training and testing sets using an 80/20 ratio, with the test set held back and never used during model calibration. The training/testing sets were split using a stratified sampling function to ensure a balanced distribution of the models' target variable (i.e. H_2O, temperature, pressure and An content) in both the training and testing sets. Models can be optimised by tuning hyperparameters, but studies have shown that it has little impact on model performance (e.g., Petrelli et al., 2020; Jorgenson et al., 2022). Therefore, we used the default hyperparameter tuning (i.e., *mtry*) within the Caret package (Kuhn, 2008) to optimise each model while keeping the number of the decision trees small (*num.trees* = 200) to minimise computational time.

We use the median to average the final prediction from the 200 individual decision trees (Figure S1a), which has been shown to return slightly lower RMSEs (Root Mean Square Errors) than the mean (Jorgenson et al., 2022; Weber and Blundy, 2024).

Model errors were assessed using two approaches. First, stratified 10-fold cross-validation was used on the training set using the Caret package, where the training set was split into ten subsets or folds (Figure S2.1b). One of the folds is left out for testing, while the remainder is used to train the model. This process is repeated until all ten rows of folds are processed, generating a median R^2 (coefficient of determination) and RMSE value. All folds were again stratified to remove an imbalanced distribution of the models' target variable. The models were also examined using the testing sets, providing independent metric values. The model RMSE and R^2 values during cross-validation (CV) may differ slightly depending on how the training and testing sets are split. We thus repeated the workflow of random training/testing set splitting and 10-fold cross-validation ten times (Figure S2.1b). After model cross-validation and evaluation, the final saved models were trained on the full calibration dataset (i.e., Petrelli et al., 2020; Thomson et al., 2021).

2.3 P-T-H_2O-An models

2.3.1 Model calibration and validation

Figure 2.2 highlights the overall variation and median RMSE values from the cross-validation of both plagioclase-melt and melt hygrothermobarometry models. The plagioclase-melt and melt models for each variable (P-T-H_2O) depict a remarkably similar performance. The similarity across all models results from the predictive

capability of the algorithm predominantly using the melt rather than the plagioclase compositional components (Figure 2.3), effectively rendering the plagioclase information redundant. This is unlike other random forest-calibrated models using mineral-melt pairs (clinopyroxene, Petrelli et al., 2020; biotite, Li and Zhang, 2022), where both the crystal and melt chemistry information improve the RMSE and R^2 scores. The melt model RMSEs also reaffirm the utility of silicate melt composition in recovering key magmatic variables (e.g. Helz and Thornber, 1987; Yang et al., 1996; Blundy, 2022; Weber and Blundy, 2024). This finding results from the low thermodynamic variance of natural magmatic compositions whose overall chemical variability can be described with a relatively limited number of independent compositional variables, significantly fewer than the total number of constituent oxides, as determined using Principal Component Analysis (Weber and Blundy, 2024). In this section, we will thus focus on the melt models, which are appropriate for use with compositions of quenched and entrapped liquid (i.e. matrix glass or plagioclase-hosted melt inclusions). We will also examine limitations affecting model accuracy (i.e., model calibration) and precision (i.e., analytical uncertainties) to obtain P-T-H_2O estimates and compositions of plagioclase.

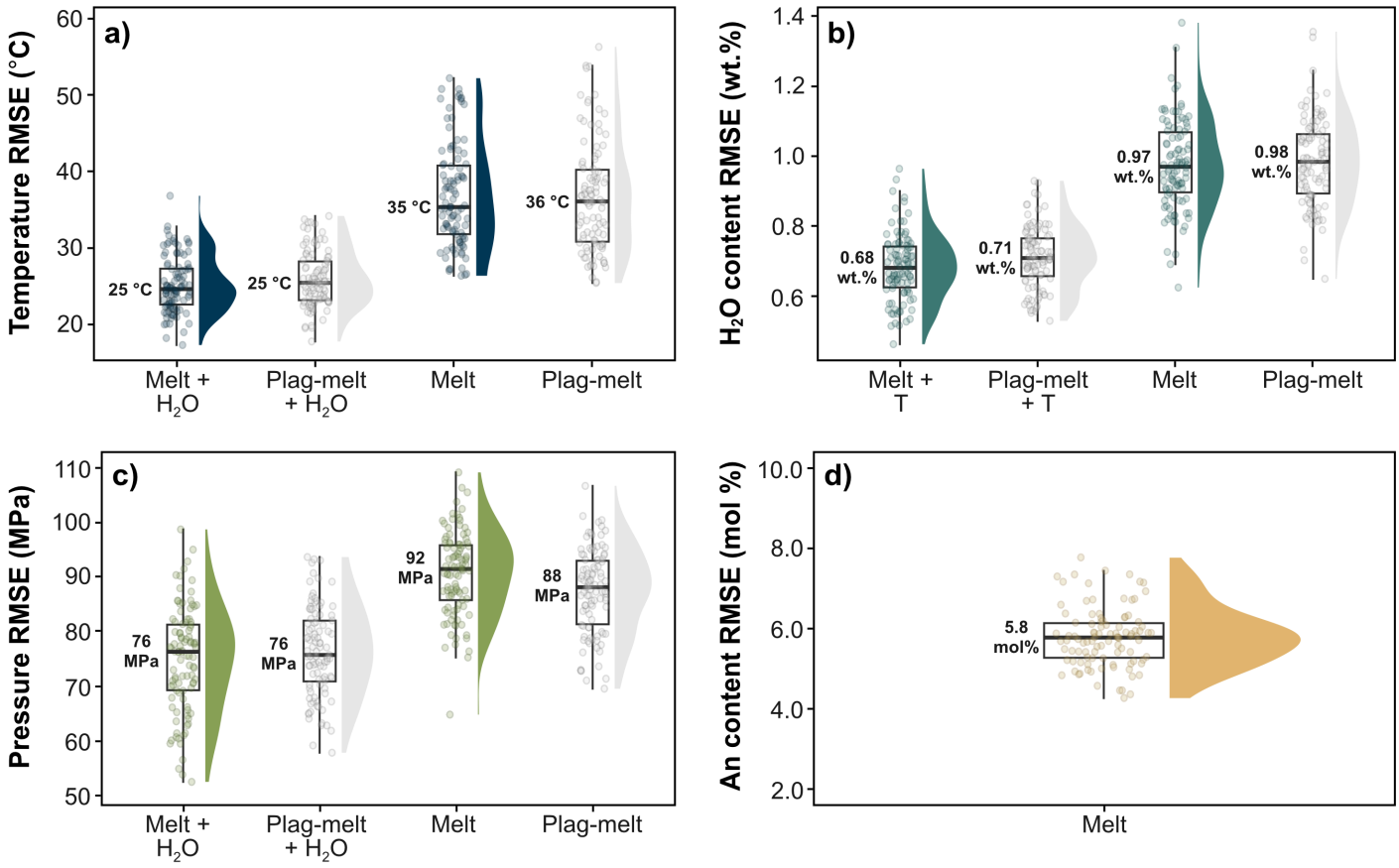

Figure 2.2 Raincloud comparison plots of cross-validation RMSEs from the plagioclase-melt and melt thermometer (**a**), hygrometer (**b**) and barometer (**c**) models, as well as the plagioclase anorthite content model (**d**).

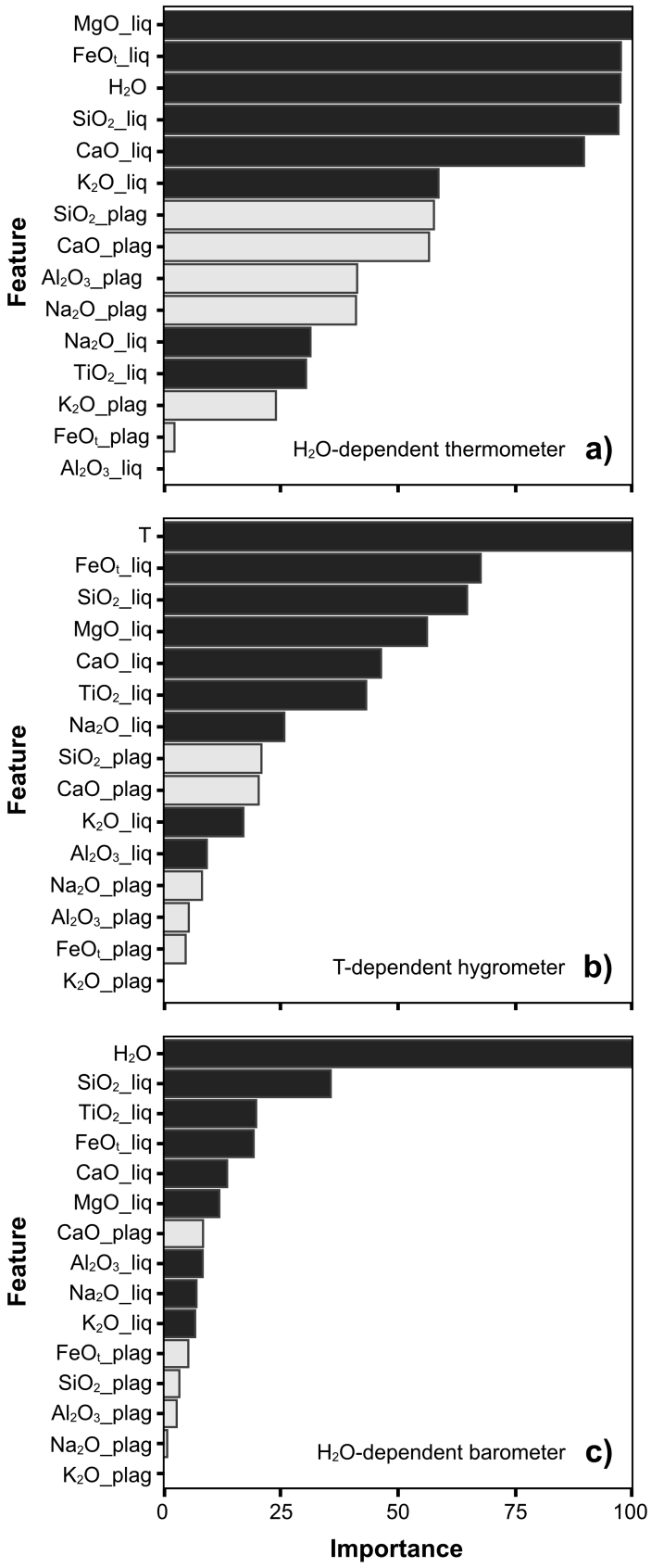
MgO_liq
FeOt_liq
H2O
SiO2_liq
CaO_liq
K2O_liq
SiO2_plag
CaO_plag
Al2O3_plag
Na2O_plag
Na2O_liq
TiO2_liq
K2O_plag
FeOt_plag
Al2O3_liq
Feature
H2O-dependent thermometer
a)
T
FeOt_liq
SiO2_liq
MgO_liq
CaO_liq
TiO2_liq
Na2O_liq
SiO2_plag
CaO_plag
K2O_liq
Al2O3_liq
Na2O_plag
Al2O3_plag
FeOt_plag
K2O_plag
Feature
T-dependent hygrometer
b)
H2O
SiO2_liq
TiO2_liq
FeOt_liq
CaO_liq
MgO_liq
CaO_plag
Al2O3_liq
Na2O_liq
K2O_liq
FeOt_plag
SiO2_plag
Al2O3_plag
Na2O_plag
K2O_plag
Feature
H2O-dependent barometer
c)
0
25
50
75
100
Importance

Figure 2.3 Plots of variable importance versus input variable for the H_2O-dependent thermometer (**a**), T-dependent hygrometer (**b**), and H_2O-dependent barometer (**c**). All plots highlight the most important variables used by the algorithm to make predictions. Light grey bars represent plagioclase compositional inputs, and dark grey bars represent melt oxide inputs along with additional parameters such as T or H_2O.

2.3.2 Thermometry

Temperature and H_2O in the experimental dataset display a strong inverse correlation (Figure 2.1d), leading us to test both an H_2O-independent and H_2O-dependent thermometer. In both instances, the H_2O-independent and H_2O-dependent thermometers yield low mean cross-validation (H_2O-independent, 35 °C; H_2O-dependent, 25 °C; Figure 2.2) and test set RMSE values (H_2O-independent, 38 °C; H_2O-dependent 26 °C). Systematic model errors were assessed by calculating the Mean Bias Error (MBE), as well as checking the regression gradients and intercepts (Wieser et al., 2023a). Both thermometers have relatively low intercept and MBE values with high gradients close to 1 (Figure 2.4b and Figure 2.5b), indicating no systematic offsets across the wide temperature range. Figures 2.4b and 2.5b display the test set residual distribution from all workflow replications and illustrate that 74% and 83% of residuals are within ± 30 °C of the actual experimental temperature for the H_2O-independent and H_2O-dependent thermometer, respectively. The accuracy of the thermometers primarily results from the strong non-linearity of MgO, SiO_2, FeO_t and CaO in the melt when plotted against temperature (Figure S2.2). This is consistent with other liquid thermometers that prioritise MgO, FeO_t and CaO within their parameterisations (e.g., Helz and Thornber, 1987). To further validate the ML models, we compare all our ML test set predictions (P-T-H_2O-An) with estimates generated by previous hygrothermobarometric and plagioclase-melt equilibria models (Figure 2.6). We use Thermobar (version 1.011; Wieser et al., 2023c) to calculate estimates from previous models but limit ourselves to models calibrated for a wide compositional range to ensure comparison across similar experimental conditions. We only compare our

H_2O-dependent thermometer with the plagioclase-saturated liquid thermometer of Putirka (2008) (Equation 26; calibrated for T in the range 850–1350 °C), as both models require H_2O inputs. The ML H_2O-dependent thermometer performs better than Equation 26 with a lower RMSE (26 °C vs. 36 °C), MBE (-0.94 °C vs. -9.6 °C) and intercept (41 °C vs. 112 °C) value, as well as a gradient and R^2 value closer to 1 (Figure 2.5b, Figure 2.6a).

2.3.3 Hygrometry

We tested a T-dependent (Figure 2.5c, 2.5d) and T-independent hygrometer (Figure 2.4c, 2.4d), as temperature is not always well-constrained in petrological studies. The T-dependent hygrometer (Figure 2.5c) returns median cross-validation and test set RMSE values of 0.68 wt.% and 0.69 wt.%, respectively, while the T-independent hygrometer (Figure 2.4c) gives reasonable cross-validation (0.97 wt.%) and test set (0.95 wt.%) RMSEs scores. No systematic offsets across the range of H_2O contents are apparent in the test data for both hygrometers, as they each have low intercept and MBE values and gradients close to 1 (Figure 2.4d, 2.5d). A closer look at the residuals, when grouped by type of experiment, reveals that the T-dependent hygrometer displays no difference in the modal and median values for anhydrous and hydrous ($X H_2O = 1$ and $X H_2O < 1$) experiments (Figure S2.3), with all groups concentrated at zero. For fluid-saturated experiments, the T-independent hygrometer residuals are centred at -1, indicating the model tends to slightly underestimate H_2O compared to fluid-undersaturated and anhydrous experiments. Temperature is an important variable in predicting melt water content, with 70% of the residuals for the T-dependent hygrometer within ±0.5 wt.% of the actual water content value (Figure 2.5d) compared to 58% of the

residuals for the T-independent hygrometer (Figure 2.4d). Aside from temperature, FeOt, SiO_2 and MgO play a key role in water content predictions, in which the algorithm appears to use these three oxides to characterise H_2O content depending on the level of melt differentiation (Figure S2.4). These results broadly correspond with the findings of Zimmer et al. (2010), who show an inverse correlation exists between the level of Fe enrichment in melts (i.e., tholeiitic index) and their water content. We use the Putirka (2008; calibrated for liquids with <9 wt.% H_2O) and Waters and Lange (2015; calibrated for liquids with 0–8.3 wt.% H_2O) plagioclase-melt hygrometers to make a comparison with the T-dependent hygrometer, as all models require temperature inputs. The T-dependent hygrometer outperforms the Putirka (2008) and Waters and Lange (2015) plagioclase-melt hygrometers with a lower overall RMSE (0.69 wt.%), MBE (-0.02 wt.%) and high gradient (0.94) and R^2 value (0.93; Figure 2.5d, Figure 2.6b).

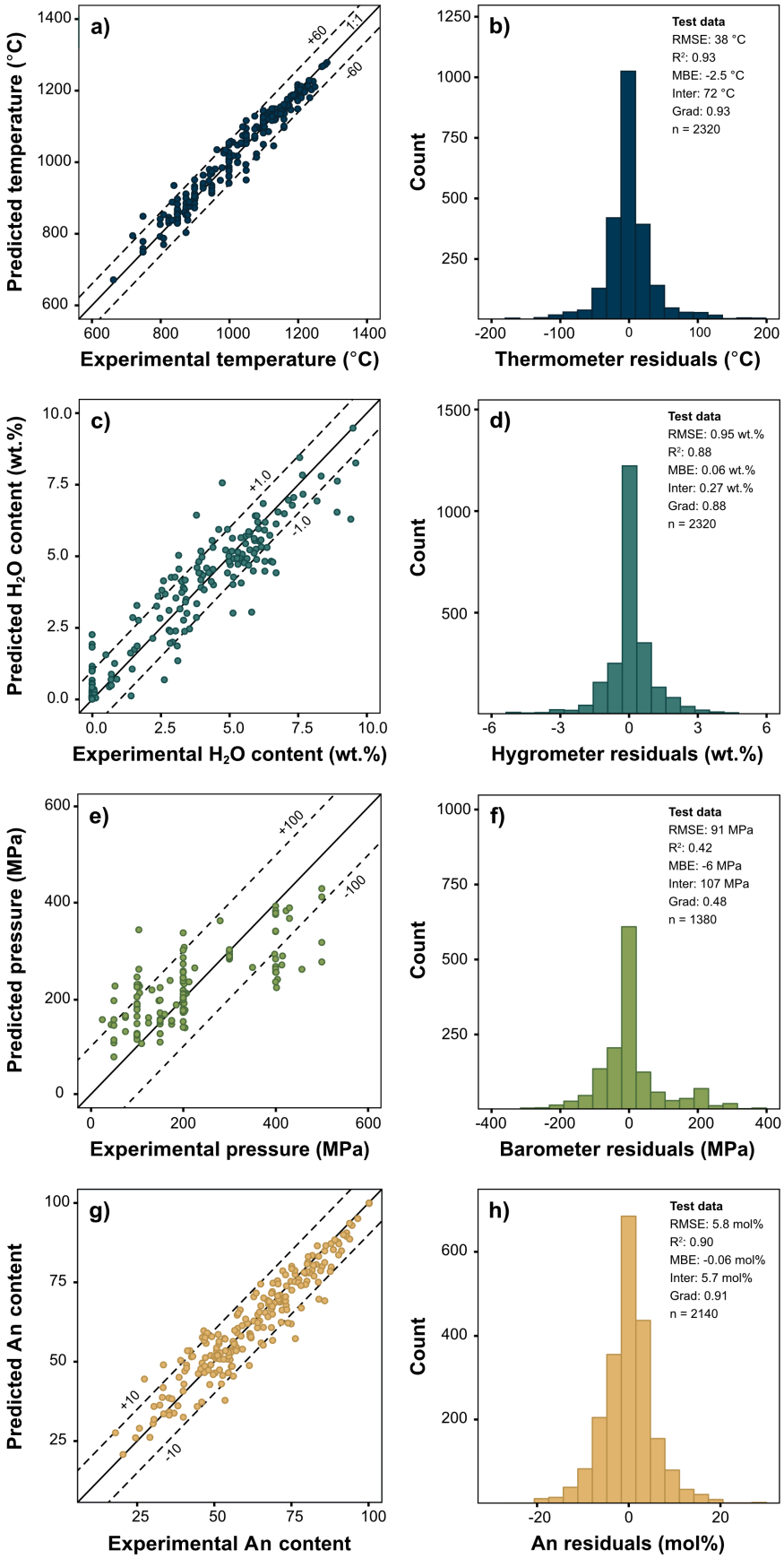
a)
Predicted temperature (°C)
Experimental temperature (°C)
+60
1:1
-60
b)
Test data
RMSE: 38 °C
R²: 0.93
MBE: -2.5 °C
Inter: 72 °C
Grad: 0.93
n = 2320
Count
Thermometer residuals (°C)
c)
Predicted H2O content (wt.%)
Experimental H2O content (wt.%)
+1.0
-1.0
d)
Test data
RMSE: 0.95 wt.%
R²: 0.88
MBE: 0.06 wt.%
Inter: 0.27 wt.%
Grad: 0.88
n = 2320
Count
Hygrometer residuals (wt.%)
e)
Predicted pressure (MPa)
Experimental pressure (MPa)
+100
-100
f)
Test data
RMSE: 91 MPa
R²: 0.42
MBE: -6 MPa
Inter: 107 MPa
Grad: 0.48
n = 1380
Count
Barometer residuals (MPa)
g)
Predicted An content
Experimental An content
+10
-10
h)
Test data
RMSE: 5.8 mol%
R²: 0.90
MBE: -0.06 mol%
Inter: 5.7 mol%
Grad: 0.91
n = 2140
Count
An residuals (mol%)

Figure 2.4 Examples of testing set performance for the melt-only models and residual (difference between experimental value and predicted value) histograms. Only the best-performing testing set is shown for each model. Testing set statistics in the histograms reflect the average RMSE, R^2, MBE, intercept and gradient values across all ten testing sets. **a**) Comparison of experimental versus predicted temperature (°C) showing a 1:1 correspondence line. **b**) Histogram for temperature residuals for all test sets. **c**) Comparison of experimental versus predicted water content (wt.%). **d**) Histogram of water content residuals for all test sets. **e**) Comparison of experimental versus predicted pressure (MPa). **f**) Histogram of pressure residuals for all test sets. **g**) Comparison of experimental versus predicted anorthite content (mol%). **h**) Histogram of anorthite content residuals for all test sets.

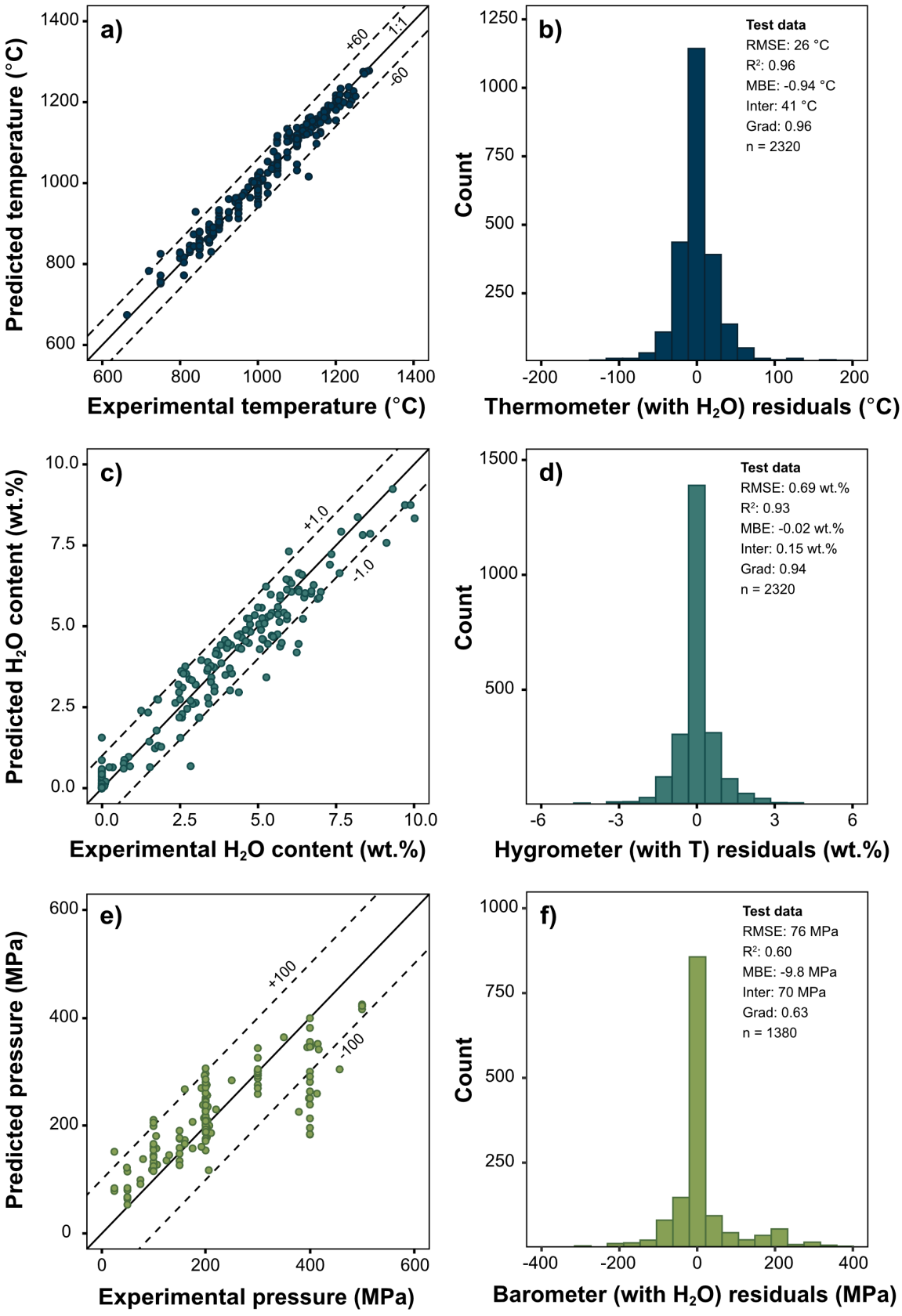
a)
Predicted temperature (°C)
Experimental temperature (°C)
+60
1:1
-60
b)
Test data
RMSE: 26 °C
R²: 0.96
MBE: -0.94 °C
Inter: 41 °C
Grad: 0.96
n = 2320
Count
Thermometer (with H2O) residuals (°C)
c)
Predicted H2O content (wt.%)
Experimental H2O content (wt.%)
+1.0
-1.0
d)
Test data
RMSE: 0.69 wt.%
R²: 0.93
MBE: -0.02 wt.%
Inter: 0.15 wt.%
Grad: 0.94
n = 2320
Count
Hygrometer (with T) residuals (wt.%)
e)
Predicted pressure (MPa)
Experimental pressure (MPa)
+100
-100
f)
Test data
RMSE: 76 MPa
R²: 0.60
MBE: -9.8 MPa
Inter: 70 MPa
Grad: 0.63
n = 1380
Count
Barometer (with H2O) residuals (MPa)

Figure 2.5 Examples of testing set performance for the melt models with additional input parameters (T or H_2O) and residual histograms. Only the best-performing testing set is shown for each model. Testing set statistics in the histograms reflect the average RMSE, R^2, MBE, intercept and gradient values across all ten testing sets. **a**) Comparison of experimental versus predicted temperature (°C) using a 1:1 correspondence line. **b**) Histogram for temperature residuals for all test sets. **c**) Comparison of experimental versus predicted water content (wt.%). **d**) Histogram of water content residuals for all test sets. **e**) Comparison of experimental versus predicted pressure (MPa). **f**) Histogram of pressure residuals for all test sets.

2.3.4 Barometry

We tested an H_2O-dependent (Figure 2.5e, 2.5f) and an H_2O-independent barometer (Figure 2.4e, f), as H_2O contents are not always well-constrained for natural systems, especially for lavas lacking glassy melt inclusions suitable for direct H_2O analysis. The barometers are calibrated using a reduced dataset by removing all high-pressure experiments (>500 MPa) due to the low number and narrow compositional range of experiments undertaken at higher pressures (Figure 2.1b). Atmospheric pressure experiments were also removed, as the pressure output for nominally anhydrous natural samples is likely to skew towards 0.1 MPa when H_2O is used as an additional input variable. Both barometers perform surprisingly well with 10-fold cross-validation (H_2O-dependent RMSE: 76 MPa; Figure 2.5e, f, H_2O-independent RMSE: 92 MPa, Figure 2.4e, f), which is confirmed by their predictive performance in the test set (H_2O-dependent RMSE: 76 MPa, H_2O-independent RMSE: 91 MPa; Figure 2.4e and 2.5e), although the R^2 values for both barometers are low (H_2O-dependent R^2: 0.60; H_2O-independent R^2: 0.42; Table S2.2). In terms of residuals, the addition of H_2O as an input enables 85% of the predictions to be within ±100 MPa of the actual experimental pressure for the H_2O-dependent barometer (Figure 2.5f), compared to 76% for the H_2O-independent (Figure 2.4f) barometer. None of the melt components has a dominant control on the pressure predictions, where it would be expected that Al_2O_3 and Na_2O would correlate with pressure (Blundy, 2022). Instead, the algorithm mainly uses SiO_2, TiO_2, FeO_t, MgO and CaO, suggesting that, like the hygrometers, the extent of differentiation helps constrain pressure values in a hypothetical P-T(-H_2O) space. The test set predictions for both barometers are systematically slightly offset as predictions

<300 MPa tend to slightly overestimate pressures, while the barometers underestimate pressures >300 MPa, evident from the low gradient values and higher intercepts (Figure 2.4e and 2.5e). However, this pattern is similar to other barometers (e.g., clinopyroxene-based; Wieser et al., 2023b), likely amplified by the significant data gaps present at higher pressures in calibration datasets and the weak pressure trends with compositional variables. This highlights a crucial objective to conduct systematic experiments >300 MPa for a wide array of melt compositions to explore pressure correlations fully. To compare our H_2O-dependent barometer performance, we use the Putirka (2008) plagioclase-liquid barometer (Equation 25a; calibrated for P <2000 MPa) due to both barometers requiring an H_2O input. A comparison of model performance statistics (Figure 2.5f, Figure 2.6c) for the ML and plagioclase-liquid barometer highlights that the ML barometer represents a significant improvement in reducing pressure estimate errors.

2.3.5 Anorthite content

We tested a model to estimate the composition of plagioclase (An content) as a function of the melt composition. The An model performs well without incorporating temperature and H_2O as additional input variables (Figure 2.4g, 2.4h), with a median 5.8 mol% RMSE during cross-validation (Figure 2.2d) and a 5.8 mol% RMSE for the test set data (Figure 2.4g). The test data show no overall systematic offset across the An content range with low intercept and MBE values and a gradient close to 1 (Figure 2.4g), attesting to the model's high accuracy of anorthite predictions. Furthermore, 69% of the predictions have residuals within ± 5 mol% of the measured values and 91% within ± 10 mol%. CaO, SiO_2 and MgO in the melt are the dominant controls on

plagioclase anorthite content (Figure S2.5), consistent with thermodynamic and experimental studies (e.g., Panjasawatong et al., 1995; Namur et al., 2012; Neave and Namur, 2022). With temperature exerting a primary control on plagioclase composition (e.g., Kudo and Weill, 1970; Lange et al., 2009; Figure 2.1c), the combination of CaO, SiO_2 and MgO also likely acts as an indirect proxy for temperature aiding anorthite predictions. We test our ML anorthite model against model E of Putirka (2005), calibrated on experiments with SiO_2 contents of 42–73 wt.% and plagioclase compositions of An_{40-95} (Figure 2.6d). We also compare the anhydrous test set experiments with the T-independent models (Eq. 33–35) of Namur et al. (2012) that are all calibrated on 0.1 MPa experiments with SiO_2 contents of 43–78 wt.% and plagioclase compositions of An_{39-100}. The ability of the ML model to predict equilibrium plagioclase compositions is greater than that of model E (Figure 2.6d; e.g., RMSE: 14 mol%), whereas, for the subset of anhydrous experiments, Namur et al.'s (2012) T-independent empirical models (Eq. 33–35) have comparable RMSE, intercept and gradient values to the ML model, although the latter has a lower MBE and a higher R^2 value (Figure 2.4h, Figure 2.6d).

2.3.6 Plagioclase saturation

Before using any of the models, melt compositions must first be checked for plagioclase saturation to avoid erroneous model predictions, which may prove difficult if petrographic or microanalytical analyses cannot be carried out on samples, for example, in cases where only bulk rock data are available. We have thus developed a classifier model to screen matrix glass compositions for plagioclase saturation. We compiled an approximately equal amount of non-plagioclase to plagioclase-saturated experimental

data (n_{total} = 2206) for calibration (Table S2.3) and used the classification mode of the algorithm to train the model. The classifier cross-validation process is the same as all the regression models outlined in Section 2.2, but 5-fold cross-validation was used instead. We use the classification accuracy metric to evaluate the classifier's performance, which is a ratio describing the number of correct predictions to the total number of predictions. The mean accuracy from cross-validation and test sets is 87% and 90%, respectively. Table S2.4 presents an average test set confusion matrix, which summarises all sets of classification results (i.e., false positive, false negative, true positive, true negative) from all test set replications and indicates low rates of false positive (~4%) and false negative (~5%) classifications. SiO_2, MgO and Al_2O_3 are the main melt oxides used to classify plagioclase saturation, corresponding to SiO_2 and MgO acting as differentiation and temperature proxies and Al_2O_3 indicating the onset of plagioclase crystallisation.

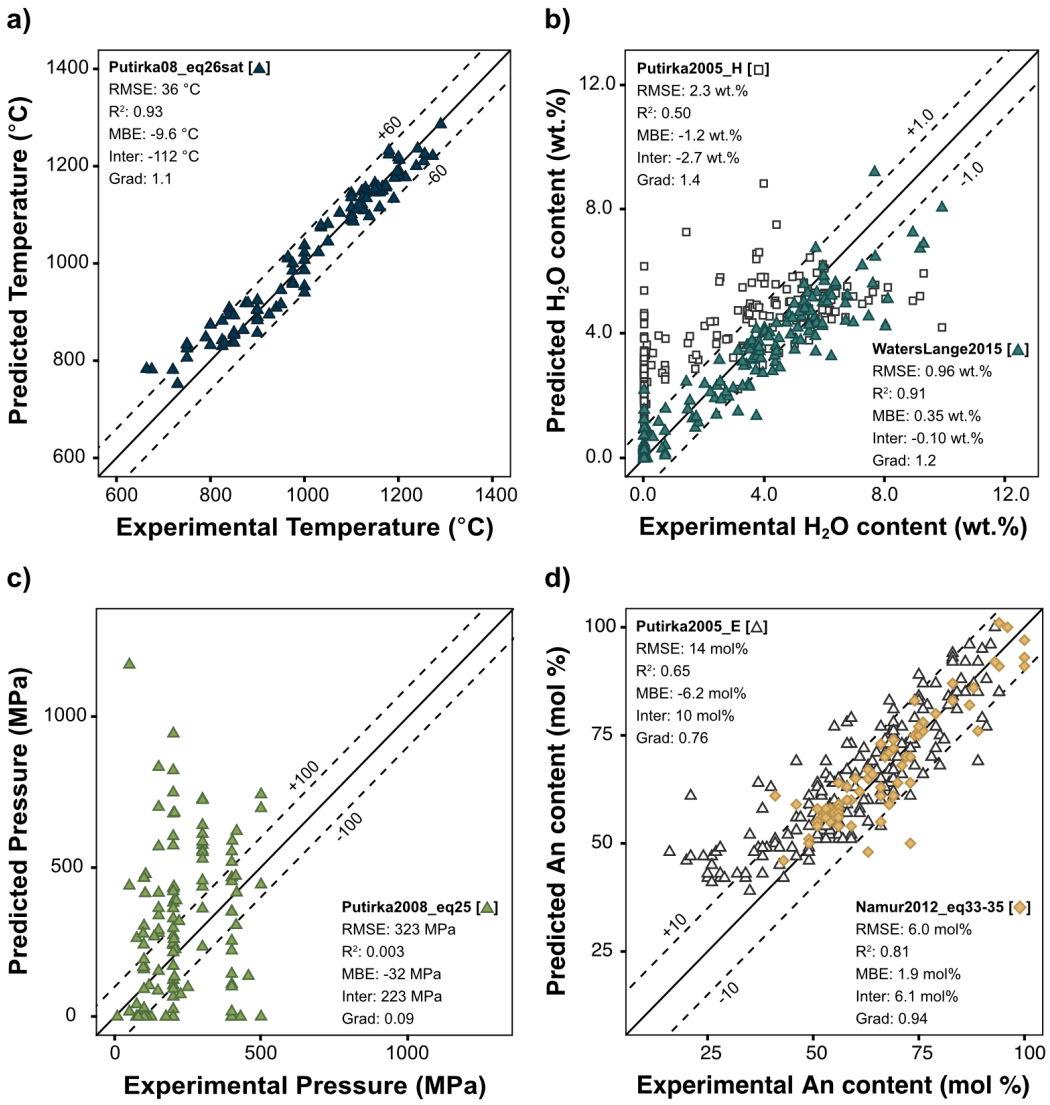

Figure 2.6 Testing set performance using other plagioclase-melt or melt models. Only the best-performing testing set is shown for each model, but the testing set statistics reflect the average RMSE, R^2, MBE, intercept and gradient values across all ten testing sets. **a**) Plot of experimental temperature versus the predicted temperature (°C) derived from liquid thermometer (Equation 26) of Putirka (2008). **b**) Plot of experimental water contents versus the predicted water contents (wt.%) resulting from plagioclase-melt hygrometers of Putirka (Model H; 2008) and Waters and Lange (2015). **c**) Plot of experimental pressure versus the predicted pressure (MPa) resulting from the plagioclase-melt barometer (Equation 25) of Putirka (2008). **d**) Plot of experimental anorthite content versus the predicted anorthite content (mol%) derived from the plagioclase-melt equilibria model of Putirka (Model E; 2008) and Namur et al. (Equations 33–35; 2012).

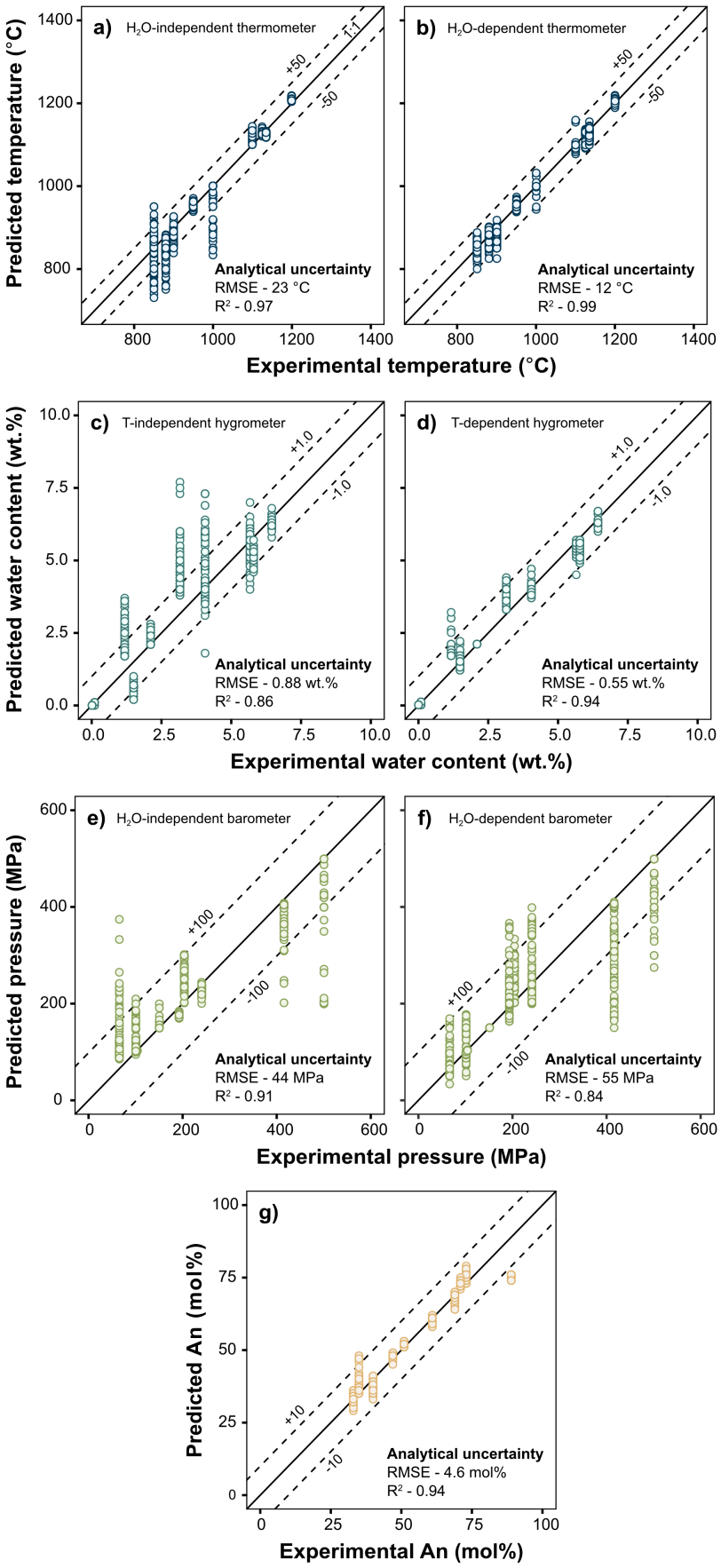
a) H2O-independent thermometer
1:1
+50
-50
Analytical uncertainty
RMSE - 23 °C
R² - 0.97
b) H2O-dependent thermometer
+50
-50
Analytical uncertainty
RMSE - 12 °C
R² - 0.99
Predicted temperature (°C)
Experimental temperature (°C)
c) T-independent hygrometer
+1.0
-1.0
Analytical uncertainty
RMSE - 0.88 wt.%
R² - 0.86
d) T-dependent hygrometer
+1.0
-1.0
Analytical uncertainty
RMSE - 0.55 wt.%
R² - 0.94
Predicted water content (wt.%)
Experimental water content (wt.%)
e) H2O-independent barometer
+100
-100
Analytical uncertainty
RMSE - 44 MPa
R² - 0.91
f) H2O-dependent barometer
+100
-100
Analytical uncertainty
RMSE - 55 MPa
R² - 0.84
Predicted pressure (MPa)
Experimental pressure (MPa)
g)
+10
-10
Analytical uncertainty
RMSE - 4.6 mol%
R² - 0.94
Predicted An (mol%)
Experimental An (mol%)

Figure 2.7 Monte Carlo simulations of electron microprobe analytical errors and their effect on resulting temperatures (**a**, H_2O-independent thermometer; **b**, H_2O-dependent thermometer), water contents (**c**, T-independent hygrometer; **d**, T-dependent hygrometer), pressures (**e**, H_2O-independent barometer; **f**, H_2O-dependent barometer), and anorthite content estimates (**g**).

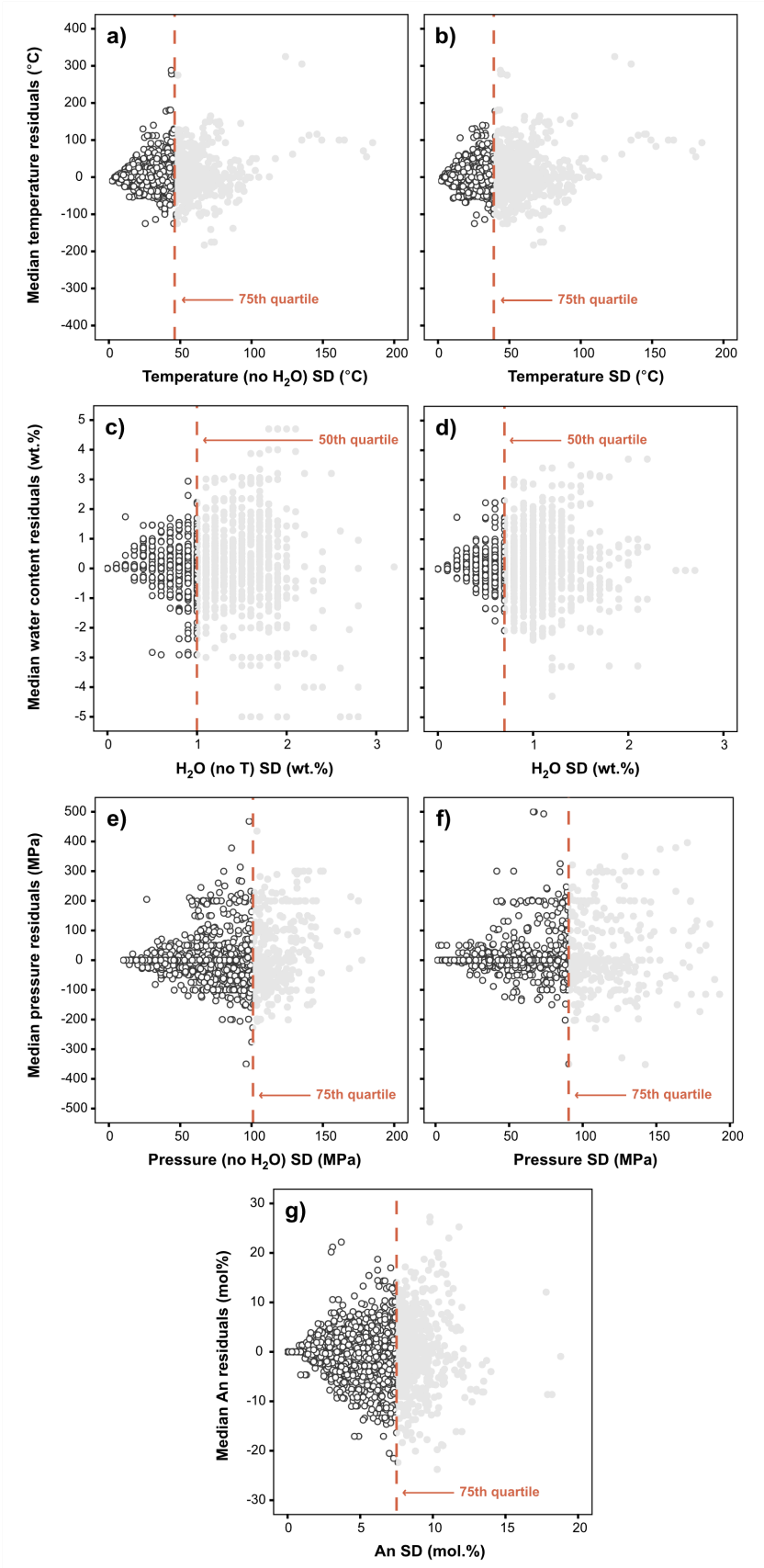
a)
b)
c)
d)
e)
f)
g)
Median temperature residuals (°C)
Median water content residuals (wt.%)
Median pressure residuals (MPa)
Median An residuals (mol%)
75th quartile
50th quartile
Temperature (no H2O) SD (°C)
Temperature SD (°C)
H2O (no T) SD (wt.%)
H2O SD (wt.%)
Pressure (no H2O) SD (MPa)
Pressure SD (MPa)
An SD (mol.%)

Figure 2.8 Investigation of appropriate filters for all testing set P-T-H_2O-An estimates using the standard deviation. Dashed lines highlight the 50th or 75th standard deviation quartile, where estimates (light grey points) greater than this value should be removed. The testing set statistics reflect the average RMSE, R^2, MBE, intercept and gradient values across all ten testing sets after filtering. **a**) Median temperature residuals versus temperature SD (°C) for the H_2O-independent thermometer. **b**) Median temperature residuals versus temperature SD (°C) for the H_2O-dependent thermometer. **c**) Median water content residuals versus water content SD (wt.%) for the T-independent hygrometer. **d**) Median water content residuals versus water content SD (wt.%) for the T-dependent hygrometer. **e**) Median pressure residuals versus pressure SD (MPa) for the H_2O-independent barometer. **f**) Median pressure residuals versus pressure SD (MPa) for the H_2O-dependent barometer. **g**) Median anorthite content residuals versus anorthite content SD (mol%) for the plagioclase-melt equilibria model.

2.3.7 Further model limitations

The P-T-H_2O bounds of the calibration dataset represent one major limitation of all models. The models presented here should *never* be used outside the calibration range since the ML algorithm is unsuited for extrapolation. Additional experimental constraints covering key calibration dataset gaps will help to increase model accuracy (i.e., Figure 2.1). Furthermore, hygrometer RMSEs could be improved if more experimental glasses were analysed for H_2O to increase the number of direct H_2O measurements within the calibration dataset, rather than using indirect H_2O estimates from solubility models (e.g., Papale et al., 2006; Zhang et al., 2007; Ghiorso and Gualda, 2015) or the 'volatiles by difference' method (e.g., Devine et al., 1995) that can have large uncertainties (e.g., Hughes et al., 2019). This is particularly true for low-H_2O melts.

The precision of P-T-H_2O-An predictions is influenced by the analytical error of the melt composition itself (e.g., Gualda and Ghiorso, 2014; Wieser et al., 2023d). To evaluate the impact of analytical (i.e. electron microprobe; EPMA) uncertainties on P-T-H_2O-An predictions, we used a series of Monte Carlo simulations to create major element oxide variation based on ten melt compositions (Table S5). These ten melts were chosen to represent the compositional range and experimental conditions throughout the calibration dataset. For each melt, new compositions are generated from its original oxide values with noise added from a normal distribution, with the variation deriving from a weighted mean of one sigma standard deviation EPMA values (Table S2.5) from a subset of experiments (n=400). The ten melts generated 2000 melt compositions by running a 200-time simulation per composition and subsequently used as inputs for each melt model. The simulations for the melt-only models highlight that

analytical errors impose a limit on precision of ±44 MPa for pressure, ±23 °C for temperature, ±0.56 wt.% for H_2O (with temperature), ±0.88 wt.% for H_2O (without temperature) and ±4.6 mol % for anorthite content (Figure 2.7a-g). In addition, analytical uncertainties associated with H_2O content inputs measured by SIMS or FTIR/Raman spectroscopy were also tested using a pessimistic averaged standard deviation of 0.5 wt.% (Ulmer et al., 2018), as few studies provide sufficient information (e.g., the number of analyses, standard deviations of water measurements) to calculate a reliable weighted mean. The simulations indicate that melt and water analytical errors can limit H_2O-dependent model precision to ±55 MPa for pressure and ±12 °C for temperature (Figure 2.7b, 2.7f). Both sets of simulations indicate the sensitivity of our hygrothermobarometers to analytical uncertainty. The simulations emphasise the need to undertake careful preparation (i.e., tephra extraction, Cooper et al., 2019; glass alteration recognition) and analytical procedures (i.e. EPMA; Hayward, 2012) of matrix glass and inclusions to minimise the chemical variability of susceptible oxides (e.g., MgO, SiO_2) that would affect subsequent predictions.

2.4 Model application

To test the calibrations of our melt models, we have applied them to two tectonically contrasting, well-constrained volcanic systems (Mount St Helens, USA; Bárðarbunga, Iceland). We compare the predicted values to previous estimates calculated from various thermobarometers, direct H_2O measurements from melt inclusions and seismic information about the sub-volcanic systems. For each application, we also discuss the different ways the models can be used depending on whether the melt H_2O contents

are known, along with suggestions on P-T-H_2O-An and plagioclase saturation prediction filtering.

2.4.1 May–October 1980 eruption, Mount St Helens, USA

On May 18th 1980, the north flank of Mount St Helens' edifice collapsed, depressurising the shallow magmatic 'cryptodome' and triggering a lateral blast. Eruption of a 24 km-high Plinian column ensued later that day as depressurisation reached the deeper magmatic system. Smaller explosive eruptions characterise subsequent activity from May to October 1980; a series of dome-forming extrusions within the crater followed through to October 1986. Here, we apply the models to matrix glass and plagioclase-hosted melt inclusion data (*n*=151) in Blundy et al. (2008) from the 1980 eruptive activity of Mount St Helens. The erupted magma was a porphyritic dacite (or silicic andesite) with ~63 wt.% SiO_2 and ~35 vol% phenocrysts. The melt phase, both as inclusions and matrix glass, was uniformly rhyolitic and thought to be saturated in plagioclase, orthopyroxene, magnetite and ilmenite (Rutherford et al., 1985). Amphibole also occurs as a phenocryst phase but shows some evidence of resorption or breakdown, notably in the dome-forming magmas. Clinopyroxene is a rare phenocryst phase in some samples.

In cases where constraints for all variables (P-T-H_2O-An) are unknown, the variables should be recovered sequentially in the following order: An → T → H_2O → P (Figure S2.6). Before using the P-T-H_2O models, glass compositions must demonstrate that they represent a melt in equilibrium with plagioclase, which can be achieved by comparing An predictions from the plagioclase-equilibria model with natural plagioclase

rim compositions. The uncertainty of a prediction is given as the standard deviation and can be used to filter model predictions to further reduce errors. This has been shown by Weber and Blundy (2024), where their model test set predictions using a random forest algorithm display higher residual variance as the standard deviation (SD) increases. Figure 2.8 presents our melt model test set residuals against the SD and shows most of the divergence begins from the 75th quartile of SD values. In addition, our test set statistics display an improvement with overall lower RMSE, intercept, and MBE values with higher gradients and R^2 values, especially in the case of the barometers (Figure 2.8e, f). Therefore, we recommend filtering values by removing the top 25% SD values. However, for the hygrometers, removing values above the 50th quartile is more effective at reducing the variance (Figure 2.8). Although filtering will lead to fewer predictions, removing predictions with the highest variance will ensure more robust estimates. Accordingly, we only report the filtered estimates from all models with both applications (Table S2.6).

The range of plagioclase compositions in equilibrium with the compositional range of plagioclase-hosted melt inclusions and matrix glasses is estimated at An_{21-51} (matrix mode: 45 mol%; MI mode: 39 mol%), which corresponds within error to the dominant plagioclase rim composition (An_{47}; Berlo et al., 2007), suggesting that the plagioclase rims were in equilibrium with the host melt.

The H_2O-independent thermometer returns mean melt inclusion and matrix glass temperatures of 892 ± 55°C (SD) and 885 ± 49°C (Figure 2.9a), respectively; the former is consistent with melt inclusion temperatures (853–941 °C; Blundy et al. 2006) calculated using the plagioclase-liquid thermometer of Putirka (2005). Fe-Ti oxide

thermometry estimates (816–958 °C; Blundy et al., 2008), calculated using the oxide recalculation procedure of Spencer and Lindsley (1981) and the thermometer of Andersen and Lindsley (1988), extend the range to slightly higher temperatures. This slight magma heating may reflect latent heat release due to crystallisation or magma recharge (Blundy et al., 2006) and the ability of Fe-Ti oxides to re-equilibrate chemically on short timescales (Venezky & Rutherford, 1999).

We next use the predicted melt temperatures as inputs for the T-dependent hygrometer, producing H_2O estimates between 2.6 and 6.5 wt.%. We also performed Monte Carlo error propagation using the temperature SD from the thermometer outputs (Figure 2.9a), and the mean uncertainty for H_2O predictions across all samples is ± 1.4 wt.%. A full description of the error propagation method is presented in Text S1. The majority of melt inclusion H_2O estimates are broadly similar to measured analyses by SIMS (Blundy et al., 2006). In contrast, the estimated H_2O contents for the groundmass and the highly silicic (>75 wt.% SiO_2) melt inclusions are significantly higher than measured (Figure 2.9b) values, reflecting extensive degassing upon eruption and the failure of the melt to evolve chemically in response (Blundy and Cashman, 2005). The comparison could also signify a deficit of highly silicic calibration experiments with low dissolved water concentrations where the H_2O estimates diverge more profoundly from the 1:1 line. Furthermore, Figure 2.9b highlights that H_2O content negatively correlates with SiO_2, consistent with Blundy and Cashman (2005) suggesting decompression crystallisation of the groundmass and plagioclase phenocrysts during ascent.

Finally, using the predicted H_2O contents as inputs for the H_2O-dependent barometer, the pressure predictions returned values between 50 and 250 MPa (matrix

mean: 117 ± 44 MPa, melt inclusion mean: 98 ± 41 MPa; Figure 2.9a). We again performed error propagation using the water uncertainty from the hygrometer resulting in a mean uncertainty of ± 38 MPa across all samples. The mean uncertainties for both H_2O and pressure highlight that even with two unknown variables for a system, the accumulated errors are still low enough to obtain informative interpretations; we include the error propagation capability within the provided R scripts (Cutler, 2024). The H_2O-independent barometer returns similar pressures of 44–225 MPa (matrix mean: 113 ± 59 MPa, melt inclusion mean: 109 ± 61 MPa; Figure 2.9a). The pressures, particularly from melt inclusions, overlap with saturation pressure values (melt inclusion range: 7–282 MPa; mean: 97 MPa, matrix range: 3.2–20.6 MPa; matrix mean: 8.3 MPa; Figure 2.9a) from Blundy et al. (2010) estimated using Papale's et al. (2006) H_2O-CO_2 solubility model. Overall, the main pressure range (44–250 MPa) resulting from both barometers convert to depths of 1.2–6.9 km using a 2700 kg/m^3 average crustal density. Scandone and Malone (1985) estimated a reservoir depth of 7–9 km using net edifice subsidence measured from electronic tiltmeters. An aseismic zone was also mapped at 7 km extending vertically for 6+ km from earthquake hypocentres, and interpreted as a reservoir connected to the surface (Scandone and Malone, 1985; Lees, 1992). Although our mean melt inclusion and matrix glass crystallisation depths are shallower than geophysical estimates, the glass compositions likely record crystallisation conditions

during pre-eruptive ascent from the top of the storage region, consistent with the H_2O vs. SiO_2 relationship in Figure 2.9b.

2.4.2 2014-2015 Holuhraun eruption, Bárðarbunga, Iceland

In mid-August 2014, a dyke propagated laterally NE from Bárðarbunga volcano, and by the end of August, the dyke caused a fissure eruption at the Holuhraun lava field (Ágústsdóttir et al., 2016). The Holuhraun magma was a phenocryst poor (≤5 vol%), highly vesicular olivine tholeiite (Halldórsson et al. (2018). Here, we use the basaltic matrix glass and plagioclase-hosted melt inclusion (with post-entrapment crystallisation corrections) data (*n*=251) from Hartley et al. (2018) and Halldórsson et al. (2018). Matrix glass data points with <6 wt.% MgO were removed, as they represent syn-emplacement crystallisation conditions (Halldórsson et al., 2018). We tested the plagioclase-saturation classifier on the matrix glasses (*n*=175), and 174 compositions are predicted to be plagioclase-saturated, in agreement with the petrography of the samples (plagioclase-olivine-clinopyroxene-Fe-Ti oxides; Halldórsson et al., 2018). Although the one matrix glass composition that failed the classifier test could be, in fact, plagioclase-saturated (i.e., false negative), the main objective of the classifier approach is to eliminate any false positives that may generate inaccurate pressure estimates. We thus removed that single matrix glass composition for subsequent P-T-H_2O-An estimations.

The modal equilibrium plagioclase compositions predicted for matrix glasses and melt inclusions are An_{70} and An_{79}, respectively, consistent with the estimated equilibrium plagioclase phenocryst rims and microphenocrysts using the plagioclase-melt equilibria model of Namur et al. (2012) ($An_{64.5–75}$; Halldórsson et al., 2018; Figure

2.10a). A subset of melt inclusions with higher MgO contents (>8 wt.%) have higher An_{75-82} contents, which likely represent the entrainment of plagioclase phenocrysts from mush horizons (Hartley et al., 2018) now in disequilibrium with the surrounding melt.

Temperature reconstructions for matrix glasses and melt inclusions (<8 wt.% MgO) with the H_2O-independent thermometer yield mean temperatures of 1157 ± 14 °C and 1176 ± 13.5 °C (Figure 2.10b), respectively, consistent with clinopyroxene-liquid thermometry (1161 ± 11 °C; Neave et al., 2019) using Eq. 33 of Putirka (2008), whereas the primitive melt inclusions (higher MgO) record a higher mean temperature of 1203 ± 13 °C (Figure 2.10b). Water contents in matrix glasses and melt inclusions have been measured by FTIR and calculated, accounting for diffusive re-equilibration of melt inclusions, to be in the range of 0.13–0.7 wt.% (Bali et al., 2018; Hartley et al., 2018). If water contents are constrained to a specific range, we can use the H_2O-dependent barometer differently by testing various water values as inputs. We use values of 0.0, 0.3, 0.6 and 0.9 wt.% (Figure 2.10b), and the barometer returns matrix glass pressures of 151–296 MPa (mean: 185 ± 94 MPa) and melt inclusion pressures of 116–300 MPa (mean: 164 ± 99 MPa) for all water contents; varying the water content results in only minor pressure differences (~10–25 MPa). The H_2O-independent barometer gives similar matrix glass and melt inclusion pressures ranging between 191–202 MPa (mean: 191 ± 97 MPa) and 176–300 MPa (mean: 176 ± 91 MPa), respectively. All mean pressure predictions are in good agreement (Figure 2.10c) with pressures estimated by clinopyroxene-liquid barometry (232 ± 86 MPa, Neave et al., 2019; using iterative thermobarometric calculations including Eq. 1 of Neave and Putirka, 2017 and Eq. 33 of Putirka, 2008), plagioclase-liquid barometry (141 ± 247 MPa, Geiger et al., 2014; using

Eq. 25a of Putirka, 2008), and OPAM thermal minima (matrix glass: 210 ± 70 MPa, melt inclusion: 350 ± 170 MPa) with OPAM pressures for primitive melt inclusions returning values of 300–350 MPa (Hartley et al., 2018). Using a crustal density of 2860 kg/m^{-3} (Carlson and Herrick, 1990), the ML barometer pressures convert to depths of 3.4–8.8 km. These depths correspond well with the location of earthquake hypocentres (5–7 km; Figure 2.10c) associated with dyke propagation prior to the eruption (Sigmundsson et al., 2015; Ágústsdóttir et al., 2019).

Overall, the plagioclase-saturated melt models are effective at identifying the last-equilibrated composition of plagioclase crystals with the host melt and characterising key intensive variables at both Mount St Helens and Bárðarbunga. This is shown by the generally good agreement of predictions with previous petrological estimates using different models (e.g., volatile solubility and mineral ± melt thermobarometry) and geophysical data. Comparison of direct H_2O measurements with hygrometer predictions may also provide insight into which melt inclusions have likely lost water during ascent and their original water contents. The models offer the additional benefit of not requiring saturation of a specific mineral assemblage, which can often restrict the application of many melt-based models (e.g., olivine-plagioclase-augite, OPAM, Yang et al., 1996; Rhyolite-MELTS; Gualda and Ghiorso, 2014).

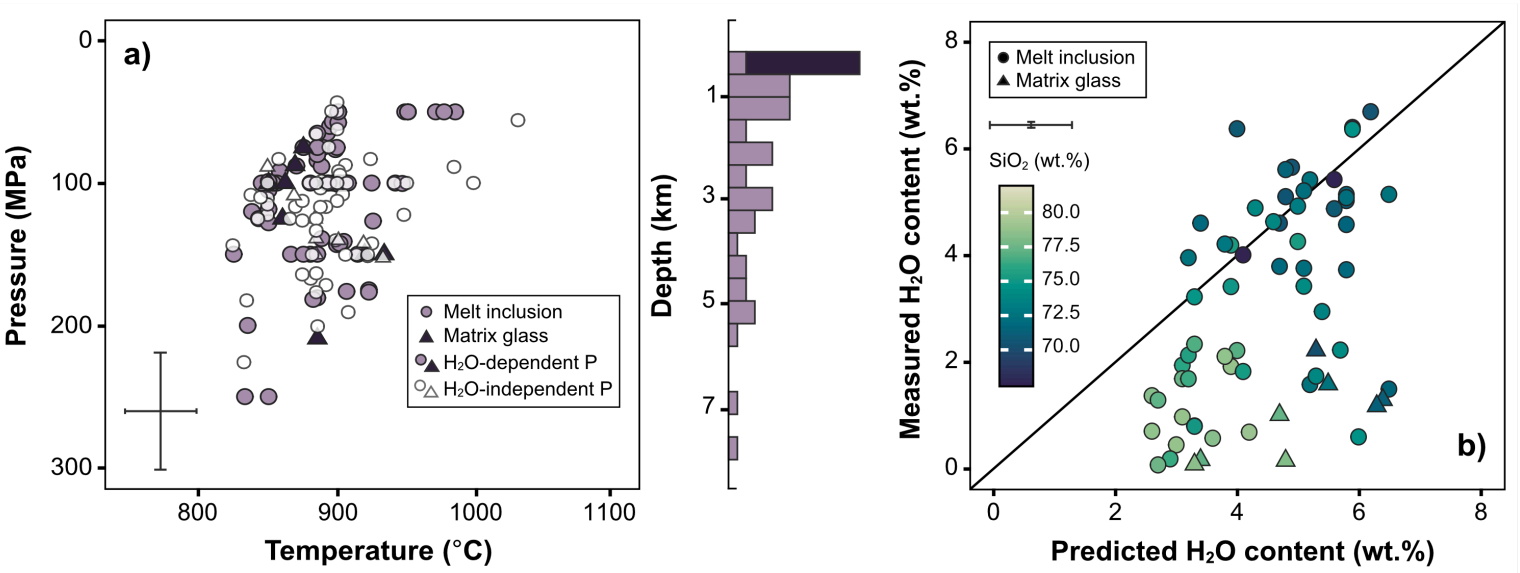

Figure 2.9 a) Filtered temperature (°C) vs. pressure (MPa) predictions of melt inclusions and matrix glasses (*n*=113) for the 1980 Mount St Helens eruption, estimated using the H_2O-independent melt thermometer, H_2O-dependent melt barometer, and H_2O-independent melt barometer. The histogram on the right displays the saturation pressures of matrix glass (*n*=29) and melt inclusions (*n*=45) from Blundy et al. (2010), estimated using the Papale et al. (2006) solubility model. **b**) SIMS water contents versus predicted water contents using the T-dependent hygrometer. Colour coding reflects SiO_2 content (wt.%) in melt.

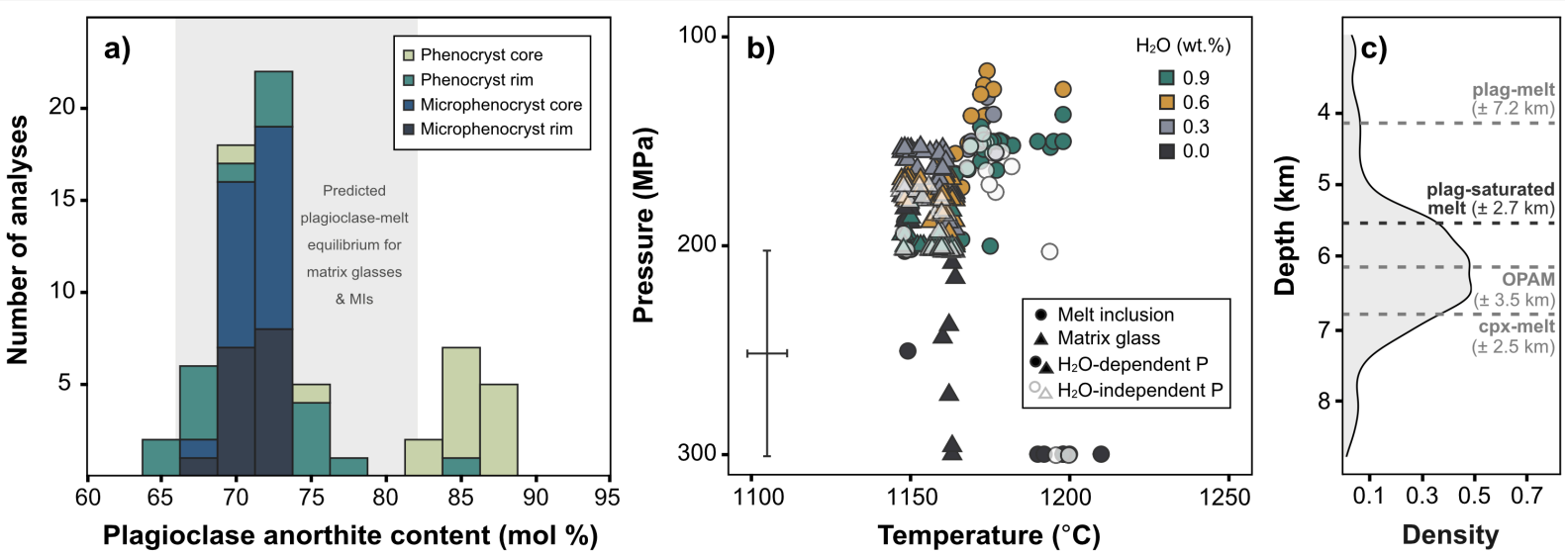

Figure 2.10 a) Stacked histogram displaying the composition of plagioclase phenocrysts and microphenocryst crystals from the 2014-2015 Holuhraun eruption (data from Halldórsson et al. (2018), with the light grey field representing the plagioclase compositions predicted to be in equilibrium with the carrier liquid and inclusions. **b**) Filtered temperature (°C) versus pressure (MPa) predictions of melt inclusions and matrix glasses (*n*=248) for the 2014-2015 Holuhraun eruption, calculated using the H_2O-independent melt thermometer, H_2O-dependent melt barometer, and H_2O-independent melt barometer. Colour coding depicts the H_2O content (wt.%) used as H_2O-dependent barometer input. **c**) Density distribution of dyke seismicity (15th to 30th August 2014; *n*=273) prior to the eruption; data taken from Ágústsdóttir et al. (2019). Dashed lines represent mean depths estimated from plagioclase-liquid barometry (Geiger et al., 2014) using Eq. 25a (Putirka, 2008), plagioclase-saturated melt barometry (mean of both matrix glass and melt inclusion pressures estimated from both H_2O-dependent and H_2O-independent melt barometers), OPAM barometry (Hartley et al., 2018), and clinopyroxene-liquid barometry (Neave et al., 2019) using iterative thermobarometric calculations of Eq. 1 of Neave and Putirka (2017) and Eq. 33 of Putirka (2008).

2.5 Conclusions

We have tested various plagioclase-based hygrothermobarometric models using either plagioclase-melt or melt chemistry and developed an updated plagioclase-melt equilibria model, with all models calibrated using random forest machine learning. Our results show that the melt compositional information holds nearly all the P-T-H_2O information rather than the plagioclase, resulting in the melt and plagioclase-melt models returning incredibly similar cross-validation RMSE values. Test set RMSEs for the melt + T/H_2O and melt-only models are 25°C–35°C, 0.65 –1.00 wt.%, 74–88 MPa and 5.8 mol% for temperature, water content, pressure and anorthite content, respectively. In general, the models provide an enhanced prediction accuracy for P-T-H_2O and anorthite content values. Furthermore, the T and H_2O-independent melt hygrothermobarometers allow predictions to be obtained without requiring additional inputs (P/T/H_2O) that are inherent within all previous plagioclase-based hygrothermobarometer formulations (Putirka, 2008; Waters and Lange, 2015; Masotta and Mollo, 2019), introducing further uncertainties that are often not propagated. For the T and H_2O-dependent melt hygrothermobarometers, there are dedicated R scripts (Cutler, 2024) to perform error propagation (for either measured H_2O contents, independent T values, or calculated T/ H_2O estimates from melt-only models) or to generate predictions with T or H_2O values in a given range.

Application of the melt thermometers and hygrometers is suitable for a wide range of plagioclase-bearing melts across temperatures of 664–1355 °C and H_2O contents ≤11.20 wt.%; the melt barometer is only appropriate for pressures of ≤500 MPa. The plagioclase-saturated melt models were applied to melt inclusions and matrix glass from

the 1980 Mount St Helens eruption and 2014-2015 Holuhraun eruption, with P-T-H_2O-An predictions returning consistent constraints comparable to estimates and observations from melt inclusion analyses, geophysical data, and previous hygrothermobarometric and plagioclase-equilibria models. The new set of models enables a quick assessment of plagioclase-melt equilibrium and an insight into the last-equilibrated P-T-H_2O conditions of plagioclase-bearing magmas in the upper crust.

References

Ágústsdóttir, T., Woods, J., Greenfield, T., Green, R. G., White, R. S., Winder, T., Brandsdóttir, B., Steinthórsson, S., & Soosalu, H. (2016). Strike-slip faulting during the 2014 Bárðarbunga-Holuhraun dike intrusion, central Iceland. *Geophysical Research Letters*, *43*(4), 1495-1503. DOI: https://doi.org/10.1002/2015GL067423

Ágústsdóttir, T., Winder, T., Woods, J., White, R. S., Greenfield, T., & Brandsdóttir, B. (2019). Intense seismicity during the 2014–2015 Bárðarbunga-Holuhraun rifting event, Iceland, reveals the nature of dike-induced earthquakes and caldera collapse mechanisms. *Journal of Geophysical Research: Solid Earth*, *124*(8), 8331-8357. DOI: https://doi.org/10.1029/2018JB016010

Andersen, D. J., & Lindsley, D. H. (1988). Internally consistent solution models for Fe-Mg-Mn-Ti oxides; Fe-Ti oxides. *American Mineralogist*, *73*(7-8), 714-726.

Bali, E., Hartley, M.E., Halldórsson, S.A., Gudfinnsson, G.H. and Jakobsson, S. (2018). Melt inclusion constraints on volatile systematics and degassing history of the 2014–2015 Holuhraun eruption, Iceland. *Contributions to Mineralogy and Petrology*, *173*, pp.1-21. DOI: 1 https://doi.org/0.1007/s00410-017-1434-1

Bamber, E.C., La Spina, G., Arzilli, F., de'Michieli Vitturi, M., Polacci, M., Hartley, M.E., Petrelli, M., Fellowes, J. and Burton, M. (2022). Basaltic Plinian eruptions at Las Sierras-Masaya volcano driven by cool storage of crystal-rich magmas. *Communications Earth & Environment*, *3*(1), p.253. DOI: https://doi.org/10.1038/s43247-022-00585-5

Berlo, K., Blundy, J., Turner, S. and Hawkesworth, C. (2007). Textural and chemical variation in plagioclase phenocrysts from the 1980 eruptions of Mount St. Helens, USA. *Contributions to Mineralogy and Petrology*, *154*, pp.291-308. DOI: https://doi.org/10.1007/s00410-007-0194-8

Blundy, J. (2022). Chemical differentiation by mineralogical buffering in crustal hot zones. *Journal of Petrology*, *63*(7), egac054. DOI: https://doi.org/10.1093/petrology/egac054

Blundy, J. and Cashman, K. (2005). Rapid decompression-driven crystallization recorded by melt inclusions from Mount St. Helens volcano. *Geology*, *33*(10), pp.793-796. DOI: https://doi.org/10.1130/G21668.1

Blundy, J., Cashman, K. and Humphreys, M. (2006). Magma heating by decompression-driven crystallization beneath andesite volcanoes. *Nature*, *443*(7107), pp.76-80. DOI: https://doi.org/10.1038/nature05100

Blundy, J., Cashman, K.V., Berlo, K., Sherrod, D.R., Scott, W.E. and Stauffer, P.H. (2008). Evolving magma storage conditions beneath Mount St. Helens inferred from chemical variations in melt inclusions from the 1980–1986 and current (2004–2006) eruptions. *US Geological Survey professional paper*, *1750*, pp.755-790.

Blundy, J., Cashman, K. V., Rust, A., & Witham, F. (2010). A case for CO2-rich arc magmas. *Earth and Planetary Science Letters*, *290*(3-4), 289-301. DOI: https://doi.org/10.1016/j.epsl.2009.12.013

Blundy, J. (2022). Chemical Differentiation by Mineralogical Buffering in Crustal Hot Zones. *Journal of Petrology*, *63*(7), egac054. DOI: https://doi.org/10.1093/petrology/egac054

Caricchi, L., Townsend, M., Rivalta, E. and Namiki, A. (2021). The build-up and triggers of volcanic eruptions. *Nature Reviews Earth & Environment*, *2*(7), pp.458-476. DOI: https://doi.org/10.1038/s43017-021-00174-8

Carlson, R.L. and Herrick, C.N. (1990). Densities and porosities in the oceanic crust and their variations with depth and age. *Journal of Geophysical Research: Solid Earth*, *95*(B6), pp.9153-9170. DOI: https://doi.org/10.1029/JB095iB06p09153

Cassidy, M., Manga, M., Cashman, K. and Bachmann, O. (2018). Controls on explosive-effusive volcanic eruption styles. *Nature communications*, *9*(1), p.2839. DOI: https://doi.org/10.1038/s41467-018-05293-3

Cassidy, M., Ebmeier, S. K., Helo, C., Watt, S. F. L., Caudron, C., Odell, A., ... & Castro, J. M. (2019). Explosive eruptions with little warning: Experimental petrology and volcano monitoring observations from the 2014 eruption of Kelud, Indonesia. *Geochemistry, Geophysics, Geosystems*, *20*(8), 4218-4247. DOI: https://doi.org/10.1029/2018GC008161

Cooper, C. L., Savov, I. P., & Swindles, G. T. (2019). Standard chemical-based tephra extraction methods significantly alter the geochemistry of volcanic glass shards. *Journal of Quaternary Science*, *34*(8), 697-707. DOI: https://doi.org/10.1002/jqs.3169

Cutler, K.S. (2024). kyra-cutler/Plag-saturated-melt-P-T-H2O-An: v1.0 (v1.0). *Zenodo.* DOI: https://doi.org/10.5281/zenodo.10841557

Devine, J. D., Gardner, J. E., Brack, H. P., Layne, G. D., & Rutherford, M. J. (1995). Comparison of microanalytical methods for estimating H2O contents of silicic volcanic glasses. *American Mineralogist*, *80*(3-4), 319-328. DOI: https://doi.org/10.2138/am-1995-3-413

Feig, S.T., Koepke, J. and Snow, J.E. (2010). Effect of oxygen fugacity and water on phase equilibria of a hydrous tholeiitic basalt. *Contributions to Mineralogy and Petrology*, *160*, pp.551-568. DOI: https://doi.org/10.1007/s00410-010-0493-3

Fuhrman, M. L., & Lindsley, D. H. (1988). Ternary-feldspar modeling and thermometry. *American mineralogist*, *73*(3-4), 201-215.

Gavrilenko, M., Krawczynski, M., Ruprecht, P., Li, W. and Catalano, J.G. (2019). The quench control of water estimates in convergent margin magmas. *American Mineralogist: Journal of Earth and Planetary Materials*, *104*(7), pp.936-948. DOI: https://doi.org/10.2138/am-2019-6735

Geiger, H., Mattsson, T., Deegan, F. M., Troll, V. R., Burchardt, S., Gudmundsson, Ó., Tryggvason, A., Krumbholz, M., & Harris, C. (2016). Magma plumbing for the 2014–2015 Holuhraun eruption, Iceland. *Geochemistry, Geophysics, Geosystems*, *17*(8), 2953-2968. DOI: https://doi.org/10.1002/2016GC006317

Ghiorso, M.S. and Gualda, G.A. (2015). An H 2 O–CO 2 mixed fluid saturation model compatible with rhyolite-MELTS. *Contributions to Mineralogy and Petrology*, *169*, pp.1-30. DOI: https://doi.org/10.1007/s00410-015-1141-8

Giordano, D., Russell, J.K. and Dingwell, D.B. (2008). Viscosity of magmatic liquids: a model. *Earth and Planetary Science Letters*, *271*(1-4), pp.123-134. DOI: https://doi.org/10.1016/j.epsl.2008.03.038

Giordano, G. and Caricchi, L. (2022). Determining the state of activity of transcrustal magmatic systems and their volcanoes. *Annual Review of Earth and Planetary Sciences*, *50*, pp.231-259. DOI: https://doi.org/10.1146/annurev-earth-032320-084733

Gualda, G.A. and Ghiorso, M.S. (2014). Phase-equilibrium geobarometers for silicic rocks based on rhyolite-MELTS. Part 1: Principles, procedures, and evaluation of the method. *Contributions to Mineralogy and Petrology*, *168*, pp.1-17. DOI: https://doi.org/10.1007/s00410-014-1033-3

Halldórsson, S.A., Bali, E., Hartley, M.E., Neave, D.A., Peate, D.W., Guðfinnsson, G.H., Bindeman, I., Whitehouse, M.J., Riishuus, M.S., Pedersen, G.B. and Jakobsson, S. (2018). Petrology and geochemistry of the 2014–2015 Holuhraun eruption, central Iceland: compositional and mineralogical characteristics, temporal variability and magma storage. *Contributions to Mineralogy and Petrology*, *173*, pp.1-25. DOI: https://doi.org/10.1007/s00410-018-1487-9

Hartley, M.E., Bali, E., Maclennan, J., Neave, D.A. and Halldórsson, S.A. (2018). Melt inclusion constraints on petrogenesis of the 2014–2015 Holuhraun eruption, Iceland. *Contributions to Mineralogy and Petrology*, *173*, pp.1-23. DOI: https://doi.org/10.1007/s00410-017-1435-0

Hayward, C. (2012). High spatial resolution electron probe microanalysis of tephras and melt inclusions without beam-induced chemical modification. *The Holocene*, *22*(1), 119-125. DOI: https://doi.org/10.1177/0959683611409777

Helz, R.T. and Thornber, C.R. (1987). Geothermometry of Kilauea Iki lava lake, Hawaii. *Bulletin of volcanology*, *49*, pp.651-668. DOI: https://doi.org/10.1007/BF01080357

Higgins, O., Sheldrake, T. and Caricchi, L. (2022). Machine learning thermobarometry and chemometry using amphibole and clinopyroxene: a window into the roots of an arc volcano (Mount Liamuiga, Saint Kitts). *Contributions to Mineralogy and Petrology*, *177*(1), p.10. DOI: https://doi.org/10.1007/s00410-021-01874-6

Hilley, G. E. (ed.), Brodsky, E.E., Roman, D., Shillington, D. J., Brudzinski, M., Behn, M., Tobin, H. and the SZ4D RCN (2022). SZ4D Implementation Plan. Stanford Digital Repository.

Hirschmann, M. M., Ghiorso, M. S., Davis, F. A., Gordon, S. M., Mukherjee, S., Grove, T. L., M. Krawczynski, E. Medard, & Till, C. B. (2008). Library of Experimental Phase Relations (LEPR): A database and Web portal for experimental magmatic phase equilibria data. *Geochemistry, Geophysics, Geosystems*, *9*(3). DOI: https://doi.org/10.1029/2007GC001894

Housh, T.B. and Luhr, J.F. (1991). Plagioclase-melt equilibria in hydrous systems. *American Mineralogist*, *76*(3-4), pp.477-492.

Hughes, E. C., Buse, B., Kearns, S. L., Blundy, J. D., Kilgour, G., & Mader, H. M. (2019). Low analytical totals in EPMA of hydrous silicate glass due to sub-surface charging: Obtaining accurate volatiles by difference. *Chemical Geology*, *505*, 48-56. https://doi.org/10.1016/j.chemgeo.2018.11.015

Husen, A., Almeev, R.R. and Holtz, F. (2016). The effect of H2O and pressure on multiple saturation and liquid lines of descent in basalt from the Shatsky Rise. *Journal of Petrology*, *57*(2), pp.309-344. DOI: https://doi.org/10.1093/petrology/egw008

Iacovino, K., Matthews, S., Wieser, P.E., Moore, G.M. and Bégué, F. (2021). VESIcal Part I: An open-source thermodynamic model engine for mixed volatile (H2O-CO2) solubility in silicate melts. *Earth and Space Science*, *8*(11), p.e2020EA001584. DOI: https://doi.org/10.1029/2020EA001584

Jorgenson, C., Higgins, O., Petrelli, M., Bégué, F. and Caricchi, L. (2022). A Machine Learning-Based Approach to Clinopyroxene Thermobarometry: Model Optimization and Distribution for Use in Earth Sciences. *Journal of Geophysical Research: Solid Earth*, *127*(4), p.e2021JB022904. DOI: https://doi.org/10.1029/2021JB022904

Krawczynski, M.J., Grove, T.L. and Behrens, H. (2012). Amphibole stability in primitive arc magmas: effects of temperature, H2O content, and oxygen fugacity. *Contributions to Mineralogy and Petrology*, *164*(2), pp.317-339. DOI: https://doi.org/10.1007/s00410-012-0740-x

Kudo, A.M. and Weill, D.F. (1970). An igneous plagioclase thermometer. *Contributions to Mineralogy and Petrology*, *25*(1), pp.52-65. DOI: https://doi.org/10.1007/BF00383062

Kuhn, M. (2008). Building predictive models in R using the caret package. *Journal of statistical software*, *28*, pp.1-26. DOI: https://doi.org/10.18637/jss.v028.i05

Lange, R.A., Frey, H.M. and Hector, J. (2009). A thermodynamic model for the plagioclase-liquid hygrometer/thermometer. *American Mineralogist*, *94*(4), pp.494-506. DOI: https://doi.org/10.2138/am.2009.3011

Lees, J. M. (1992). The magma system of Mount St. Helens: Non-linear high-resolution P-wave tomography. *Journal of volcanology and geothermal research*, *53*(1-4), 103-116.

Le Maitre, R.W., Bateman, P., Dudek, A. and Keller, J. (1989). Lameyre Le Bas. *MJ, Sabine, PA, Schmid, R., Sorensen, H., Streckeisen, A., Woolley, AR, Zanettin, B*, p.193.

Li, X. and Zhang, C. (2022). Machine Learning Thermobarometry for Biotite-Bearing Magmas. *Journal of Geophysical Research: Solid Earth*, *127*(9), p.e2022JB024137. DOI: https://doi.org/10.1029/2022JB024137

Liu, E.J., Cashman, K.V., Miller, E., Moore, H., Edmonds, M., Kunz, B.E., Jenner, F. and Chigna, G. (2020). Petrologic monitoring at Volcán de Fuego, Guatemala. *Journal of Volcanology and Geothermal Research*, *405*, p.107044. DOI: https://doi.org/10.1016/j.jvolgeores.2020.107044

Longhi, J., Fram, M.S., Vander Auwera, J. and Montieth, J.N. (1993). Pressure effects, kinetics, and rheology of anorthositic and related magmas. *American Mineralogist*, *78*(9-10), pp.1016-1030.

Masotta, M. and Mollo, S. (2019). A new plagioclase-liquid hygrometer specific to trachytic systems. *Minerals*, *9*(6), p.375. DOI: https://doi.org/10.3390/min9060375

Namur, O., Charlier, B., Toplis, M.J. and Vander Auwera, J. (2012). Prediction of plagioclase-melt equilibria in anhydrous silicate melts at 1-atm. *Contributions to Mineralogy and Petrology*, *163*, pp.133-150. DOI: https://doi.org/10.1007/s00410-011-0662-z

Neave, D.A. and Putirka, K.D. (2017). A new clinopyroxene-liquid barometer, and implications for magma storage pressures under Icelandic rift zones. *American Mineralogist*, *102*(4), pp.777-794. DOI: https://doi.org/10.2138/am-2017-5968

Neave, D.A., Bali, E., Guðfinnsson, G.H., Halldórsson, S.A., Kahl, M., Schmidt, A.S. and Holtz, F. (2019). Clinopyroxene–liquid equilibria and geothermobarometry in natural and experimental tholeiites: the 2014–2015 Holuhraun eruption, Iceland. *Journal of Petrology*, *60*(8), pp.1653-1680. DOI: https://doi.org/10.1093/petrology/egz042

Neave, D.A. and Namur, O. (2022). Plagioclase archives of depleted melts in the oceanic crust. *Geology*, *50*(7), pp.848-852. DOI: https://doi.org/10.1130/G49840.1

Panjasawatwong, Y., Danyushevsky, L.V., Crawford, A.J. and Harris, K.L. (1995). An experimental study of the effects of melt composition on plagioclase-melt equilibria at 5 and 10 kbar: implications for the origin of magmatic high-An plagioclase. *Contributions to Mineralogy and Petrology*, *118*, pp.420-432. DOI: https://doi.org/10.1007/s004100050024

Papale, P., Moretti, R. and Barbato, D. (2006). The compositional dependence of the saturation surface of H2O+ CO2 fluids in silicate melts. *Chemical Geology*, *229*(1-3), pp.78-95. DOI: https://doi.org/10.1016/j.chemgeo.2006.01.013

Petrelli, M., Caricchi, L. and Perugini, D. (2020). Machine learning thermo-barometry: Application to clinopyroxene-bearing magmas. *Journal of Geophysical Research: Solid Earth*, *125*(9), p.e2020JB020130. DOI: https://doi.org/10.1029/2020JB020130

Pritchard, M.E., Mather, T.A., McNutt, S.R., Delgado, F.J. and Reath, K. (2019). Thoughts on the criteria to determine the origin of volcanic unrest as magmatic or non-magmatic. *Philosophical Transactions of the Royal Society A*, *377*(2139), p.20180008. DOI: https://doi.org/10.1098/rsta.2018.0008

Putirka, K.D. (2005). Igneous thermometers and barometers based on plagioclase+ liquid equilibria: Tests of some existing models and new calibrations. *American Mineralogist*, *90*(2-3), pp.336-346. DOI: https://doi.org/10.2138/am.2005.1449

Putirka, K.D. (2008). Thermometers and barometers for volcanic systems. *Reviews in mineralogy and geochemistry*, *69*(1), pp.61-120. DOI: https://doi.org/10.2138/rmg.2008.69.3

Putirka, K. (2016). Amphibole thermometers and barometers for igneous systems and some implications for eruption mechanisms of felsic magmas at arc volcanoes. *American Mineralogist*, *101*(4), pp.841-858. DOI: https://doi.org/10.2138/am-2016-5506

R Core Team, R. (2013). R: A language and environment for statistical computing.

Rutherford, M.J., Sigurdsson, H., Carey, S. and Davis, A. (1985). The May 18, 1980, eruption of Mount St. Helens: 1. Melt composition and experimental phase equilibria. *Journal of Geophysical Research: Solid Earth*, *90*(B4), pp.2929-2947. DOI: https://doi.org/10.1029/JB090iB04p02929

Saunders, K., Blundy, J., Dohmen, R. and Cashman, K. (2012). Linking petrology and seismology at an active volcano. *Science*, *336*(6084), pp.1023-1027. DOI: https://doi.org/10.1126/science.1220066

Scandone, R., & Malone, S. D. (1985). Magma supply, magma discharge and readjustment of the feeding system of Mount St. Helens during 1980. *Journal of Volcanology and Geothermal Research*, *23*(3-4), 239-262.

Sigmundsson, F., Hooper, A., Hreinsdóttir, S., Vogfjörd, K.S., Ófeigsson, B.G., Heimisson, E.R., Dumont, S., Parks, M., Spaans, K., Gudmundsson, G.B. and Drouin, V. (2015). Segmented lateral dyke growth in a rifting event at Bárðarbunga volcanic system, Iceland. *Nature*, *517*(7533), pp.191-195. DOI: https://doi.org/10.1038/nature14111

Spencer, K. J., & Lindsley, D. H. (1981). A solution model for coexisting iron–titanium oxides. *American Mineralogist*, *66*(11-12), 1189-1201.

Stock, M.J., Bagnardi, M., Neave, D.A., Maclennan, J., Bernard, B., Buisman, I., Gleeson, M.L. and Geist, D. (2018). Integrated petrological and geophysical constraints on magma system architecture in the western Galápagos Archipelago: insights from Wolf volcano. *Geochemistry, Geophysics, Geosystems*, *19*(12), pp.4722-4743. DOI: https://doi.org/10.1029/2018GC007936

Thomson, A.R., Kohn, S.C., Prabhu, A. and Walter, M.J. (2021). Evaluating the formation pressure of diamond-hosted majoritic garnets: A machine learning majorite barometer. *Journal of Geophysical Research: Solid Earth*, *126*(3), p.e2020JB020604. DOI: https://doi.org/10.1029/2020JB020604

Ulmer, P., Kaegi, R. and Müntener, O. (2018). Experimentally derived intermediate to silica-rich arc magmas by fractional and equilibrium crystallization at 1· 0 GPa: an evaluation of phase relationships, compositions, liquid lines of descent and oxygen fugacity. *Journal of Petrology*, *59*(1), pp.11-58. DOI: https://doi.org/10.1093/petrology/egy017

Venezky, D.Y. and Rutherford, M.J. (1999). Petrology and Fe–Ti oxide reequilibration of the 1991 Mount Unzen mixed magma. *Journal of Volcanology and Geothermal Research*, *89*(1-4), pp.213-230. DOI: https://doi.org/10.1016/S0377-0273(98)00133-4

Waters, L.E. and Lange, R.A. (2015). An updated calibration of the plagioclase-liquid hygrometer-thermometer applicable to basalts through rhyolites. *American Mineralogist*, *100*(10), pp.2172-2184. DOI: https://doi.org/10.2138/am-2015-5232

Weber, G., & Blundy, J. (2024). A machine learning-based thermobarometer for magmatic liquids. *Journal of Petrology*, egae020. DOI: https://doi.org/10.1093/petrology/egae020

Whitaker, M. L., Nekvasil, H., Lindsley, D. H., & Difrancesco, N. J. (2007). The role of pressure in producing compositional diversity in intraplate basaltic magmas. *Journal of Petrology*, *48*(2), 365-393. DOI: https://doi.org/10.1093/petrology/egl063

Wieser, P. E., Gleeson, M. L. M., Matthews, S., DeVitre, C. and Gazel, E. (2023a). Determining the Pressure –Temperature – Composition (P-T-X) conditions of magma storage. DOI: https://doi.org/10.31223/X50M44

Wieser, P., Kent, A.J. and Till, C., (2023b). Barometers behaving badly II: A critical evaluation of Cpx-only and Cpx-Liq thermobarometry in variably-hydrous arc magmas. *Journal of Petrology*, *64*(8), egad050. DOI: https://doi.org/10.1093/petrology/egad050

Wieser, P., Petrelli, M., Lubbers, J., Wieser, E., Ozaydin, S., Kent, A. and Till, C. (2023c). Thermobar: an open-source Python3 tool for thermobarometry and hygrometry. *Volcanica*, *5*(2), pp.349-384. DOI: https://doi.org/10.30909/vol.05.02.349384

Wieser, P.E., Kent, A.J., Till, C.B., Donovan, J., Neave, D.A., Blatter, D.L. and Krawczynski, M.J. (2023d). Barometers Behaving Badly I: Assessing the Influence of Analytical and Experimental Uncertainty on Clinopyroxene Thermobarometry Calculations at Crustal Conditions. *Journal of Petrology*, *64*(2), p.egac126. DOI: https://doi.org/10.1093/petrology/egac126

Wright, M. N., & Ziegler, A. (2017). ranger: A Fast Implementation of Random Forests for High Dimensional Data in C++ and R. *Journal of Statistical Software*, *77*(1), 1–17. DOI: https://doi.org/10.18637/jss.v077.i01

Yang, H.J., Kinzler, R.J. and Grove, T.L. (1996). Experiments and models of anhydrous, basaltic olivine-plagioclase-augite saturated melts from 0.001 to 10 kbar. *Contributions to Mineralogy and Petrology*, *124*(1), pp.1-18. DOI: https://doi.org/10.1007/s004100050169

Yip, S.T.H., Biggs, J., Edmonds, M., Liggins, P. and Shorttle, O. (2022). Contrasting volcanic deformation in arc and ocean island settings due to exsolution of magmatic water. *Geochemistry, Geophysics, Geosystems*, *23*(7), p.e2022GC010387. DOI: https://doi.org/10.1029/2022GC010387

Zhang, Y., Xu, Z., Zhu, M. and Wang, H. (2007). Silicate melt properties and volcanic eruptions. *Reviews of Geophysics*, *45*(4). DOI: https://doi.org/10.1029/2006RG000216

Zimmer, M.M., Plank, T., Hauri, E.H., Yogodzinski, G.M., Stelling, P., Larsen, J., Singer, B., Jicha, B., Mandeville, C. and Nye, C.J. (2010). The role of water in generating the calc-alkaline trend: new volatile data for Aleutian magmas and a new tholeiitic index. *Journal of Petrology*, *51*(12), pp.2411-2444. DOI: https://doi.org/10.1093/petrology/egq062

Supplementary Materials for…

'Plagioclase-saturated melt hygrothermobarometry and plagioclase-melt equilibria using machine learning'

Contents of this file

- Text S2.1
- Figures S2.1 to S2.6
- Table S2.2
- Table S2.4

Additional Supporting Information (see separate .xlsx spreadsheets)

- **Table S2.1** Calibration dataset for the thermometers, hygrometers, barometers, and the anorthite content model.
- **Table S2.3** Calibration dataset for the plagioclase-saturated classifier.
- **Table S2.5** Monte Carlo analytical uncertainty simulation input (ten experimental liquid compositions + weighted mean errors of electron microprobe glass oxide analyses) and output.
- **Table S2.6** Summary of petrological estimates (An-T-H_2O-P) for the Mount St Helens (USA) and Holuhraun (Iceland) eruptions.

Text S2.1

The ML H_2O-independent thermometer and T-dependent hygrometer provide an uncertainty value (standard deviation; SD) from the T or H_2O prediction of each individual glass compositional analysis. For n=50, a uniform distribution within the SD on every temperature or water content estimate predicted by the H_2O-independent thermometer and T-dependent hygrometer is sampled. For example, if the thermometer returns a value of 900 °C and an SD of ± 50 °C, 50 points are sampled between 850–950 °C according to a uniform distribution. All 50 temperature/water content estimates are then input into the T-dependent hygrometer or H_2O-dependent barometer for each glass analysis. The maximum absolute difference to the mean value is the maximum uncertainty associated with a given pre-eruptive water content/pressure estimate.

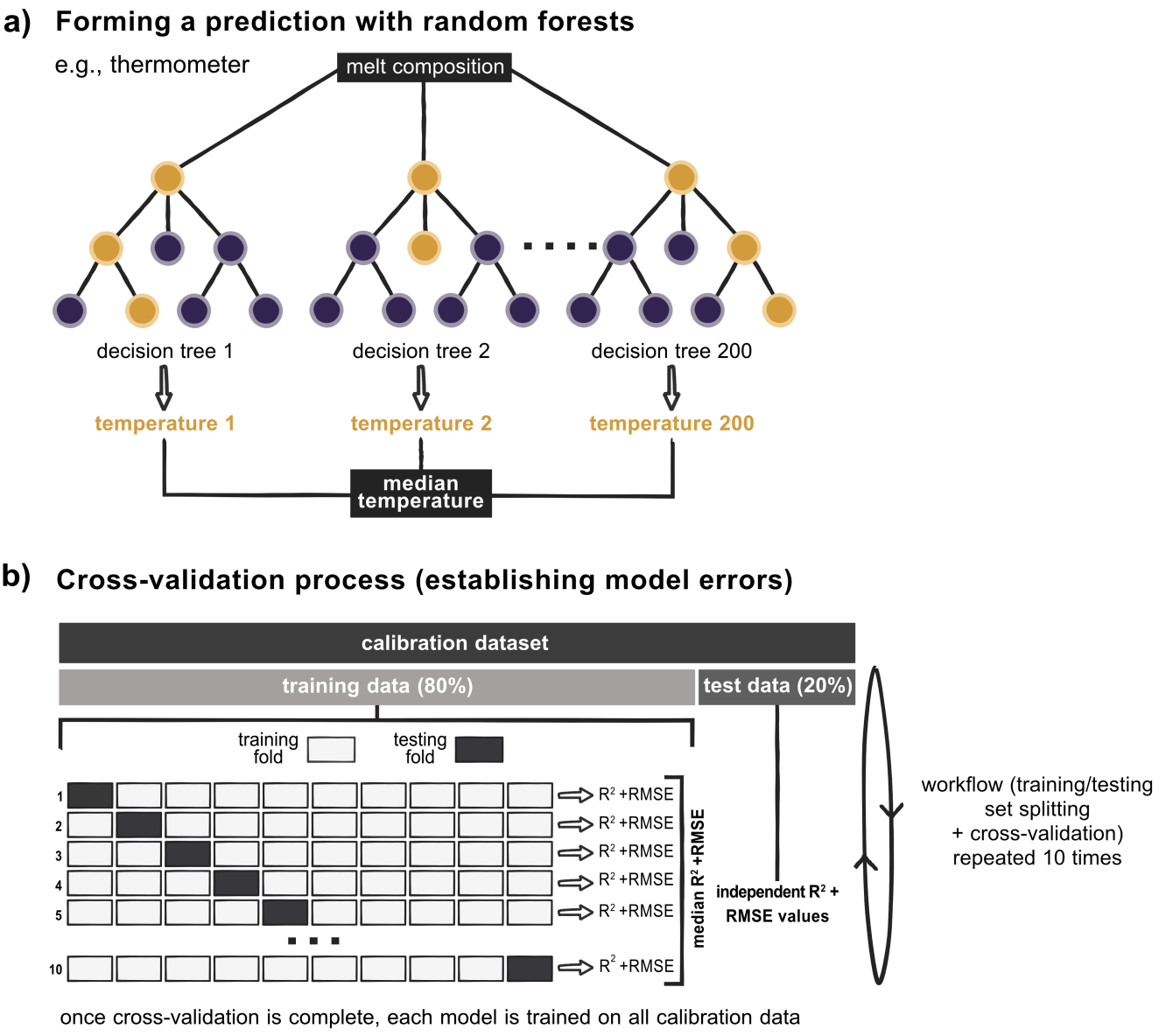

Figure S2.1 Summary diagrams of the random forest algorithm and the cross-validation process. **a**) Simplified diagram of a random forest thermometer displaying how a temperature prediction forms via averaging of multiple decision trees. **b**) Schematic of 10-fold cross-validation.

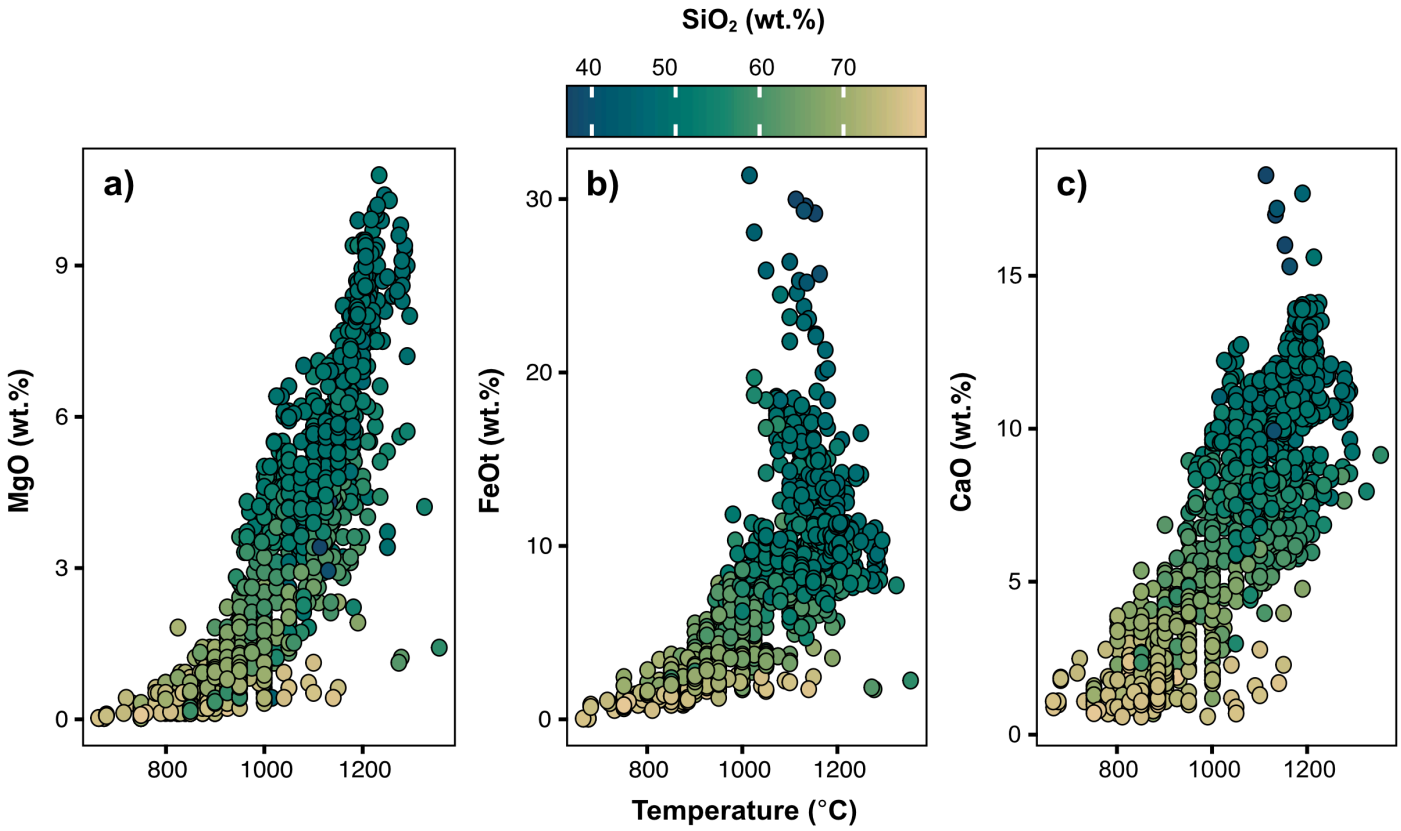

Figure S2.2 Plots illustrating the strong non-linearity between temperature and (a) MgO (wt.%), (b) FeOt (wt.%), and (c) CaO (wt.%) in the liquid. Colour coding reflects the SiO_2 (wt.%) of the liquid.

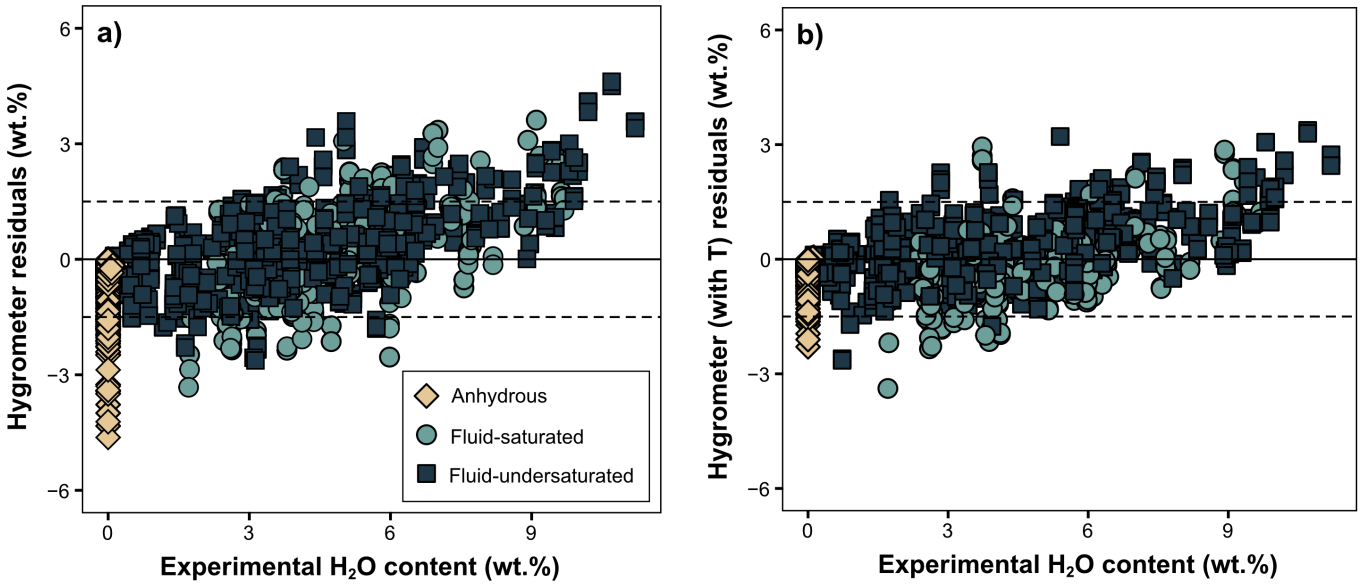

Figure S2.3 Residuals of the T-independent hygrometer (**a**) and the T-dependent hygrometer (**b**) against experimental H_2O content.

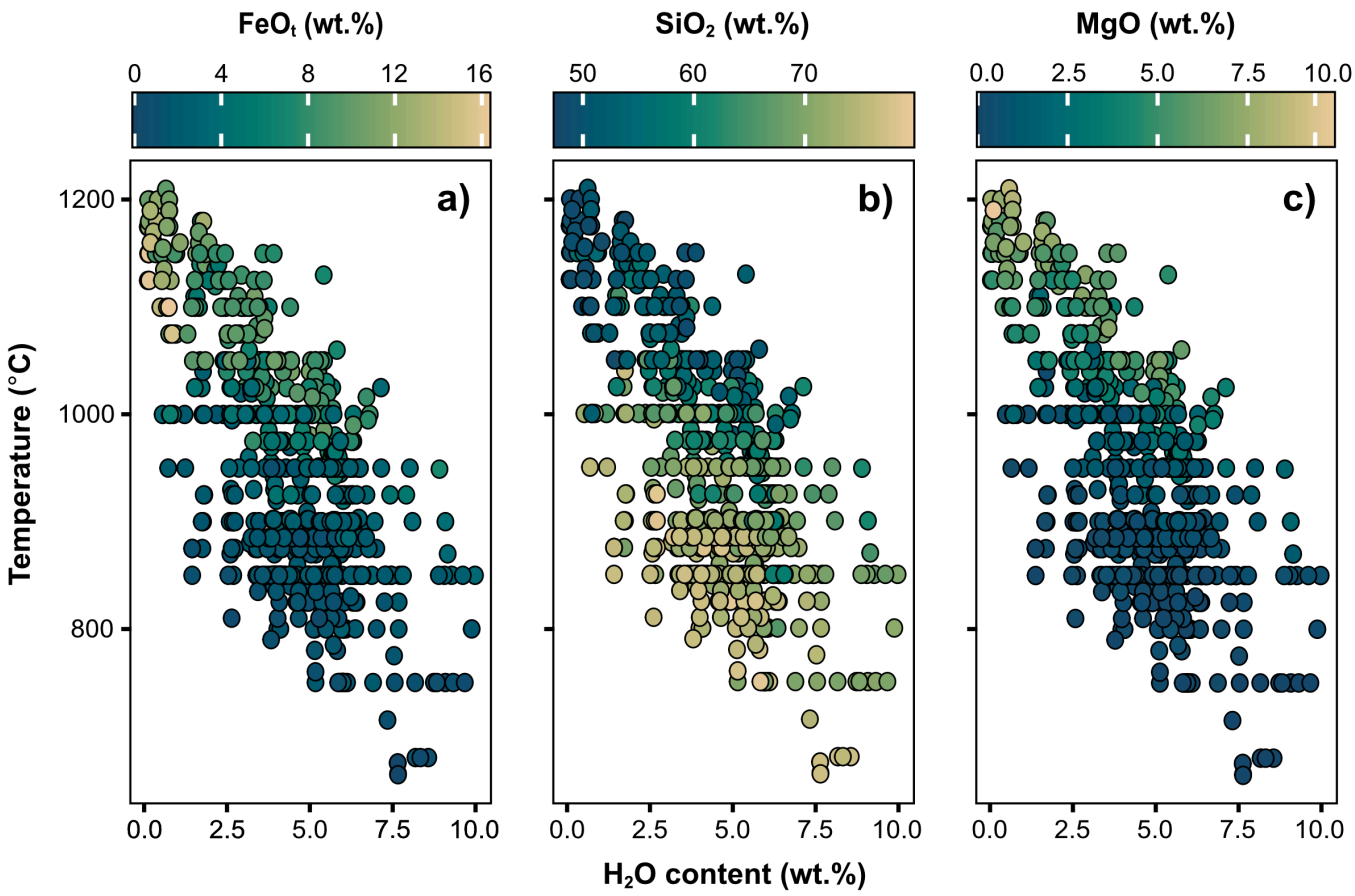

Figure S2.4 Temperature vs. H_2O (wt.%) of experimental glass compositions with colour coding showing the (**a**) FeO_t (wt.%), (**b**) SiO_2 (wt.%), and (**c**) MgO (wt.%) contents in the liquid. Note that all anhydrous experiments were removed.

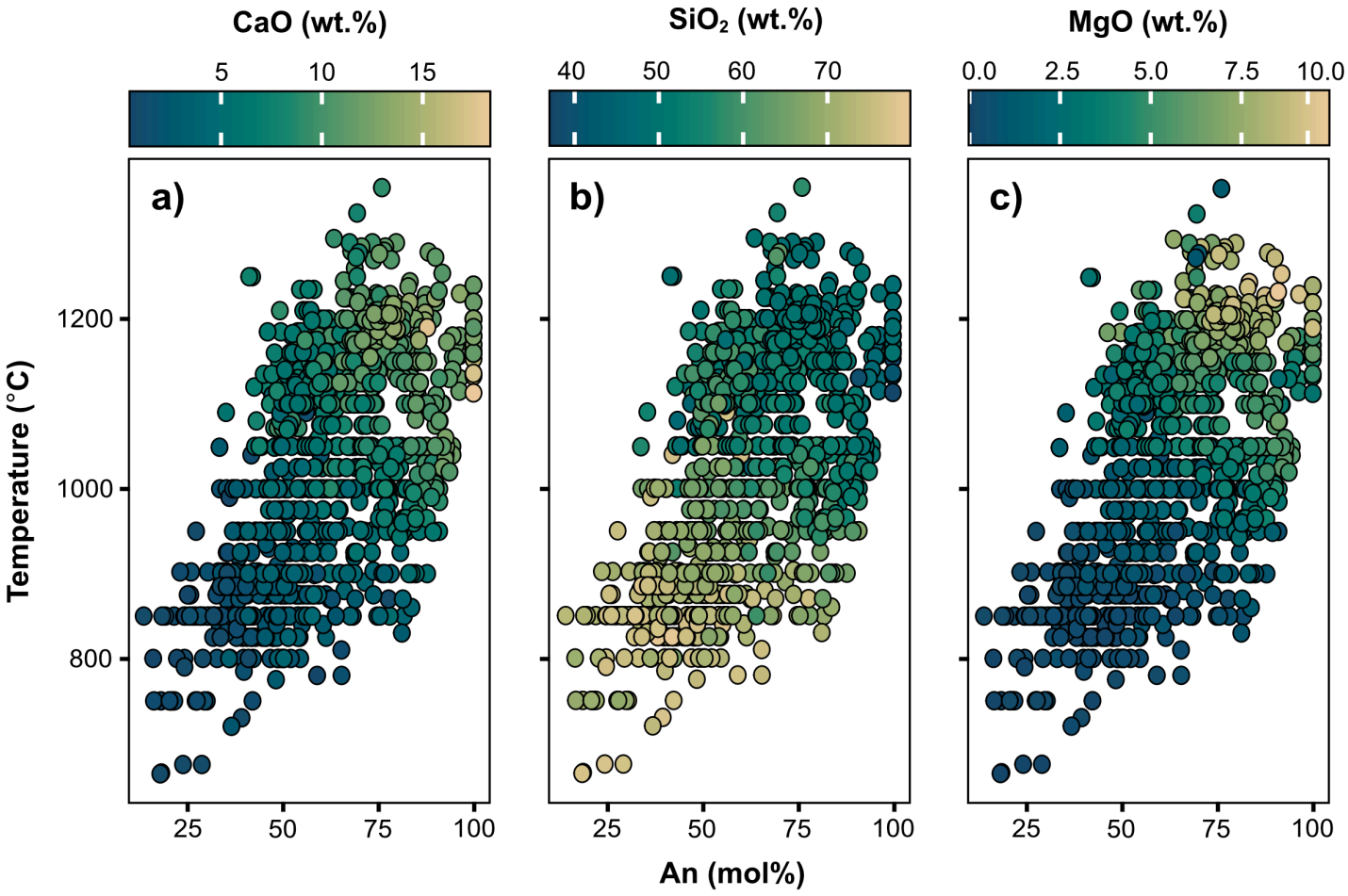

Figure S2.5 Temperature of experimental glass compositions vs. An content (mol%) of experimental plagioclase with colour coding showing the (**a**) CaO (wt.%), (**b**) SiO_2 (wt.%), and (**c**) MgO (wt.%) contents in the liquid.

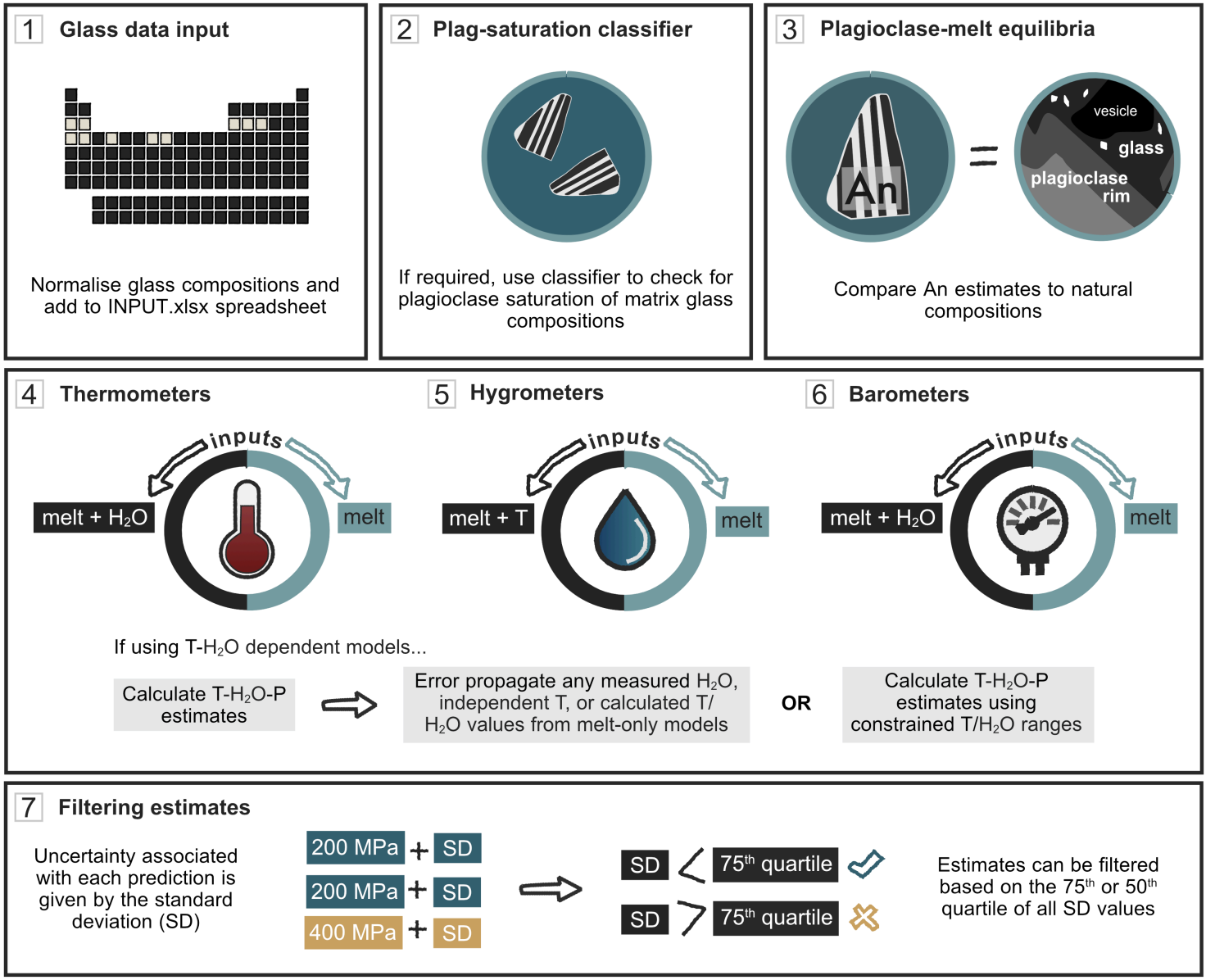

Figure S2.6 Schematic of recommended workflow to use the plagioclase-saturated melt models.

Table S2.2 Summary of cross-validation (CV) and test set RMSE and R^2 values for all models.

Model	T (°C)		H_2O (wt.%)		P (MPa)		An (mol.%)
	Melt + H_2O	Melt-only	Melt + T	Melt-only	Melt + H_2O	Melt-only	Melt-only
CV RMSE	24.5	35.3	0.68	0.97	76.3	91.5	5.8
CV R^2	0.97	0.93	0.94	0.88	0.60	0.41	0.91
Test set RMSE	25.9	37.5	0.69	0.95	76.2	91.3	5.8
Test set R^2	0.96	0.93	0.93	0.88	0.60	0.42	0.90

Table S2.4 Confusion matrix summarising the results of all test set classifications for the plagioclase-saturated melt classifier. 'Yes' refers to melts classified as plagioclase-saturated, and 'No' refers to melts without plagioclase-saturation.

Classification prediction	Classification reference	
	No (i.e. melt is not plagioclase-saturated)	**Yes (i.e. melt is plagioclase-saturated)**
No	188	19
Yes	23	212

3 | Experimental insights into the partitioning behaviour of hydrogen between plagioclase and melt

Abstract

Analysing hydrogen in nominally anhydrous minerals is becoming an increasingly valuable strategy for estimating magmatic water contents. Prior experimental work on plagioclase-melt hydrogen partition coefficients suggests a non-linear relation between H_2O in plagioclase and H_2O in co-existing melt; however, all previous experiments have been limited to mostly lunar mafic starting materials. To expand the applicability of the approach to terrestrial felsic melts, low-pressure, hydrous experiments have been conducted at 780–860 °C in cold-seal pressure vessels using a haplogranitic starting material. Hydrogen concentrations in plagioclase and glass were analysed using Secondary Ion Mass Spectrometry and were supplemented with rhyolitic experimental runs from Madden-Nadeau (2022). The resulting mass fraction (Nernst) partition coefficients, expressed as H_2O_{pl}/H_2O_{melt}, range from 0.002 to 0.008 (± 0.001). Our results indicate that water content in plagioclase depends on water fugacity following a power-law relationship, although constraints on XH_2O or pressure are required to determine melt H_2O concentrations. Hydrogen partition coefficients also have a strong dependence on melt H_2O concentrations ($D_{H_2O}^{plagioclase/melt} = 0.0071 \cdot C_{H_2O}^{melt\,-0.80}$), resulting in strong non-Henrian behaviour likely related to water speciation in the melt. Our empirical hygrometer based on $D_{H_2O}^{plagioclase/melt}$ was applied to hydrated plagioclase grains from dacitic deposits in Castilla et al. (2024), yielding equilibrium melt H_2O contents that corroborate estimates from plagioclase- and quartz-hosted melt inclusions and melt hygrometry.

3.1 Introduction

Water (H_2O) is the most abundant volatile species in silicate melts, exerting a significant impact on the formation and differentiation of melts, as well as resulting eruption styles (e.g., Cashman, 2004; Popa et al., 2021; Rasmussen et al., 2022). Several methods exist to estimate the H_2O content in melts, which include gas and volatile chemistry modelling (Fischer and Marty, 2005); phase equilibria experiments (e.g., Grove et al., 2003; Krawczynski et al., 2012; Melekhova et al., 2017; Ulmer et al., 2018); direct measurements of hydrous glasses (e.g., McIntosh et al., 2022; Murch et al., 2024), typically from melt inclusions (e.g., Muir et al., 2014; Wallace et al., 2021; Urann et al., 2022), and mineral-melt or mineral/melt-only based hygrometers (Waters et al., 2015; Mollo et al., 2015; Perinelli et al., 2016; Cutler et al., 2024; Gavrilenko et al., 2025). While the latter provides a less direct approach to measuring H_2O content, the mineral-based hygrometry method is widely applicable due to its range of available calibrations for different melt compositions and its ease of acquiring the necessary chemical input data. The main limitation of all mineral-based hygrometers is in assessing primary equilibrium and the need for independent temperature and/or pressure estimates. Melt inclusions remain the primary means of directly assessing initial and evolving volatile concentrations across a range of geological settings (e.g., Blundy and Cashman, 2005; Bennett et al., 2019). However, the inclusion record can often be complicated by the availability or size of inclusions, as well as post-entrapment volatile loss through cracks, devitrification, and bubble growth (e.g., Danyushevsky et al., 2002; Moore et al., 2015). With the advancements in measuring hydrogen at finer spatial scales using Secondary Ion Mass Spectrometry (SIMS; e.g., Aubaud et al., 2007; Mosenfelder et al., 2015; Kumamoto et al., 2017), analysing the volatile content of mineral phases (e.g.

pyroxene, olivine) offers an alternative approach to overcoming the limitations of melt inclusions (e.g., Wade et al., 2008; Edmonds et al., 2016; Mitchell et al., 2017). Nominally anhydrous minerals (NAMs) accommodate trace concentrations of hydrogen as structural defects within their crystal lattices, which can act as a proxy for determining melt H_2O content if the relevant mineral-melt partition coefficients are known.

Plagioclase has excellent potential as a NAM hygrometer due to its slower H^+ diffusivity compared to clinopyroxene and olivine (Johnson and Rossman, 2013), meaning that the original H_2O content is preserved during magma ascent, eruption and cooling. Based on infrared (IR) spectroscopic studies, OH^- point defects exist within the plagioclase feldspar lattice with H^+ bonded to oxygen atoms adjacent to M-site (Ca, Na, or K) vacancies (Johnson and Rossman, 2004; Mosenfelder et al., 2020). In silicate melts, water is dissolved as two species: hydroxyl groups (OH) and molecular water (H_2O_m; Stolper, 1982). By measuring the H_2O concentrations in plagioclase, the water content of the host melt can be quantified by:

$$D_{H_2O}^{plagioclase/melt} = \frac{C_H^{plagioclase}}{C_H^{melt}} \quad (1)$$

where $D_{H_2O}^{plagioclase/melt}$ is the partition coefficient, and $C_{H_2O}^{plagioclase}$ and $C_{H_2O}^{melt}$ are the weight concentrations of hydrogen in the respective phases coexisting in equilibrium (e.g., Beattie, 1993). Current experimental constraints on hydrogen plagioclase-melt partitioning are limited to lunar melts (e.g., Caseres et al., 2017; Lin et al., 2019; Xu et al., 2024) and one study on basaltic to basaltic-andesite melts under terrestrial conditions (Hamada et al., 2013). These studies highlight that $D_{H_2O}^{plagioclase/melt}$ varies

with melt H_2O content, indicating a non-linear relationship that does not obey Henry's law. In mineral-melt partitioning studies, Henry's law describes the direct proportionality between the thermodynamic activity of a trace element and its concentration in both the mineral and melt, resulting in partition coefficients independent of the trace element's concentration (Beattie, 1993). The evident non-linearity has led to a mix of hygrometer parameterisations (Hamada et al., 2013; Lin et al., 2019; Xu et al., 2024), though their applicability is limited to mafic melts. In this study, we have carried out H^+ plagioclase-melt partitioning experiments using a haplogranitic starting material to develop a new parameterisation to extend the calibration range to felsic melts.

3.2 Experimental and analytical methods

3.2.1 Starting material

All experiments were performed using a synthetic haplogranite glass (Qz_{31}-Ab_{41}-Or_{22}-An_5, "Glass 0"; Pichavant et al., 2019), prepared from a gel of tetraethyl orthosilicate (TEOS) and various nitrates ($Al(NO_3)_3$; $NaNO_3$; KNO_3 and $Ca(NO_3)_2$) and produced following the co-precipitation method of Hamilton and Henderson (1968). Nitrates were first added to a Teflon beaker with water and ethanol to dissolve and evaporate the contents before incorporating the TEOS. The resulting mixture was precipitated using ammonium hydroxide (NH_4OH) and later dried at ~110°C. The gel was denitrified over a Bunsen burner and ground in a pestle and mortar. The gel was then melted twice in a Pt crucible at 1400 °C for 4-5 hr in a 1 atm furnace, with grinding occurring between each melting cycle to ensure the final glass was homogenous (Table 3.1).

Equilibrium conditions are easier to reach in silicic systems when using an amorphous starting material, but crystals formed at high temperatures are usually too small for geochemical analysis. Therefore, to enhance the size of crystallised plagioclase, two types of starting materials were tested: a dry haplogranitic powder (grain size ~<250 μm) with water and pre-hydrated haplogranitic glass chips. The former material undergoes hydration and crystallisation during the same run, whereas the latter only experiences crystallisation. The first type of charge consisted of ~110 mg of haplogranitic glass powder doped with ~2-3 mg of natural gem-quality plagioclase seeds (250–500 μm in size, An_{10-59}; Table 3.2), and varying amounts of deionised water (Table 3.3) to ensure water saturation (i.e., Newman and Lowenstern, 2002). The exact same process was followed for the hydrated glass chips except for the supplement of plagioclase seeds. The hydrated glass chips were then transferred to a new capsule with the addition of ~2-3 mg plagioclase seeds. All partitioning experiments were conducted in hydrothermal, cold-seal pressure vessels (CPSVs) at the University of Oxford. Charges were loaded into $Au_{80}Pd_{20}$ (3 mm diameter, 0.25 mm wall thickness) or Au_{100} capsules (3.9 mm diameter, 0.20 mm wall thickness) to minimise H^+ diffusion and arc-welded shut. Capsules were placed at one end of a Rene 41 Ni-alloy autoclave and were buffered at nickel-nickel-oxide (NNO) using pure Ni filler rods positioned next to the capsule (Matthews et al., 2003). A K-type thermocouple inserted into the end of the autoclave close to the capsule was used to check the temperature offset between the furnace's internal thermocouple and the autoclave (Cassidy et al., 2022; Voigt et al., 2022). Experiments were conducted at 780–860 °C at pressures ≤200 MPa for durations

Table 3.1 Experimental starting materials for hydrogen partitioning runs and hydrous haplogranitic standards for SIMS.

Sample	**Glass_0**		**LW**		**HW**	
n (EPMA)	18	σ1	9	σ1	10	σ1
SiO_2	75.90	0.20	76.00	1.15	76.01	0.31
TiO_2	0.00	0.02	0.00	0.01	0.00	0.01
Al_2O_3	14.90	0.25	14.48	0.64	14.69	0.14
FeO_t	0.22	0.02	0.36	0.05	0.34	0.04
MnO	0.01	0.02	0.02	0.03	0.00	0.04
MgO	0.00	0.02	0.01	0.02	0.01	0.02
CaO	1.06	0.02	0.89	0.36	1.01	0.04
Na_2O	4.14	0.31	4.52	0.48	4.33	0.40
K_2O	3.76	0.07	3.67	0.19	3.56	0.26
Total (raw)	98.87		96.93		94.27	
FTIR H_2O (wt.%)	NA		1.97		3.20	

Normalised to 100% anhydrous.

between 192 and 288 hr. Experiments were then quenched using a rapid water-cooled system. Recovered capsules were weighed before and after welding and following quenching to ensure no water loss; experiments recording a mass loss were discarded. Capsule tops were cut, and the remaining capsule material was peeled back using pliers to extract the experimental glass for multiple geochemical analyses. Rhyolitic phase-equilibrium experiments simulating magma storage conditions of the 1883 Krakatau eruption from Madden-Nadeau (2022) were also selected to supplement our hydrogen plagioclase-melt analyses, as neither the glass nor the plagioclase had previously undergone water analysis by SIMS.

Table 3.2 Compositions of experimental plagioclase seeds and plagioclase SIMS standards.

Sample	**O_US^**		**An_M^**		**L_Co*^**	
Locality	New Mexico, US		Inner Mongolia		Congo	
n (EPMA)	40	σ1	50	σ1	39	σ1
SiO_2	63.04	0.22	56.79	0.18	52.64	0.23
TiO_2	0.00	0.01	0.06	0.02	0.07	0.02
Al_2O_3	22.83	0.09	27.00	0.15	29.56	0.14
FeO_t	0.07	0.02	0.36	0.03	0.36	0.02
MnO	0.00	0.01	0.01	0.02	0.00	0.01
MgO	0.00	0.01	0.07	0.01	0.10	0.01
CaO	4.00	0.02	9.58	0.03	12.44	0.04
Na_2O	9.47	0.09	5.54	0.10	4.48	0.05
K_2O	0.24	0.01	0.49	0.02	0.29	0.01
Total	99.68		99.91		99.95	
An	18.5		47.2		59.2	
Ab	80.2		50.0		39.1	
Or	1.3		2.9		1.6	
FTIR H_2O (ppm)	43.7	1.5	**0.7	2.0	98.2	6.1

*Experimental seed composition

^SIMS standards

**FTIR H_2O contents from Mosenfelder et al. (2015) for GRR 3031.

Table 3.3 Experimental run conditions, run products, and SIMS data of glass and plagioclase.

Run no.	Conditions			Phase assemblage & proportions^ (%)	$\sum R^2$	H_2O* (wt.%)	Glass			Plagioclase			H^+ partition coefficient	
	T (°C)	P (MPa)	Duration (hr)				H_2O (wt.%)	n	σ1	H_2O (ppm)	n	σ1	D	σ1
HL_CoGL08	830	68	240	gl (97.3), pl (2.3)	0.15	3.15	2.80	3	0.1	172	5	4.8	0.006	0.001
HGL19	790	168	192	gl (91.0), pl (9.0)	0.06	5.15	2.20	2	0.1					
HGL22	780	72	240	gl (95.2), pl (4.8)	0.21	3.40	2.01	4	0.1	156	2	15.4	0.008	0.001
HGL23	860	54	288	gl (86.4), pl (13.6)	0.04	2.70	1.83	3	0.03					
HGL24	800	78	288	gl (93.3), pl (6.7)	0.25	3.50	2.09	3	0.04					
KK16	850	150	168	gl (91.6), pl (6.0), cpx (0.5), opx (1.6), acc (0.3)		4.94	5.27	3	0.1	86	5	3.2	0.002	0.0001
KK27	800	200	168	gl (85.3), pl (11.3), cpx (2.3), qtz (1.3), acc (1.1)		6.08	5.07	2	0.02	82	3	32.0	0.002	0.001

^Mass balance calculated using GeoBalance (Li et al., 2020) without considering the seeds. KK16 and KK27 proportions from Madden-Nadeau (2022) calculated from SEM BSE imagery (gl, glass; pl, plagioclase; cpx, clinopyroxene; opx, orthopyroxene; qtz, quartz; acc, accessory minerals such as Fe-Ti oxides and apatite).
*Water added to capsule.

3.2.2 Secondary Ion Mass Spectrometry (SIMS)

Chips of experimental run products were ground individually using alumina grinding papers and diamond paste to a 1 μm polish and pressed, polished side up, into indium-filled aluminium rounds. Backscatter Electron (BSE) maps were created for all mounts, with images taken to scope for plagioclase targets using the FEI Quanta 650 Scanning Electron Microscope at the Department of Earth Sciences, University of Oxford. The samples were uncoated for mapping, carried out in low vacuum mode using a ~5 nA beam current and a 20 kV accelerating voltage.

The mounts were Au-coated and analysed using the Cameca IMS-7f instrument at the Edinburgh Ion Microprobe Facility (EIMF; University of Edinburgh, Apr 2024). We implemented several approaches to minimise hydrogen background signals: (1) samples were held under high vacuum conditions for at least 48 hr before analysis; (2) only the last five cycles of each analysis were used to integrate the hydrogen signal; and (3) analyses were performed using a 15 keV $^{16}O^-$ primary beam and a positive secondary ion beam with a liquid N_2 cold trap attached. Alongside $^1H^+$, the isotopes ^7Li, ^{30}Si and ^{26}Mg were also measured. ^{30}Si was used to ratio the ^1H signal and ^{26}Mg to cross-check against electron microprobe (EPMA) analyses of the same phase.

Glass $^1H^+$ concentrations were measured using a 3 nA primary beam, with 90 seconds pre-sputter raster over a 10 μm^2 area to remove any absorbed H_2O from the sample surfaces. Plagioclase $^1H^+$ concentrations were measured using a 3 nA primary beam, with 240 seconds pre-sputter rastered over a 15 μm^2 area. H_2O concentrations in the glass and plagioclase were calculated based on the $^1H^+/^{30}Si^+$ ion ratio and calibrated using working curves constructed from standards with known volatile contents (c.f. Blundy and Cashman 2008). H_2O concentrations were

calibrated using a selection of glass (LW; HW; Lipari RF obsidian, Humphreys et al., 2008; Suprasil blank), plagioclase (A_M; O_US; L_Co) and NAM secondary standards (Supplementary Table 3.1; Langmuir et al., 1977; Luhr and Aranda-Gomez, 1997; Harvey et al., 2012; Kumamoto et al., 2017). It should be noted that matrix-matched standards were not used to calibrate plagioclase water values because the plagioclase standards (A_M, O_US) are not well characterised, which means the measured values may be influenced by matrix effects (e.g., Hauri et al., 2002). The calibration was fitted using a weighted least squares regression to account for heteroscedasticity (Figure 3.1), with weighting based on the uncertainty in the FTIR values for water content. $^{1}H^{+}$ backgrounds were monitored using the A_M standard, as the Suprasil blank recorded a greater OH^{-}/Si^{-} signal than expected. A_M is an andesine (An_{47}) sourced from the same locality as crystals reported in Mosenfelder et al. (2015; GRR2651) and Johnson and Rossman (2004), characterised by a low H_2O content of 0.7 ppm (Mosenfelder et al., 2015). Therefore, for the instrument background, we used the levels determined on the A_M standard, resulting in a background of 3.5 ppm, and subtracted the average $^{1}H^{+}$ background count from all analyses. The minimum detection limit (calculated from three standard deviations on repeat background measurements) of H_2O was 3.2 ppm.

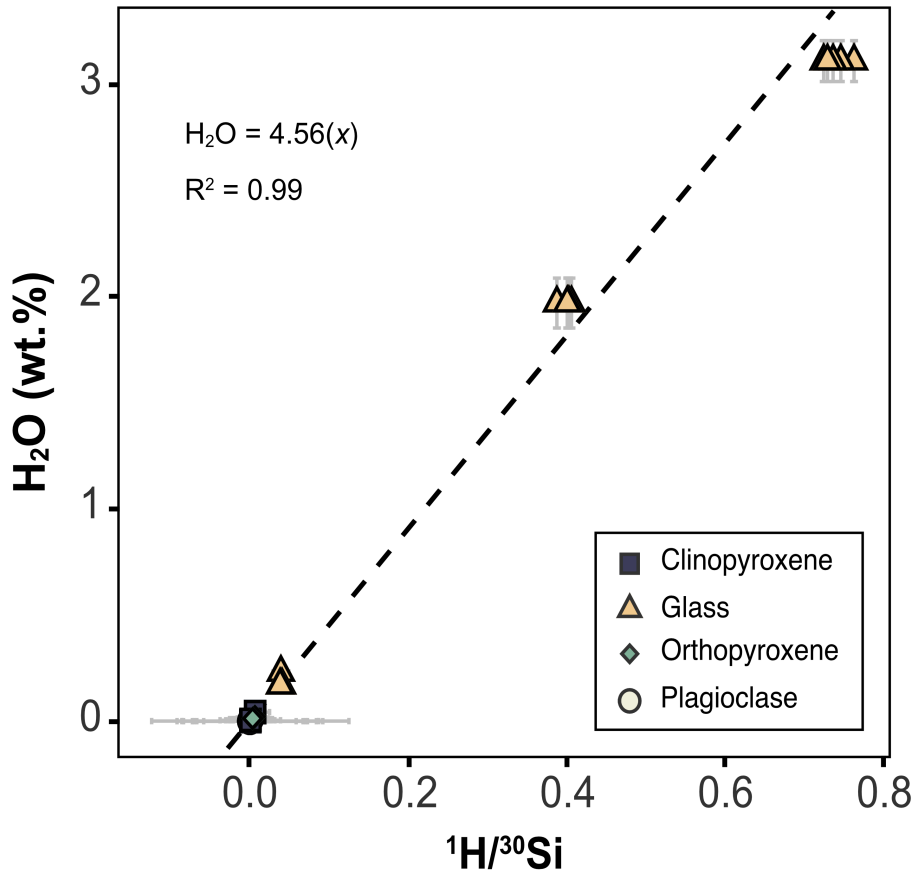

Figure 3.1 Calibration curve for the April 2024 SIMS session.

3.2.3 Fourier Transform Infrared Spectroscopy

The LW and HW standards were prepared as double-sided polished wafers, with a 0.34 and 190 μm thickness, respectively, measured using a Mitutoyo digital micrometre (±1 μm accuracy). Both standards were formed under water-saturated conditions in CSPVs using the same dry haplogranitic starting material used for the partitioning experiments (Table 3.1). H_2O concentrations were analysed using the ThermoFisher Scientific Nicolet iN 10 Fourier Transform Infrared Spectrometer at the University of Bristol. Unpolarised glass spectra (700 to 7000 cm^{-1} wavelengths) were taken with a resolution of 8 cm^{-1}, collected from 256 scans with an aperture size of 100x100 μm. The near-IR absorption bands at 5200 cm^{-1} (H_2O_m) and 4500 cm^{-1}

(OH^-) were used to obtain peak heights, and 4–5 analyses across each glass wafer were taken to account for thickness variation.

The O_US and L_Co plagioclase standards (Table 3.2) are two gem-quality oligoclase (An_{19}) and labradorite (An_{59}) crystals, respectively, polished into ~200–400 µm thick wafers. Water concentrations in anisotropic plagioclase crystals are typically determined using polarised infrared light and acquiring absorption spectra along three principal crystallographic axes. However, the crystal axes could not be identified at the time. Instead, unpolarised spectra were taken on randomly oriented crystals (Kovács et al., 2008; Sambridge et al., 2008) with a resolution of 4 cm^{-1} and collected from 128 scans with an aperture size of 150x150 µm. Mid-IR absorption bands between 3200 and 3700 cm^{-1} were used to obtain band areas, signifying the structurally-bound type IIa OH band characterising plagioclase (Johnson and Rossman, 2004), and corrected using a spline-fit baseline correction (Mosenfelder et al., 2015; Xu et al., 2024).

H_2O concentrations for the glass and plagioclase were calculated using the Beer-Lambert law:

$$C = \frac{1.802 \cdot A}{\rho \cdot t \cdot \varepsilon} \quad (2)$$

where C is the water concentration (wt.%) of the glass, A is the peak height of the species absorption peak (cm^{-1}) for glass or the integral area under the O-H absorption band for plagioclase, p is the density (2.30 g cm^{-3} for haplogranitic glass, Ardia et al., 2014; 2.76 g cm^{-3} for plagioclase, Hacker et al., 2003), t is the thickness of the sample (cm), and ε represents the molar absorptivity. Molar absorption coefficients used are εOH = 1.56 l mol^{-1} cm^{-1} and εH_2O = 1.79 l mol^{-1} cm^{-1} (Behrens

and Nowak, 2003) for the haplogranitic glass and an updated molar absorption coefficient of 202,600 l mol^{-1} cm^{-2} (Mosenfelder et al., 2015) for plagioclase.

3.2.4 Electron Probe Microanalysis

The haplogranitic experiments, along with glass from the Krakatau sample KK16 (Madden-Nadeau, 2022), were analysed using a Cameca SX-5 FE electron microprobe at the Department of Earth Sciences, University of Oxford. Plagioclase crystals were analysed using an acceleration voltage of 15 kV, a beam current of 15 nA, and a focused beam (spot size of 1 μm). Glasses were analysed at 15 kV acceleration voltage, a beam current of 4 nA, and a defocused 10x10 μm beam size to minimise alkali migration under the electron beam. Alkalis were also analysed first with short counting times to reduce migration (e.g., Humphreys et al., 2006). Secondary standards include SJI olivine and labradorite.

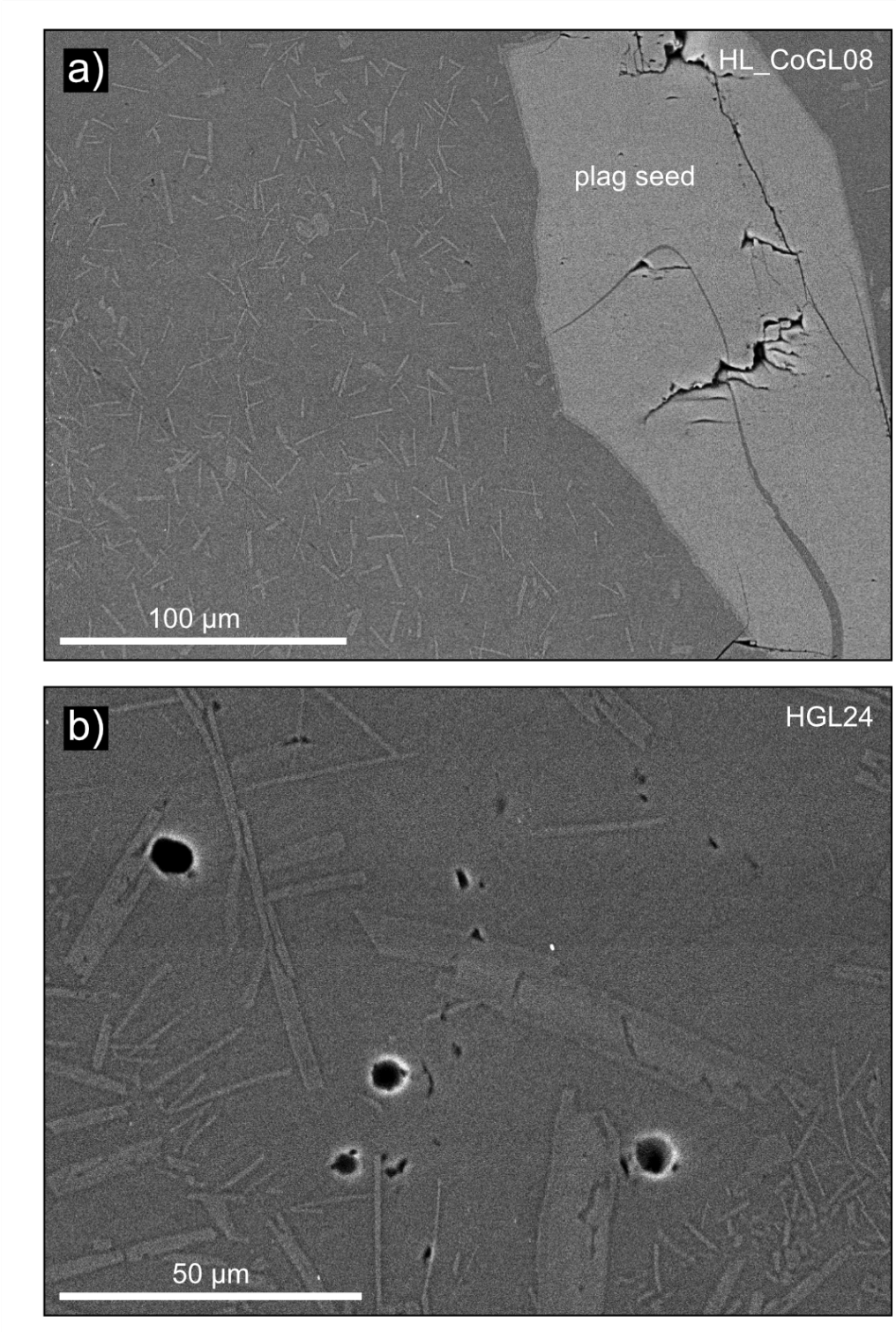

Figure 3.2 SEM images of experimental runs. (**a**) HL_CoGL08 is a charge with dry glass powder + water and plagioclase seeds, whereas HGL24 (**b**) is an example of a charge with pre-hydrated glass.

3.3 Results

3.3.1 Experimental phases and major element compositions

All experiments contain plagioclase and glass; additionally, pyroxenes and accessory phases such as apatite and Fe-Ti oxides occur in the two Krakatau runs (KK16 and KK27). Tables 3.4 and 3.5 list the average major element compositions and corresponding standard deviations of the plagioclase and glass. Plagioclase crystals are usually euhedral, evenly distributed throughout the capsules, and unzoned in most experiments, except for pre-hydrated starting material. The pre-hydrated chip and dry glass powder charges have similar plagioclase compositions (An_{21-26}), yet the crystals display different textures (Figure 3.2). The pre-hydrated charges are more anhedral and skeletal than the dry powder charges, which are more euhedral in shape. This difference in shape may represent a change from interface-controlled growth dominating the dry powder charges to diffusion-controlled growth in the pre-hydrated charges (Da Silva et al., 2017). However, the pre-hydrated charges exhibit larger crystal widths (~15–30 μm) than the dry glass powder charges with widths of <5 μm. As such, the seeds were the main analytical targets for the dry powder charges, where H_2O enrichment occurs via diffusion rather than growth.

3.3.2 H_2O contents of experimental glass and plagioclase

Rim analyses of plagioclase crystals could not be obtained, as the average width of the rims is <2 μm, which would result in analyses contaminated by high glass concentrations. Additionally, analysing the small-grown crystals proved challenging for experiments HGL19, HGL23, and HGL24, where seeds were unavailable in the polished sections. The plagioclase analyses in these experiments exhibited very

Table 3.4 EPMA of glasses.

Sample	HA_KGL02		HL_CoGL08		HGL19		HGL22		HGL23		HGL24		KK16		KK27*	
n (EPMA)	1	σ1	10	σ1	9	σ1	10	σ1	9	σ1	10	σ1	9	σ1	11	σ1
SiO_2	76.70		76.37	1.00	77.15	1.67	76.20	1.47	77.73	1.61	76.68	0.73	71.80	0.52	75.62	0.16
TiO_2	0.00		0.00	0.01	0.00	0.01	0.00	0.02	0.00	0.01	0.00	0.01	0.48	0.04	0.27	0.03
Al_2O3	13.86		14.46	0.53	13.71	1.35	14.31	1.24	13.50	0.99	14.08	0.47	15.42	0.23	14.51	0.15
FeO_t	0.36		0.29	0.06	0.15	0.04	0.15	0.07	0.14	0.05	0.15	0.06	1.63	0.14	1.16	0.06
MnO	0.02		0.00	0.05	0.00	0.02	0.00	0.04	0.00	0.02	0.00	0.03	0.07	0.02	0.03	0.02
MgO	0.01		0.01	0.02	0.00	0.02	0.00	0.01	0.00	0.03	0.01	0.02	0.57	0.30	0.18	0.03
CaO	0.83		0.99	0.26	0.57	0.45	0.65	0.42	0.45	0.41	0.57	0.29	1.63	0.25	0.98	0.04
Na_2O	4.31		4.30	0.45	4.14	0.67	4.42	0.58	3.99	0.60	4.15	0.53	6.45	0.50	5.06	0.14
K_2O	3.92		3.51	0.19	4.22	0.75	4.23	0.74	4.14	0.46	4.32	0.59	1.93	0.24	2.18	0.04
Total (raw)	92.51		95.77		96.90		95.97		96.78		96.32		93.12		91.80	

Normalised to 100% anhydrous.
*Data from Madden-Nadeau (2022).

Table 3.5 EPMA of crystallised plagioclase.

Sample	HL_CoGL08		HGL19		HGL22		HGL23		HGL24		KK16*		KK27*	
n (EPMA)	6	σ1	7	σ1	10	σ1	11	σ1	10	σ1	18	σ1	13	σ1
SiO_2	63.85	1.09	61.99	1.23	64.45	1.55	64.67	1.86	62.48	1.02	55.74	1.00	55.04	1.85
TiO_2	0.00	0.01	0.00	0.00	0.00	0.01	0.00	0.01	0.00	0.01	0.04	0.02	0.04	0.01
Al_2O_3	22.33	0.89	23.86	1.09	21.93	1.08	21.93	1.25	23.91	0.74	27.44	0.69	27.46	1.25
FeO_t	0.09	0.04	0.03	0.02	0.12	0.03	0.12	0.03	0.03	0.02	0.56	0.20	0.53	0.05
MnO	0.00	0.02	0.00	0.01	0.00	0.01	0.00	0.01	0.00	0.01	0.01	0.01	0.01	0.01
MgO	0.00	0.01	0.00	0.01	0.00	0.01	0.00	0.01	0.00	0.01	0.04	0.01	0.04	0.01
CaO	4.10	0.53	4.97	0.69	4.19	0.55	4.13	0.71	4.99	0.56	10.18	0.68	10.62	1.46
Na_2O	8.26	0.47	8.31	0.38	7.86	0.45	7.72	0.52	7.69	0.42	5.80	0.43	6.09	0.87
K_2O	1.35	0.32	0.82	0.35	1.43	0.31	1.40	0.43	0.87	0.26	0.19	0.03	0.18	0.04
Total	100.51		100.79		99.69		101.09		101.15		99.44		98.48	
An	20		24		21		21		25		49		49	
Ab	72		72		71		71		70		50		50	
Or	8		5		9		9		5		1		1	

*Data from Madden-Nadeau (2022).

high H^+ concentrations, indicating glass-contaminated analyses, and are not considered further. This is further supported by the high lithium counts in plagioclase, which resemble those in the glass.

For the haplogranite experiments, the plagioclase in the seed (HL_CoGL08) and grown crystals (HGL22) contain H_2O contents of 156 and 172 ppm, respectively, while the Krakatau plagioclase (KK16 and KK27) have H_2O contents of 82 and 86 ppm, respectively. The melt H_2O contents in all experiments range between 2.01 and 5.27 wt.%. The corresponding average $D_{H_2O}^{plag/melt}$ value for experiments with high H_2O contents (>4.0 wt.%) is 0.002, which is consistent with terrestrial experiments conducted on basaltic to basaltic-andesite melts (Hamada et al., 2013) and plagioclase-melt inclusion analyses from dacitic-rhyolitic systems (Figure 3.3; Caseres, 2019; Rappoccio et al. 2020). In contrast, the lower H_2O content experiments have higher partition coefficients of 0.006–0.008.

3.4 Discussion

3.4.1 Controls on hydrogen plagioclase-melt partitioning

Compiling partitioning data from previous experiments and natural samples reveals that the primary factors controlling hydrogen partitioning between plagioclase and melt are the H_2O content of the melts and the oxygen fugacity. This section will explore the importance of these factors.

Prior work has shown that $D_{H_2O}^{plag/melt}$ correlates inversely with oxygen fugacity, particularly at reduced conditions (Caseres et al., 2017; Lin et al., 2019). As shown in Figure 3.4, higher partition coefficients are observed as fO_2 decreases from the NNO (nickel-nickel oxide) to IW (iron-wüstite) buffer, which mirrors H^+ solubility data in

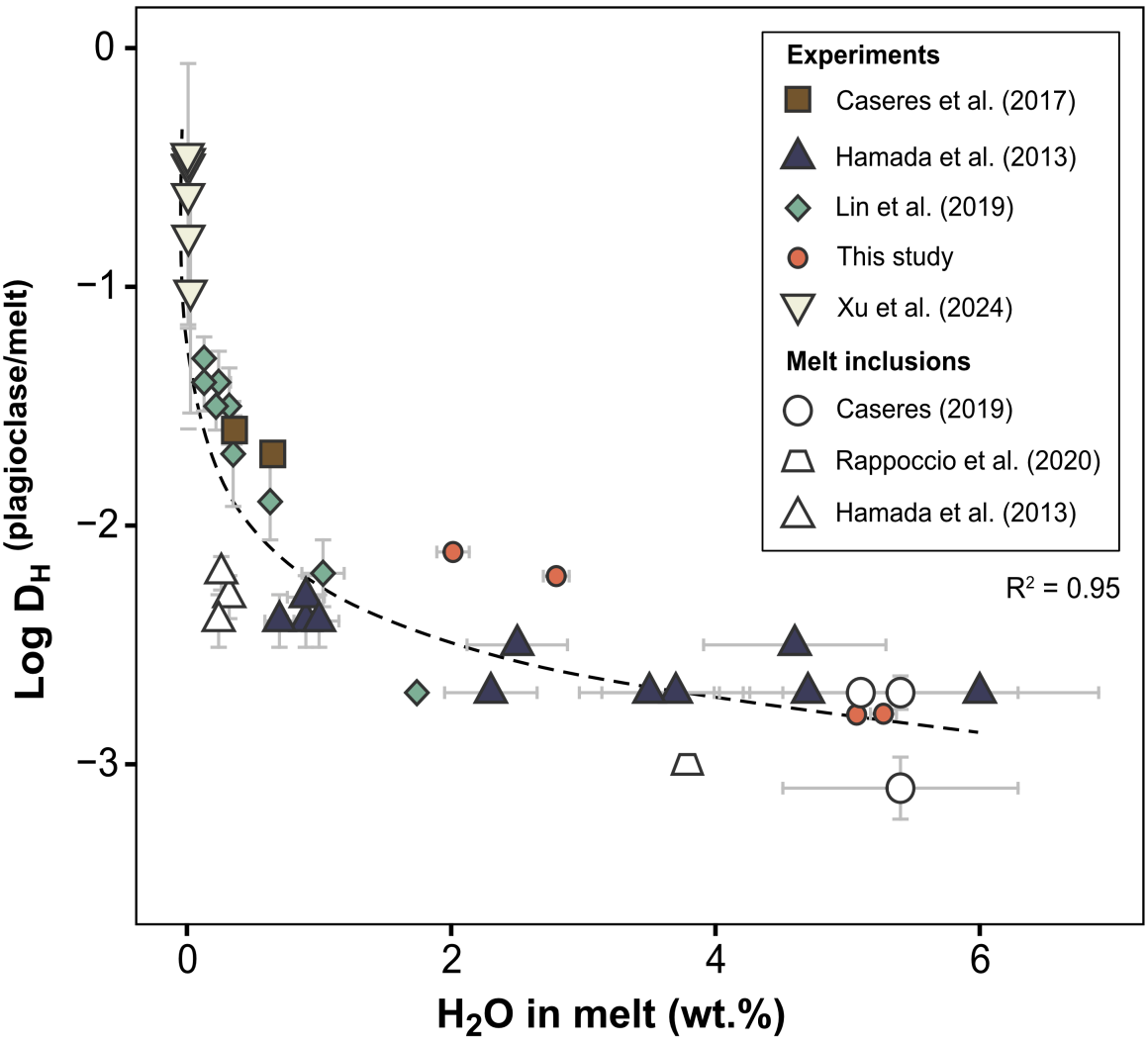

Figure 3.3 Hydrogen partition coefficients obtained from experiments and plagioclase-melt inclusion pairs versus melt water content (wt.%). Note that hydrogen partition coefficients from Hamada et al. (2013) are recalculated using the updated FTIR plagioclase absorption coefficient by Mosenfelder et al. (2015). The displayed line of best fit was derived solely from the experimental data.

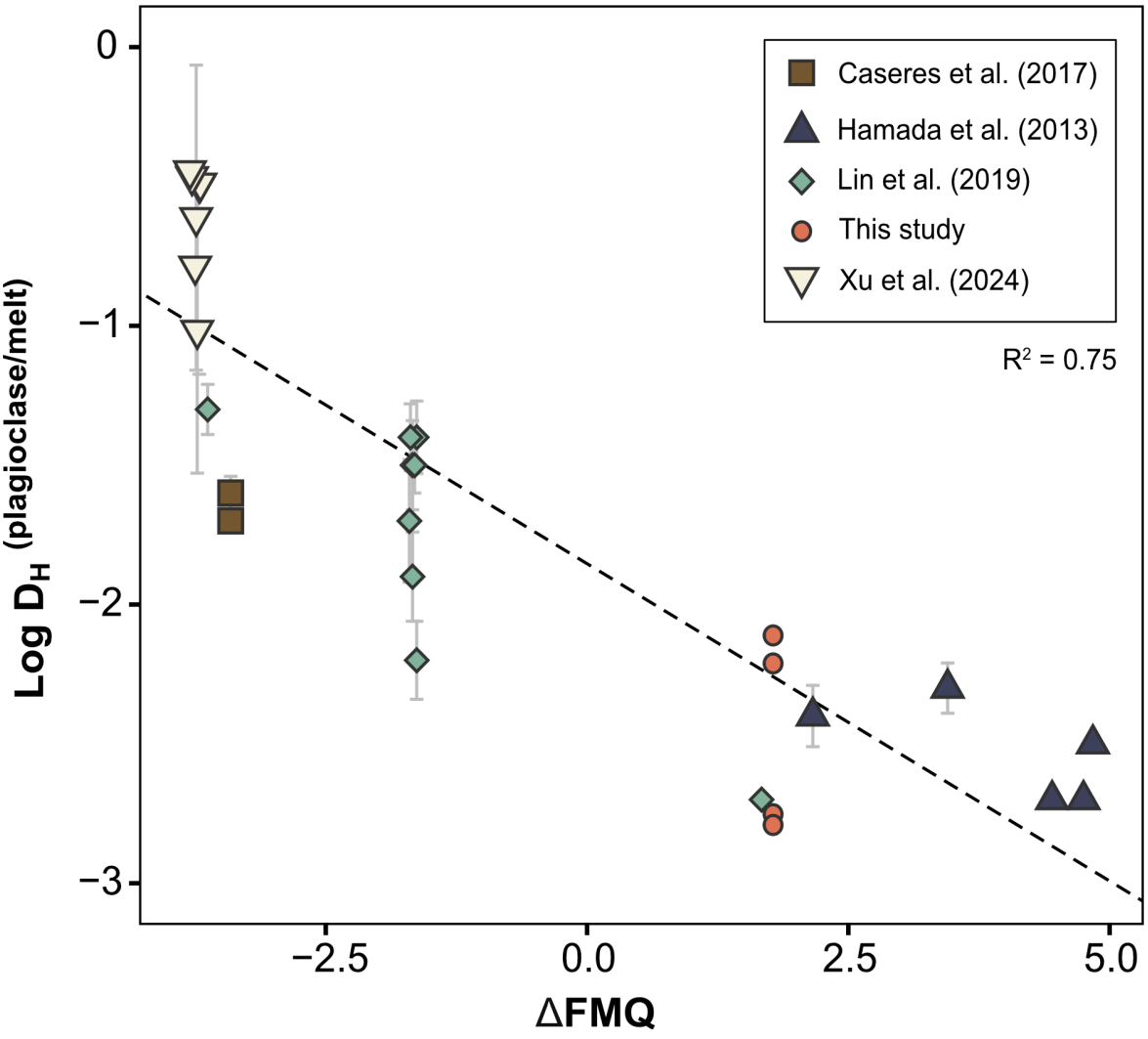

Figure 3.4 Hydrogen partition coefficients versus fO_2. fO_2 values recalculated to the fayalite-magnetite-quartz (FMQ) buffer using Kress and Carmichael (1991).

plagioclase ranging between An_{58} and An_{94} (Yang, 2012; Mosenfelder et al., 2020). Mosenfelder et al. (2020) proposed that the main H^+ incorporation mechanism in plagioclase occurs when Fe^{3+} in tetrahedral sites reduces to Fe^{2+}, and hydrogen attaches to an adjacent M-site vacancy to attain charge balance. However, Mosenfelder et al. (2020) noted an increase in H^+ solubility in more oxidising environments between the NNO and haematite-magnetite (HM) buffers, indicating a possible change and further complexity with H^+ incorporation into the plagioclase structure. Despite the apparent correlation in Figure 3.4, there are examples of wide-ranging $D_{H_2O}^{plag/melt}$ values, at constant fO_2 (e.g., Lin et al., 2019; this study). This variability appears to stem from variations in melt water content, highlighting how fO_2 has a minor effect on partitioning compared to melt H_2O content.

Experimental studies have observed non-Henrian behaviour between H_2O concentrations measured in plagioclase crystals and H_2O in co-existing melts, evident in the curvature of H_2O in plagioclase versus H_2O in the melt in Figure 3.5 (Hamada et al., 2013; Lin et al., 2019; Xu et al., 2024). To account for this, existing parameterisations of H^+ partitioning between plagioclase and silicate melts have fitted the data to develop two separate constant partition coefficients for low- and high-water melts (Hamada et al., 2013; Lin et al., 2019). Other studies have calculated a constant partition coefficient of ~0.002 based on analyses of plagioclase-melt inclusion pairs from dacitic-rhyolitic systems such as Mount St Helens (Johnson, 2005), Mount Hood (Caseres, 2019) and the Huckleberry Ridge Tuff, Yellowstone (Rappoccio et al., 2020). Hydrogen is primarily present as hydroxyl groups and molecular water in silicate melts (Stolper, 1982; Dixon et al., 1995) and predominantly as hydroxyl groups in a range of nominally anhydrous minerals

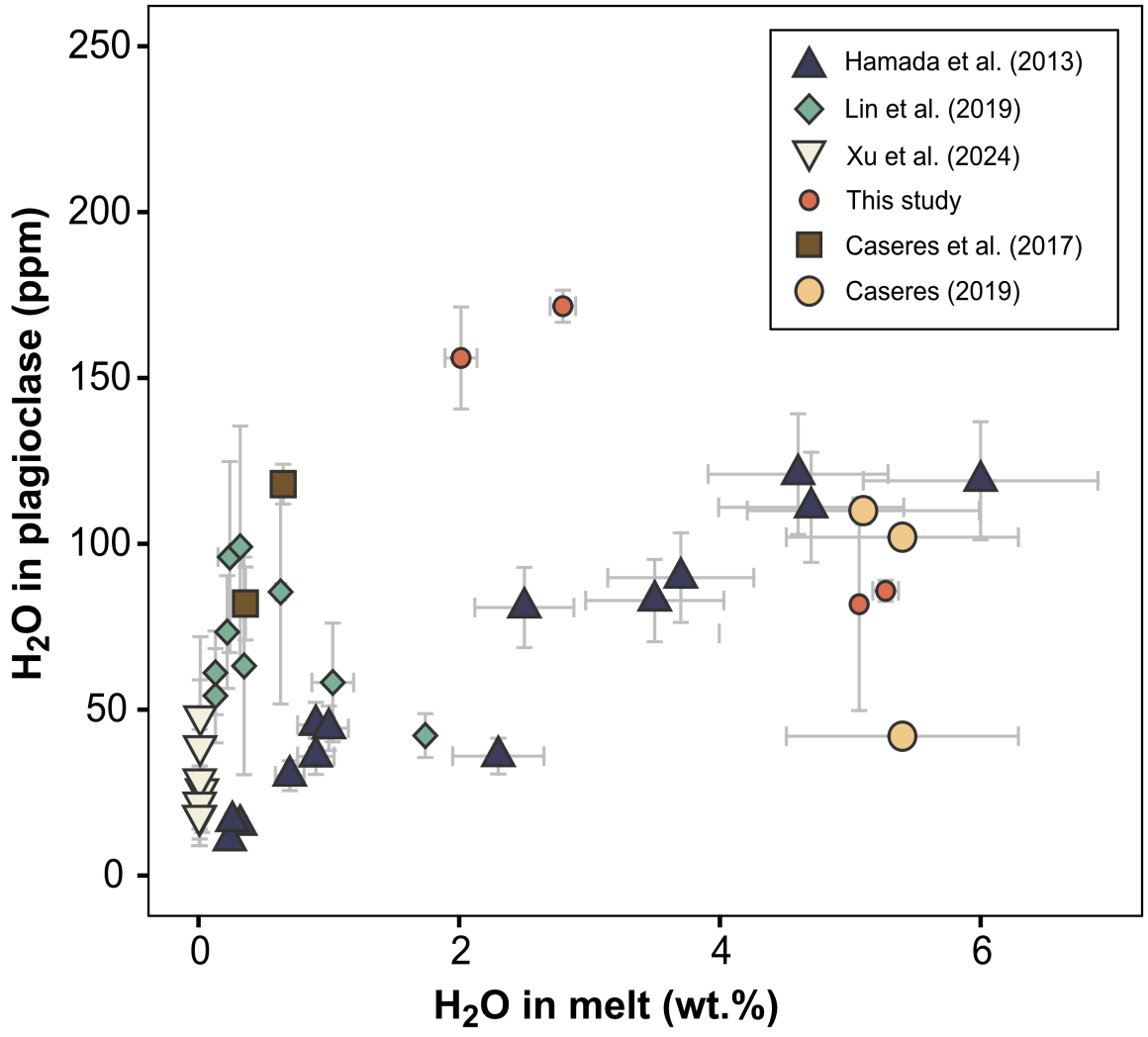

Figure 3.5 H_2O contents in hydrated plagioclase crystals (weight ppm of H_2O) and co-existing melt (wt.%).

(Keppler and Bolfan-Casanova, 2006), including plagioclase (e.g., Johnson and Rossman, 2004; Mosenfelder et al., 2015). The complex hydrogen speciation in melts and minerals indicates that partitioning is unlikely to be independent of water concentration (e.g., clinopyroxene; Adam et al., 2016), particularly since the activities of OH/H_2O in silicate melts vary non-linearly as a function of total water concentration (Stolper, 1982). To account for water speciation, Castilla et al. (2024) fitted the H_2O concentration in plagioclase as a square root function of melt H_2O content using the terrestrial experiments and plagioclase-melt inclusion data of Hamada et al. (2013) and Caseres (2019). Their parameterisation is based on the expectation that the mole fraction of hydroxyl in both plagioclase ($X_{OH}^{plagioclase}$) and the melt (X_{OH}^{melt}) is proportional to the square root of water fugacity (fH_2O):

$$C_{H_2O}^{plagioclase} = 48\sqrt{C_{H_2O}^{melt}} \quad (3)$$

However, Castilla et al. (2024) note their parameterisation only applies in low-pressure settings and is unlikely to extrapolate to cases of higher fH_2O, as the relationship of $X_{OH}^{melt} \propto \sqrt{fH_2O}$ will no longer hold (Newcombe et al., 2017). The reactions describing the dissolution of water in the melt ($H_2O^{fluid} = H_2O_m^{melt}$, $H_2O_m^{melt} + O^{melt} = 2OH^{melt}$; Stolper, 1982) can be combined to form an equilibrium constant (K_1) that can be approximated as:

$$K_1 \cong \frac{X_{OH}^{melt^2}}{X_O^{melt} \cdot fH_2O} \quad (4)$$

At low water concentrations, H_2O mainly dissolves as hydroxyl groups in the melt, leading to minimal water dissolution with negligible change to X_O^{melt} such that it can be assumed constant. However, this assumption is no longer valid at higher fH_2O, and a pressure dependence may further affect the equilibrium constant (Newcombe et al., 2017; Castilla et al., 2024). This is evident when all H^+ partitioning experiments are considered, as nearly all the lunar experiments deviate from the trend (Figure 3.5), especially the high-pressure (>400 MPa) experiments of Lin et al. (2019) and Caseres et al. (2017). Given that water solubility in silicate melts and plagioclase is known to be dependent on pressure (e.g., Hamilton et al., 1964; Dixon et al., 1995; Liu et al., 2005; Shishkina et al., 2014), we explored an alternative fit using plagioclase H_2O concentrations from partitioning studies alongside solubility experiments (Yang, 2012; Behrens, 2021) correlated with water fugacity (fH_2O). pH_2O (MPa) in all partitioning experiments was calculated assuming that pH_2O = $P_{total} \cdot XH_2O_{(fluid)}$, with the latter parameter calculated using MagmaSat (Ghiorso and Gualda, 2015). Water fugacity was then calculated using an online calculator (https://fluid-eos.web.psi.ch/EOS/calculator_simple.html). From this, we obtain the following best-fit equation (R^2 = 0.74; ± 0.38; Figure 3.6) using a weighted power law regression:

$$C_{H_2O}^{plagioclase} = 51.26 \cdot fH_2O^{0.20} \quad (5)$$

where $C_{H_2O}^{plagioclase}$ is the measured water concentration of plagioclase (ppm). However, the melt water concentration can only be recovered from water fugacity if an independent constraint on XH_2O or pressure is available. As an alternative empirical calculation that is not dependent on other variables, we performed another

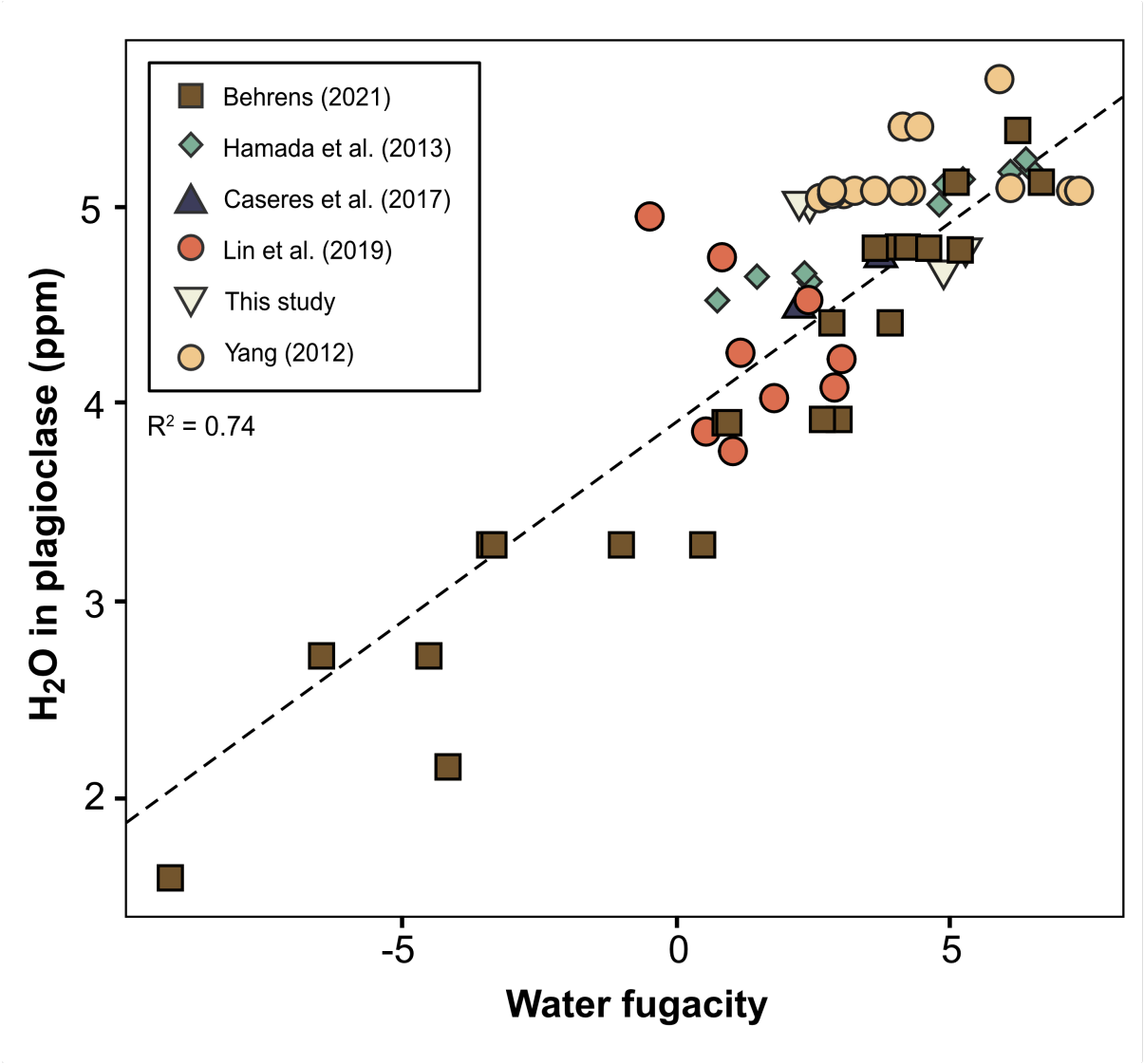

Figure 3.6 Power-law regression of water fugacity versus H_2O in plagioclase (ppm). Plagioclase H_2O values were taken from both partitioning and solubility experiments.

weighted regression to determine a power law relation between $D_{H_2O}^{plag/melt}$ and melt water content (R^2 = 0.95; ± 0.4):

$$D_{H_2O}^{plagioclase/melt} = 0.0071 \cdot {C_{H_2O}^{melt}}^{-0.80} \quad (6)$$

Rearranging Equation 6 produces a new H^+-in-plagioclase hygrometer (Equation 7):

$$C_{H_2O}^{melt} = \left(\frac{C_{H_2O}^{plagioclase}}{0.0071}\right)^5 \quad (7)$$

where $C_{H_2O}^{melt}$ and $C_{H_2O}^{plagioclase}$ are water concentrations of melt and plagioclase in wt.%, respectively. The high sensitivity of Equation 7 is a substantial limitation for using H^+-in-plagioclase as a hygrometer and highlights the importance of obtaining high-quality data on H^+ concentrations with SIMS or FTIR. Measuring water content in nominally anhydrous minerals (NAMs) using SIMS offers greater precision than FTIR, with typical analytical uncertainties of 5-10% (e.g., Koga et al., 2003). FTIR uncertainties can be minimised by analysing plagioclase crystals under polarised infrared light and by carefully selecting appropriate absorption coefficients (Mosenfelder et al., 2015). Meanwhile, SIMS uncertainties can be reduced by using matrix-matched standards, though such standards are currently limited for plagioclase. Regardless of the instrument used, even small changes in plagioclase H+ concentrations can greatly affect the calculated equilibrium melt content. For instance, with a measured plagioclase H_2O value of 93 ppm and an uncertainty of ±10%, the actual melt H_2O content could range from 2.3 to 6.2 wt.%. Despite its high sensitivity, the main advantage of this hygrometer is that it provides an alternative,

direct method for determining H_2O concentrations when no viable melt inclusions are available. To optimise the approach, using large crystals from highly explosive eruptions characterised by rapid decompression and quickly cooled volcanic deposits will favour better preservation of water in plagioclase (Lloyd et al., 2016). Until further experiments are conducted to refine parameterisations and well-characterised plagioclase standards are developed for SIMS analysis, using plagioclase as a nominally anhydrous mineral hygrometer remains a tentative approach. However, clinopyroxene can currently offer more reliable water constraints due to its well-established partitioning coefficients (e.g., O'Leary et al., 2010) and accessible standards (Kunamoto et al., 2017).

3.4.2 Magmatic water contents estimated from Cerro Machín (Colombia) plagioclase

Detailed tephra stratigraphy and radiocarbon dating reveal that six Plinian eruptions occurred at Cerro Machín volcano, Colombia, during the Holocene. The third eruption, dated to 3600 years BP, is identified as the largest Plinian event (VEI = 5; Rueda, 2005); the dacitic pyroclastic fall deposits contain plagioclase, amphibole, quartz, and biotite, along with minor phases of Fe-Ti oxide, olivine, and apatite within a rhyolitic matrix (Castilla et al., 2024). The new H^+-in-plagioclase hygrometer (Equation 7) is applied to 5 plagioclase (An_{24-38}) grains from Castilla et al. (2024), with a notable absence of H_2O gradients, to test the hygrometer and find equilibrium melt water concentrations of Cerro Machín magma. Cerro Machín H_2O concentrations in plagioclase measured by FTIR vary from 103 to 117 $\pm$ 11 ppm, corresponding to equilibrium melt H_2O contents ranging from 6.4 to 12.2 $\pm$ 0.4 wt.%. It must be noted that applying Equation 7 to this case requires extrapolation outside the experimental calibration H_2O content range (0.005–6.0 wt.%). However, the

lower end of the calculated values aligns with other H^+-in-plagioclase hygrometer estimates (constant partition coefficient ~0.002, 5.8–5.9 wt.%, Mosenfelder et al., 2020; square root function, 4.7–5.9 ± 1.0 wt.%, Castilla et al., 2024) and estimates derived from T-independent melt hygrometry (5.2–9.0 ± 1.6 wt.%; Cutler et al., 2024; Figure 3.7). In addition, the calculated melt water contents match the higher end of direct H_2O measurements from plagioclase (1.7–6.3 ± 0.5 wt.%) and quartz-hosted melt inclusion measurements (0.5–10.7 ± 0.9 wt.%; Castilla et al., 2024). Although the melt inclusions show a bias towards lower H_2O values, this is unsurprising as various processes may influence the integrity of melt inclusion records, such as the rapid diffusion of hydrogen in minerals and melts, which can result in rapid water loss in melt inclusions by post-entrapment diffusion (Barth et al., 2023). Significant reductions in pressure during magma ascent can also trigger the rupture of melt inclusions (e.g., Bachmann et al., 2010; Wallace et al., 2021). The composition of Cerro Machín plagioclase ($An_{24–48}$) also indicates the presence of melts with relatively high H_2O content. Experimental phase equilibrium studies demonstrate that $An_{27–66}$ plagioclase crystallises near or at water saturation (~7 wt.% at~220 MPa) at temperatures between 750 °c and 900 °c (Rutherford & Devine, 1996; Scaillet & Evans, 1999; Prouteau & Scaillet, 2003), relating to shallow crystallisation at Cerro Machín. The experimental temperature constraints overlap with estimates from H_2O-independent melt thermometry (Cutler et al., 2024) based on matrix and melt inclusion data, yielding temperatures between 680 and 850 °C (matrix median: 750 °C, melt inclusion median: 760 °C). The pyroclastic deposits also feature high-forsterite olivine (Fo_{89-92}) and amphibole (Mg# = 73–80; Castilla et al., 2024). Phase-equilibrium experiments on primitive magnesian andesites and high-Mg basalts demonstrate that these two phases coexist under water-saturated conditions at

pressures above 500 MPa, suggesting water contents exceeding 10 wt.% (Grove et al., 2003; Grove et al., 2005; Krawczynski et al., 2012). Furthermore, the combination of both high-forsterite olivine and high-Mg# amphibole in arc magmas is considered a characteristic feature of very hydrous magmatic systems (e.g., Goltz et al., 2020). Collectively, the range of H_2O concentrations observed in individual plagioclase crystals and melt inclusions, along with the presence of high-forsterite olivine and high-Mg# amphibole, suggests that the system underlying Cerro Machín is water-rich. Such hydrous systems are not uncommon and have been inferred using geophysical methods. For example, magnetotelluric studies have indicated the presence of water-rich silicic melts (>8 wt.%) in the Andean magmatic arc, showing a broad conduction zone linked to a low-velocity region at depths >20 km (~700 MPa; Brasse et al., 2002; Laumonier et al., 2017).

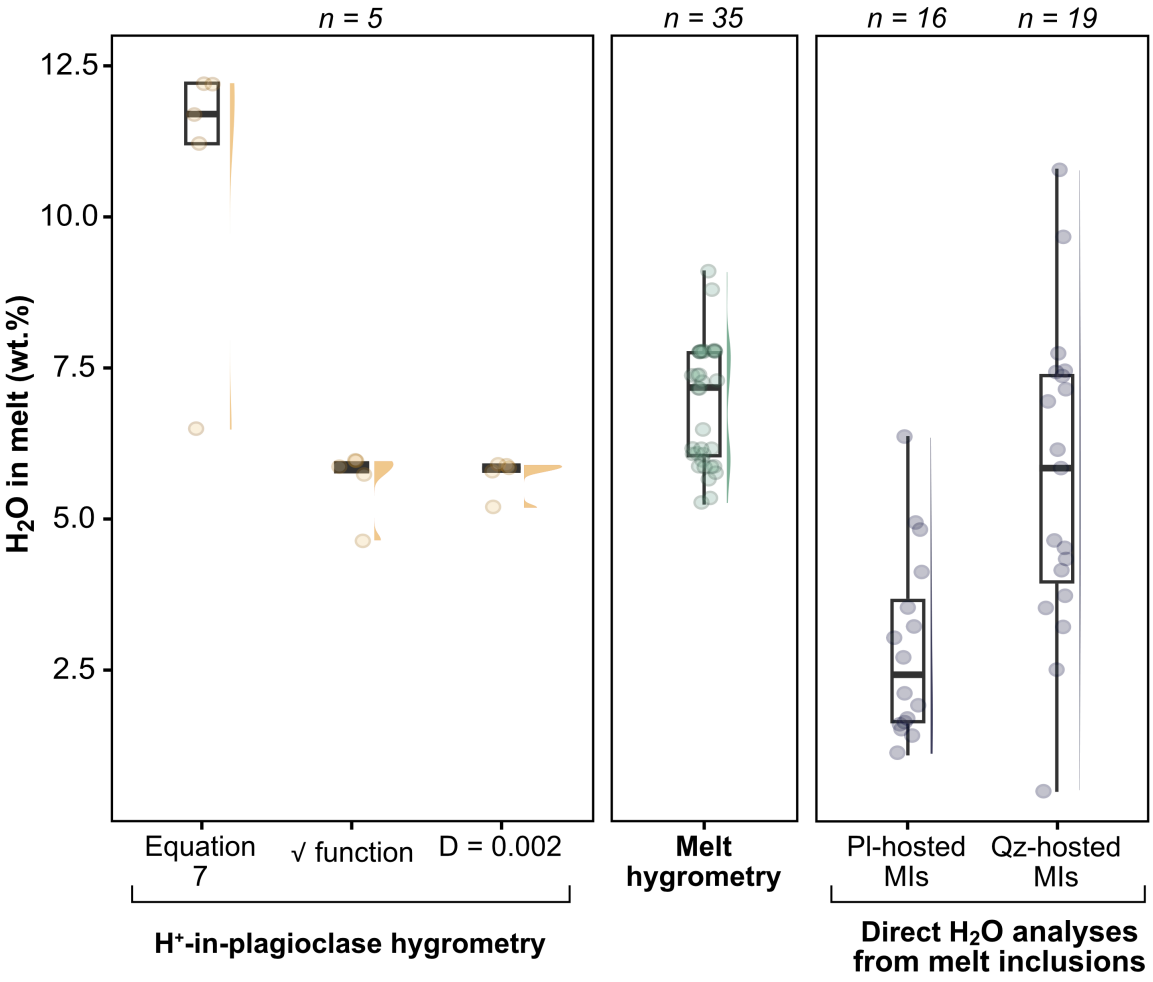

Figure 3.7 Comparison of H_2O content values from H^+-in-plagioclase hygrometry, melt hygrometry and analyses from melt inclusions. The H^+-in-plagioclase hygrometers include Equation 7 proposed in this study, the square root function from Castilla et al. (2024), and a constant partition coefficient for felsic melts from Mosenfelder et al. (2020). Melt hygrometry estimates derive from the T-independent plagioclase-saturated melt hygrometer of Cutler et al. (2024). Plagioclase and quartz-hosted melt inclusion data from Castilla et al. (2024).

3.5 Conclusion

This study presents new hydrogen plagioclase-melt partitioning data under hydrous haplogranitic and rhyolitic conditions (780–850 °C; 68–200 MPa; 2.01–4.58 wt.%). We show that H_2O concentrations in plagioclase depend on water fugacity in the melt using a power-law relation, but a constraint on XH_2O or pressure is required to derive melt water concentrations. In addition, as observed in previous studies, hydrogen partition coefficients are strongly dependent on the H_2O content of the melt, resulting in non-Henrian behaviour between H_2O concentrations in plagioclase and the melt, which can also be described by an empirical power-law relation. This parameterisation can be used as a new H^+-in-plagioclase hygrometer applied to lunar and terrestrial calc-alkaline melts for melt water contents between 0.005 and 6.0 wt.%. Applying the hygrometer to the hydrated plagioclase dataset of Castilla et al. (2024) returns equilibrium melt H_2O contents (6.4–12.2 $\pm$ 0.4 wt.%), consistent with other H^+-in-plagioclase hygrometers, plagioclase- and quartz-hosted melt inclusion data, and melt hygrometry.

References

Ardia, P., Di Muro, A., Giordano, D., Massare, D., Sanchez-Valle, C., & Schmidt, M. W. (2014). Densification mechanisms of haplogranite glasses as a function of water content and pressure based on density and Raman data. *Geochimica et Cosmochimica Acta*, *138*, 158-180. DOI: https://doi.org/10.1016/j.gca.2014.03.022

Aubaud, C., Withers, A. C., Hirschmann, M. M., Guan, Y., Leshin, L. A., Mackwell, S. J., & Bell, D. R. (2007). Intercalibration of FTIR and SIMS for hydrogen measurements in glasses and nominally anhydrous minerals. *American Mineralogist*, *92*(5-6), 811-828. DOI: https://doi.org/10.2138/am.2007.2248

Bachmann, O., Wallace, P. J., & Bourquin, J. (2010). The melt inclusion record from the rhyolitic Kos Plateau Tuff (Aegean Arc). *Contributions to Mineralogy and Petrology*, *159*, 187-202. DOI: https://doi.org/10.1007/s00410-009-0423-4

Barth, A., Plank, T., & Towbin, H. (2023). Rates of dehydration in hydrous, high-Fo, magmatic olivines. *Geochimica et Cosmochimica Acta*, *342*, 62-73. DOI: https://doi.org/10.1016/j.gca.2022.11.009

Beattie, P. (1993). On the occurrence of apparent non-Henry's Law behaviour in experimental partitioning studies. *Geochimica et Cosmochimica Acta*, *57*(1), 47-55. DOI: https://doi.org/10.1016/0016-7037(93)90467-B

Behrens, H., & Nowak, M. (2003). Quantification of H2O speciation in silicate glasses and melts by IR spectroscopy-in situ versus quench techniques. *Phase Transitions: A Multinational Journal*, *76*(1-2), 45-61. DOI: https://doi.org/10.1080/0141159031000076048

Behrens, H. (2021). Hydrogen defects in feldspars: defect properties and implications for water solubility in feldspar. *Physics and Chemistry of Minerals*, *48*, 1-22. DOI: https://doi.org/10.1007/s00269-020-01128-0

Bennett, E. N., Jenner, F. E., Millet, M. A., Cashman, K. V., & Lissenberg, C. J. (2019). Deep roots for mid-ocean-ridge volcanoes revealed by plagioclase-hosted

melt inclusions. *Nature*, *572*(7768), 235-239. DOI: https://doi.org/10.1038/s41586-019-1448-0

Blundy, J., & Cashman, K. (2005). Rapid decompression-driven crystallization recorded by melt inclusions from Mount St. Helens volcano. *Geology*, *33*(10), 793-796. DOI: https://doi.org/10.1130/G21668.1

Blundy, J., & Cashman, K. (2008). Petrologic reconstruction of magmatic system variables and processes. *Reviews in Mineralogy and Geochemistry*, *69*(1), 179-239. DOI: https://doi.org/10.2138/rmg.2008.69.6

Brasse, H., Lezaeta, P., Rath, V., Schwalenberg, K., Soyer, W., & Haak, V. (2002). The Bolivian altiplano conductivity anomaly. *Journal of Geophysical Research: Solid Earth*, *107*(B5), EPM-4. DOI: https://doi.org/10.1029/2001JB000391

Caseres, J. R., Mosenfelder, J. L., & Hirschmann, M. M. (2017, March). Partitioning of hydrogen and fluorine between feldspar and melt under the conditions of lunar crust formation. In *48th Annual Lunar and Planetary Science Conference* (No. 1964, p. 2303).

Caseres, J. R. (2019). *Water and fluorine contents in Mt. Hood magmas recorded by plagioclase phenocrysts* (Master's thesis, University of Minnesota).

Cashman, K. V. (2004). Volatile controls on magma ascent and eruption. *Geophysical Monograph Series*, *150*, 109-124. DOI: https://doi.org/10.1029/150GM10

Cassidy, M., Iveson, A. A., Humphreys, M. C., Mather, T. A., Helo, C., Castro, J. M., ... & EIMF. (2022). Experimentally derived F, Cl, and Br fluid/melt partitioning of intermediate to silicic melts in shallow magmatic systems. *American Mineralogist*, *107*(10), 1825-1839. DOI: https://doi.org/10.2138/am-2022-8109

Castilla, S. C., Newcombe, M. E., Piccoli, P. M., & Peterson, L. D. (2024). Crystals and melt inclusions record deep storage of superhydrous magma prior to the largest

known eruption of Cerro Machín volcano, Colombia. *Journal of Petrology*, *65*(9), egae095. DOI: https://doi.org/10.1093/petrology/egae095

Cutler, K. S., Cassidy, M., & Blundy, J. D. (2024). Plagioclase-saturated melt hygrothermobarometry and plagioclase-melt equilibria using machine learning. *Geochemistry, Geophysics, Geosystems, 25*(4), e2023GC011357. DOI: https://doi.org/10.1029/2023GC011357

Danyushevsky, L. V., Della-Pasqua, F. N., & Sokolov, S. (2000). Re-equilibration of melt inclusions trapped by magnesian olivine phenocrysts from subduction-related magmas: petrological implications. *Contributions to Mineralogy and Petrology*, *138*(1), 68-83. DOI: https://doi.org/10.1007/PL00007664

Da Silva, M. M., Holtz, F., & Namur, O. (2017). Crystallization experiments in rhyolitic systems: The effect of temperature cycling and starting material on crystal size distribution*. American Mineralogist: Journal of Earth and Planetary Materials, 102*(11), 2284-2294. DOI: https://doi.org/10.2138/am-2017-5981

Edmonds, M., Kohn, S. C., Hauri, E. H., Humphreys, M. C., & Cassidy, M. (2016). Extensive, water-rich magma reservoir beneath southern Montserrat. *Lithos*, *252*, 216-233. DOI: https://doi.org/10.1016/j.lithos.2016.02.026

Fischer, T. P., & Marty, B. (2005). Volatile abundances in the sub-arc mantle: insights from volcanic and hydrothermal gas discharges. *Journal of Volcanology and Geothermal Research*, *140*(1-3), 205-216. DOI: https://doi.org/10.1016/j.jvolgeores.2004.07.022

Gavrilenko, M., Ruprecht, P., & Krawczynski, M. (2025). The magmatic H2O pathway of ascending arc magmas recorded by Ca-in-olivine hygrometry: advantages, complications, and perspectives. *Contributions to Mineralogy and Petrology*, *180*(9), 1-23. DOI: https://doi.org/10.1007/s00410-025-02246-0

Goltz, A. E., Krawczynski, M. J., Gavrilenko, M., Gorbach, N. V., & Ruprecht, P. (2020). Evidence for superhydrous primitive arc magmas from mafic enclaves at

Shiveluch volcano, Kamchatka. *Contributions to Mineralogy and Petrology*, *175*, 1-26. DOI: https://doi.org/10.1007/s00410-020-01746-5

Grove, T.L., Elkins-Tanton, L. T., Parman, S., Chatterjee, N., Müntener, O., Gaetani, G. (2003). Fractional crystallization and mantle-melting controls on calc-alkaline differentiation trends. *Contributions to Mineralogy and Petrology*, *145*(5), 515–533. DOI: https://doi.org/10.1007/s00410-003-0448-z

Grove, T. L., Baker, M. B., Price, R. C., Parman, S. W., Elkins-Tanton, L. T., Chatterjee, N., & Müntener, O. (2005). Magnesian andesite and dacite lavas from Mt. Shasta, northern California: products of fractional crystallization of H 2 O-rich mantle melts. *Contributions to Mineralogy and Petrology*, *148*, 542-565. DOI: https://doi.org/10.1007/s00410-004-0619-6

Ghiorso, M. S., & Gualda, G. A. (2015). An H 2 O–CO 2 mixed fluid saturation model compatible with rhyolite-MELTS. *Contributions to Mineralogy and Petrology*, *169*, 1-30. DOI: https://doi.org/10.1007/s00410-015-1141-8

Hacker, B. R., Abers, G. A., & Peacock, S. M. (2003). Subduction factory 1. Theoretical mineralogy, densities, seismic wave speeds, and H2O contents. *Journal of Geophysical Research: Solid Earth, 108*(B1), 1–26. DOI: https://doi.org/10.1029/2001JB001127

Hamada, M., Ushioda, M., Fujii, T., & Takahashi, E. (2013). Hydrogen concentration in plagioclase as a hygrometer of arc basaltic melts: Approaches from melt inclusion analyses and hydrous melting experiments. *Earth and Planetary Science Letters*, *365*, 253-262. DOI: https://doi.org/10.1016/j.epsl.2013.01.026

Hamilton, D. T., & Henderson, C. M. B. (1968). The preparation of silicate compositions by a gelling method. *Mineralogical magazine and journal of the Mineralogical Society*, *36*(282), 832-838. DOI: https://doi.org/10.1180/minmag.1968.036.282.11

Hammer, J. E. (2008). Experimental studies of the kinetics and energetics of magma crystallization. *Reviews in mineralogy and geochemistry, 69*(1), 9-59. DOI: https://doi.org/10.2138/rmg.2008.69.2

Harvey, J., Yoshikawa, M., Hammond, S. J., & Burton, K. W. (2012). Deciphering the trace element characteristics in Kilbourne Hole peridotite xenoliths: melt–rock interaction and metasomatism beneath the Rio Grande Rift, SW USA. *Journal of Petrology*, *53*(8), 1709-1742. DOI: https://doi.org/10.1093/petrology/egs030

Hauri, E., Wang, J., Dixon, J. E., King, P. L., Mandeville, C., & Newman, S. (2002). SIMS analysis of volatiles in silicate glasses: 1. Calibration, matrix effects and comparisons with FTIR. *Chemical Geology*, *183*(1-4), 99-114. DOI: https://doi.org/10.1016/S0009-2541(01)00375-8

Humphreys, M. C., Kearns, S. L., & Blundy, J. D. (2006). SIMS investigation of electron-beam damage to hydrous, rhyolitic glasses: Implications for melt inclusion analysis. *American Mineralogist*, *91*(4), 667-679. DOI: https://doi.org/10.2138/am.2006.1936

Johnson, E. A., & Rossman, G. R. (2004). A survey of hydrous species and concentrations in igneous feldspars. *American Mineralogist*, *89*(4), 586-600. DOI: https://doi.org/10.2138/am-2004-0413

Johnson, E. A. (2005). Magmatic water contents recorded by hydroxyl concentrations in plagioclase phenocrysts from Mount St. Helens, 1980-1981. *Geochimica et Cosmochimica Acta Supplement*, *69*(10), A743.

Johnson, E. A., & Rossman, G. R. (2013). The diffusion behavior of hydrogen in plagioclase feldspar at 800–1000 C: Implications for re-equilibration of hydroxyl in volcanic phenocrysts. *American Mineralogist*, *98*(10), 1779-1787. DOI: https://doi.org/10.2138/am.2013.4521

Kirkpatrick, R. J. (1975). Crystal growth from the melt: a review. *American Mineralogist: Journal of Earth and Planetary Materials, 60*(9-10), 798-814.

Koga, K., Hauri, E., Hirschmann, M., & Bell, D. (2003). Hydrogen concentration analyses using SIMS and FTIR: Comparison and calibration for nominally anhydrous minerals. *Geochemistry, Geophysics, Geosystems*, *4*(2). DOI: https://doi.org/10.1029/2002GC000378

Kovács, I., Hermann, J., O'Neill, H. S. C., Gerald, J. F., Sambridge, M., & Horváth, G. (2008). Quantitative absorbance spectroscopy with unpolarized light: Part II. Experimental evaluation and development of a protocol for quantitative analysis of mineral IR spectra. *American Mineralogist*, *93*(5-6), 765-778. DOI: https://doi.org/10.2138/am.2008.2656

Krawczynski, M. J., Grove, T. L., & Behrens, H. (2012). Amphibole stability in primitive arc magmas: effects of temperature, H2O content, and oxygen fugacity. *Contributions to Mineralogy and Petrology*, *164*(2), 317-339. DOI: https://doi.org/10.1007/s00410-012-0740-x

Kumamoto, K. M., Warren, J. M., & Hauri, E. H. (2017). New SIMS reference materials for measuring water in upper mantle minerals. *American Mineralogist*, *102*(3), 537-547. DOI: https://doi.org/10.2138/am-2017-5863CCBYNCND

Langmuir, C. H., Bender, J. F., Bence, A. E., Hanson, G. N., & Taylor, S. R. (1977). Petrogenesis of basalts from the FAMOUS area: Mid-Atlantic Ridge. *Earth and Planetary Science Letters, 36*(1), 133-156. DOI: https://doi.org/10.1016/0012-821X(77)90194-7

Laumonier, M., Gaillard, F., Muir, D., Blundy, J., & Unsworth, M. (2017). Giant magmatic water reservoirs at mid-crustal depth inferred from electrical conductivity and the growth of the continental crust. *Earth and Planetary Science Letters*, *457*, 173-180. DOI: https://doi.org/10.1016/j.epsl.2016.10.023

Lin, Y. H., Hui, H., Li, Y., Xu, Y., & Van Westrenen, W. (2019). A lunar hygrometer based on plagioclase-melt partitioning of water. *Geochemical Perspectives Letters*, *10*, 14-19. DOI: https://doi.org/10.7185/geochemlet.1908

Lloyd, A. S., Ferriss, E., Ruprecht, P., Hauri, E. H., Jicha, B. R., & Plank, T. (2016). An assessment of clinopyroxene as a recorder of magmatic water and magma ascent rate. *Journal of Petrology*, *57*(10), 1865-1886. DOI: https://doi.org/10.1093/petrology/egw058

Luhr, J. F., & Aranda-Gómez, J. J. (1997). Mexican peridotite xenoliths and tectonic terranes: correlations among vent location, texture, temperature, pressure, and oxygen fugacity. *Journal of Petrology*, *38*(8), 1075-1112. DOI: https://doi.org/10.1093/petroj/38.8.1075

Madden-Nadeau, A. L. (2021). *Silicic caldera volcanism and the 1883 eruption of Krakatau Volcano, Indonesia* (Doctoral dissertation, University of Oxford).

Matthews, W., Linnen, R. L., & Guo, Q. (2003). A filler-rod technique for controlling redox conditions in cold-seal pressure vessels. *American Mineralogist*, *88*(4), 701-707. DOI: https://doi.org/10.2138/am-2003-0424

McIntosh, I. M., Aoki, K., Yanagishima, T., Kobayashi, M., Murata, M., & Suzuki, T. (2022). Reconstruction of submarine eruption processes from FTIR volatile analysis of marine tephra: Example of Oomurodashi volcano, Japan. *Frontiers in Earth Science*, *10*, 963392. DOI: https://doi.org/10.3389/feart.2022.963392

Melekhova, E., Blundy, J., Martin, R., Arculus, R., & Pichavant, M. (2017). Petrological and experimental evidence for differentiation of water-rich magmas beneath St. Kitts, Lesser Antilles. *Contributions to Mineralogy and Petrology*, *172*, 1-32. DOI: https://doi.org/10.1007/s00410-017-1416-3

Mitchell, A. L., Gaetani, G. A., O'leary, J. A., & Hauri, E. H. (2017). H 2 O solubility in basalt at upper mantle conditions. *Contributions to Mineralogy and Petrology*, *172*, 1-16. DOI: https://doi.org/10.1007/s00410-017-1401-x

Mollo, S., Masotta, M., Forni, F., Bachmann, O., De Astis, G., Moore, G., & Scarlato, P. (2015). A K-feldspar–liquid hygrometer specific to alkaline differentiated magmas. *Chemical Geology*, *392*, 1-8. DOI: https://doi.org/10.1016/j.chemgeo.2014.11.010

Moore, L. R., Gazel, E., Tuohy, R., Lloyd, A. S., Esposito, R., Steele-MacInnis, M., ... & Bodnar, R. J. (2015). Bubbles matter: An assessment of the contribution of vapor bubbles to melt inclusion volatile budgets. *American Mineralogist*, *100*(4), 806-823. DOI: https://doi.org/10.2138/am-2015-5036

Mosenfelder, J. L., Rossman, G. R., & Johnson, E. A. (2015). Hydrous species in feldspars: A reassessment based on FTIR and SIMS. *American Mineralogist*, *100*(5-6), 1209-1221. DOI: https://doi.org/10.2138/am-2015-5034

Mosenfelder, J. L., Andrys, J. L., von der Handt, A., Kohlstedt, D. L., & Hirschmann, M. M. (2020). Hydrogen incorporation in plagioclase. *Geochimica et Cosmochimica Acta*, *277*, 87-110. DOI: https://doi.org/10.1016/j.gca.2020.03.013

Muir, D. D., Blundy, J. D., Rust, A. C., & Hickey, J. (2014). Experimental constraints on dacite pre-eruptive magma storage conditions beneath Uturuncu volcano. *Journal of Petrology, 55*(4), 749-767. DOI: https://doi.org/10.1093/petrology/egu005

Murch, A. P., White, J. D., Dürig, T., Nichols, A. R., & Carey, R. J. (2024). Reconstructing the timing and conditions of fragmentation from water speciation in ash during a deep submarine eruption: 2012 eruption of Havre, Kermadec Arc. *Lithos*, *464*, 107432. DOI: https://doi.org/10.1016/j.lithos.2023.107432

Newcombe, M. E., Brett, A., Beckett, J. R., Baker, M. B., Newman, S., Guan, Y., ... & Stolper, E. M. (2017). Solubility of water in lunar basalt at low pH2O. *Geochimica et Cosmochimica Acta*, *200*, 330-352. DOI: https://doi.org/10.1016/j.gca.2016.12.026

Newman, S., & Lowenstern, J. B. (2002). VolatileCalc: a silicate melt–H2O–CO2 solution model written in Visual Basic for excel. *Computers & Geosciences*, *28*(5), 597-604. DOI: https://doi.org/10.1016/S0098-3004(01)00081-4

O'Leary, J. A., Gaetani, G. A., & Hauri, E. H. (2010). The effect of tetrahedral Al3+ on the partitioning of water between clinopyroxene and silicate melt. *Earth and Planetary Science Letters*, *297*(1-2), 111-120. DOI: https://doi.org/10.1016/j.epsl.2010.06.011

Perinelli, C., Mollo, S., Gaeta, M., De Cristofaro, S. P., Palladino, D. M., Armienti, P., ... & Putirka, K. D. (2016). An improved clinopyroxene-based hygrometer for Etnean magmas and implications for eruption triggering mechanisms. *American Mineralogist*, 101(12), 2774-2777. DOI: https://doi.org/10.2138/am-2016-5916

Pichavant, M., Weber, C., & Villaros, A. (2019). Effect of anorthite on granite phase relations: Experimental data and models. *Comptes Rendus. Géoscience*, *351*(8), 540-550. DOI: https://doi.org/10.1016/j.crte.2019.10.001

Popa, R. G., Bachmann, O., & Huber, C. (2021). Explosive or effusive style of volcanic eruption determined by magma storage conditions. *Nature Geoscience*, *14*(10), 781-786. DOI: https://doi.org/10.1038/s41561-021-00827-9

Rappoccio, R., Johnson, E. A., Myers, M., Wallace, P. J., & Wilson, C. J. (2020, December). Hydroxyl in Quartz and Feldspar Phenocrysts from the Bishop Tuff, CA, and the Huckleberry Ridge Tuff, Yellowstone. In *AGU Fall Meeting Abstracts* (Vol. 2020, pp. V003-0005).

Rasmussen, D. J., Plank, T. A., Roman, D. C., & Zimmer, M. M. (2022). Magmatic water content controls the pre-eruptive depth of arc magmas. *Science*, *375*(6585), 1169-1172. DOI: https://doi.org/10.1126/science.abm5174

Rueda, H. (2005). *Erupciones Plinianas del Holoceno en el Volcán Cerro Machín, Colombia, Estratigrafía, Petrografía y Dinámica Eruptiva* (Doctoral dissertation, Tesis

de Maestría (Inédito), Universidad Nacional Autónoma de México, Instituto de Geofísica, Posgrado en Ciencias de la Tierra: 118 p).

Sambridge, M., Gerald, J. F., Kovacs, I., O'Neill, H. S. C., & Hermann, J. (2008). Quantitative absorbance spectroscopy with unpolarized light: Part I. Physical and mathematical development. *American Mineralogist*, *93*(5-6), 751-764. DOI: https://doi.org/10.2138/am.2008.2657

Shearer, C. K., Hess, P. C., Wieczorek, M. A., Pritchard, M. E., Parmentier, E. M., Borg, L. E., ... & Wiechert, U. (2006). Thermal and magmatic evolution of the Moon. *Reviews in Mineralogy and Geochemistry*, *60*(1), 365-518. DOI: https://doi.org/10.2138/rmg.2006.60.4

Stolper, E. (1982). The speciation of water in silicate melts. *Geochimica et Cosmochimica Acta*, *46*(12), 2609-2620. DOI: https://doi.org/10.1016/0016-7037(82)90381-7

Ulmer, P., Kaegi, R., & Müntener, O. (2018). Experimentally derived intermediate to silica-rich arc magmas by fractional and equilibrium crystallization at 1· 0 GPa: an evaluation of phase relationships, compositions, liquid lines of descent and oxygen fugacity. *Journal of Petrology*, *59*(1), 11-58. DOI: https://doi.org/10.1093/petrology/egy017

Urann, B. M., Le Roux, V., Jagoutz, O., Müntener, O., Behn, M. D., & Chin, E. J. (2022). High water content of arc magmas recorded in cumulates from subduction zone lower crust. *Nature Geoscience*, *15*(6), 501-508. DOI: https://doi.org/10.1038/s41561-022-00947-w

Voigt, A., Cassidy, M., Castro, J. M., Pyle, D. M., Mather, T. A., Helo, C., ... & Kurniawan, I. A. (2022). Experimental investigation of trachydacite magma storage prior to the 1257 eruption of Mt Samalas. *Journal of Petrology*, *63*(8), egac066. DOI: https://doi.org/10.1093/petrology/egac066

Wade, J. A., Plank, T., Hauri, E. H., Kelley, K. A., Roggensack, K., & Zimmer, M. (2008). Prediction of magmatic water contents via measurement of H2O in clinopyroxene phenocrysts. *Geology, 36*(10), 799-802. DOI: https://doi.org/10.1130/G24964A.1

Wallace, P. J., Plank, T., Bodnar, R. J., Gaetani, G. A., & Shea, T. (2021). Olivine-hosted melt inclusions: a microscopic perspective on a complex magmatic world. *Annual Review of Earth and Planetary Sciences*, *49*(1), 465-494. DOI: https://doi.org/10.1146/annurev-earth-082420-060506

Waters, L. E., & Lange, R. A. (2015). An updated calibration of the plagioclase-liquid hygrometer-thermometer applicable to basalts through rhyolites. *American Mineralogist*, *100*(10), 2172-2184. DOI: https://doi.org/10.2138/am-2015-5232

Xu, Y., Lin, Y., Zheng, H., & van Westrenen, W. (2024). Non-Henrian behavior of hydrogen in plagioclase–basaltic melt partitioning. *Chemical Geology*, *661*, 122153. DOI: https://doi.org/10.1016/j.chemgeo.2024.122153

Yang, X. (2012). An experimental study of H solubility in feldspars: effect of composition, oxygen fugacity, temperature and pressure and implications for crustal processes. *Geochimica et Cosmochimica Acta*, *97*, 46-57. DOI: https://doi.org/10.1016/j.gca.2012.08.036

4 | Identifying volcanoes with the potential for large-magnitude eruptions using supervised and unsupervised machine learning

Abstract

Identifying volcanoes capable of generating large-magnitude eruptions (M≥6) is crucial, given their potential for global environmental and socioeconomic impacts. Various factors, such as high magma flux and large edifice size, have been proposed to explain what drives volcanoes to erupt explosively at a magnitude of 6 or higher. Here, we test a data-driven approach to identify the key factors contributing to high-magnitude eruptions. We compile a database of 150 arc volcanoes, including 22 variables (e.g., eruptive records, morphology, geochemistry, tectonic setting) to develop a machine learning classifier that recognises whether a volcano has experienced prior M≥6 eruptions. The classifier suggests that larger magnitude eruptions originating from arc volcanoes are more mature, possess large edifices, and exhibit a greater range of eruptive compositions, with the model classifying volcanoes with a 70% accuracy. These factors are consistent with being proxies for describing the size, distribution, and thermal maturity of magmatic systems, all correlating to eruption magnitude (i.e., Weber and Sheldrake, 2022; Lerner et al., 2020; Karakas et al., 2017; Higgins and Caricchi, 2023). Using these key characteristics from correctly classified volcanoes with prior M≥6 eruptions, we apply hierarchical clustering to determine analogue volcanoes with similar characteristics, creating a total list of 64 volcano candidates. 22% of these volcano candidates overlap with a 'manual' list compiled by Newhall et al. (2018) of arc volcanoes thought to produce a large-magnitude eruption in the future. These volcano candidates highlight possible volcanoes that could be explored to improve short-term eruption forecasting and hazard assessments. Despite the limited

dataset, these results offer a hypothesis that can be tested and refined through expanded data collection of the most significant proxies (i.e., edifice morphology, SiO_2 95th percentile range, and number of Pleistocene eruptions).

4.1 Introduction

Large-magnitude explosive eruptions occur at least once every 110 or 1,200 years for magnitude (M) 6 or 7 eruptions, respectively (Rougier et al., 2018). Given that approximately 60 million people live within 10 km of a Holocene volcano (Freire et al., 2019), such events pose a catastrophic risk to human populations and the environment (e.g., McCormick et al., 1995; Parker et al., 1996; Nooren et al., 2017; Stocker et al., 2024). Increased globalisation has resulted in key infrastructures and networks emerging in certain geographical areas coinciding with active volcanic regions, known as 'pinch points' (Mani et al., 2021), highlighting the need to identify areas of heightened vulnerability to volcanic threats and improve systematic forecasting and monitoring efforts (Cassidy and Mani, 2022).

Forecasting eruptions mainly requires a comprehensive record of eruptive behaviour; however, many volcanoes erupt infrequently and/or have limited available data, with an estimated 70% of the world's Holocene volcanoes remaining inadequately studied (Loughlin et al., 2015). Using modelling and detailed case studies, several factors have been proposed to explain what contributes to the occurrence of large-magnitude eruptions. For instance, Sheldrake et al. (2020) used probabilistic modelling of tectonic features to suggest that eruptive size is strongly linked to convergence obliquity, finding that volcanic arcs characterised by low convergence obliquity and moderate subducting slab ages tend to favour the storage and accumulation of large magma volumes. Furthermore, Weber and Sheldrake

(2022) used whole-rock SiO_2 variance to demonstrate that volcanoes with a record of at least one caldera-forming eruption exhibit greater SiO_2 variability than those that do not. Newhall et al. (2018) also assembled a list of candidate volcanoes capable of large-magnitude eruptions, selecting them based on six criteria identified from a literature review of volcanoes that previously experienced such eruptions. These criteria include high magma fluxes from depth and mature stratovolcanoes with large edifice volumes (>200 km^3). While the aforementioned studies have identified multiple factors, such as specific tectonic or geochemical parameters, that contribute to large-magnitude eruptions, it is essential to determine the most critical factors to guide future volcanic data collection and improve hazard assessments. Nonetheless, analysing a complex, multi-dimensional dataset of volcanoes remains challenging without the use of machine learning algorithms, which have become increasingly popular over the past twenty years (e.g., Jordan and Mitchell, 2015; Wang et al., 2023). These algorithms have been highly effective in various scientific fields, capable of analysing large datasets and detecting subtle patterns that are not obvious to the human eye (Petrelli et al., 2024).

In this study, we compile various data (i.e., eruptive records, morphology, geochemistry, tectonic setting) on arc volcanoes that may serve as proxies for underlying magmatic processes to test the existing hypotheses mentioned. We test different ensemble classification machine learning algorithms to identify what key factors the models use to predict which volcanoes have experienced prior large-magnitude ($M \geq 6$) eruptions. Using the key attributes associated with accurately identified volcanoes from the classifier test sets, we apply hierarchical clustering to find analogue volcanoes, compiling a list of candidate volcanoes that could be further investigated to improve monitoring.

4.2 Datasets and statistical methods

4.2.1 Dataset compilation and pre-processing

The compilation focused on arc volcanoes due to the greater availability of data on these volcanoes from global databases. The dataset covers a range of characteristics such as edifice morphology, subduction zone features, geochemistry, and eruptive histories. Eruption records for each volcano during the Pleistocene and Holocene were sourced from the LaMEVE database (Crosweller et al., 2012) and the Global Volcanism Program database (GVP; Siebert and Simkin, 2002), providing an insight into the activity levels of each volcanic system. Key morphological features of volcanoes, such as edifice height, volume, basal area, summit area, and number of peaks, were compiled from the databases of Grosse et al. (2014) and Grosse and Kervyn (2018); several edifice volume values were substituted with updated estimates from Lerner et al. (2020). These features were included because they can act as proxies for long-term magma flux of volcanoes (Lerner et al., 2020; Higgins and Caricchi, 2023). Tectonic controls, such as convergence obliquity and subducting slab age, have previously been linked to eruption magnitude (Sheldrake et al., 2020). Therefore, various subduction-related characteristics were considered, including plate velocities, obliquities, and the age of the subducting slab at the nearest subduction zone arc segment to the volcano, all taken from Heuret (2006) and Lallemand et al. (2005). The depth, dip, strike, and thickness of the subducting slab for each volcano were obtained from the Slab2 model (Hayes et al., 2018). Crustal thickness estimates— excluding water layers —were calculated from the global crustal model CRUST1 (Laske et al., 2013), and values for the minimum effective elastic thickness of the crust were sourced from Tesauro et al. (2012). Bulk-

rock SiO_2 and trace element data were compiled from the GEOROC (https://georoc.mpchmainz.gwdg.de/georoc/) and EarthChem (https://www.earthchem.org) databases. SiO_2, among the major elements, was chosen as it provides the most reliable indicator of plumbing system size (Weber and Sheldrake, 2022). We also examined trace elements because they are indicators of various magmatic processes in subduction zones, such as the presence of melted slab components (e.g., Ba/Nb; Singer et al., 2007) or slab fluids in arc magmas (e.g., Ba/La; Elliott, 2003). Variability in SiO_2 and trace elements was calculated using the 95^{th} percentile range, calculating the difference between the 97.5^{th} and 2.5^{th} percentiles to exclude outliers (Weber and Sheldrake, 2022). For trace elements, 95^{th} percentile ranges were determined for both individual trace elements (Nb, La, Ce, Pr, Nd, Sm, Eu, Yb, Th, U, Pb, Zr, Cs, Ba, Y, and Sr) and significant geochemical ratios (Zr/Nb, Ba/La, Ba/Nb, La/Yb, Th/Yb, Th/La, Nb/U, La/Nb, Zr/Y, Sr/Y, and Ce/Pb; Lubbers et al., 2023). All geochemical data were transformed using centred log-ratio transformation (CLR) to address the effects of data closure (Aitchison, 1982). Additional factors that could be valuable to include in the dataset in the future are the magmatic water and crystallinity content of deposits, as Popa et al. (2021) show that magmas generally erupt explosively when they have a low crystallinity volume of <30% and dissolved water contents between 4 and 5.5 wt.%, based on analyses of eruptive patterns from 245 eruptions worldwide. This is consistent with numerical modelling from Castruccio et al. (2025), which indicates that effusive eruptions tend to favour conditions with low or high-end dissolved water contents and high crystallinity, due to efficient outgassing through porous crystal networks during ascent (Oppenheimer et al., 2015; Colombier et al., 2020).

Handling continuous variables with missing values is a typical pre-processing step for machine learning problems. In this instance, we excluded volcanoes with missing values from the overall dataset. Since most of the missing values come from the trace element data, we created two datasets for testing (Figure 4.1): Dataset 1 (*n* = 67) includes 49 variables with all trace element data, whereas Dataset 2 (*n* = 150) contains 21 variables (Supplementary Table 4.1). The final pre-processing step involved standardising (i.e. centring and scaling) the datasets using the open-source programming language R.

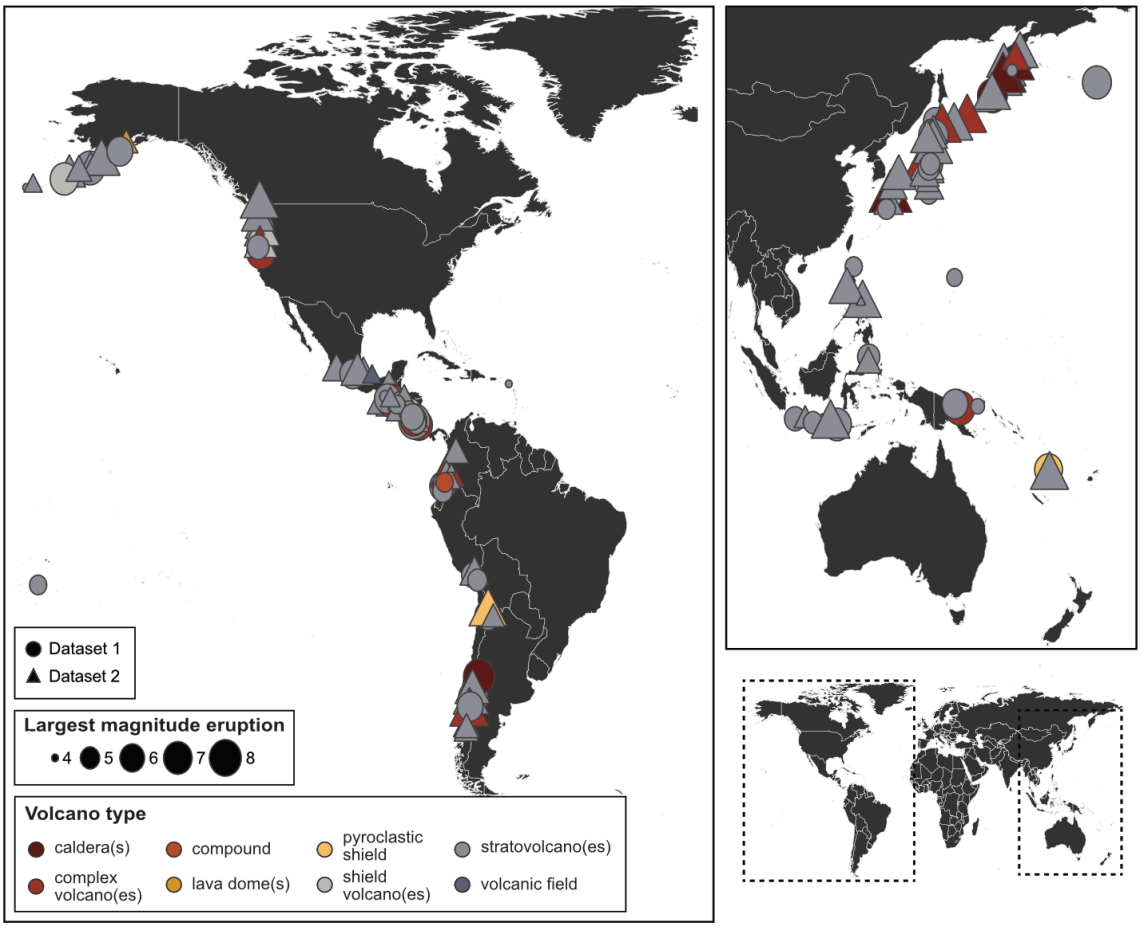

Figure 4.1 Distribution of arc volcanoes compiled in both datasets. The world map indicates the location of volcanoes by type and by the largest magnitude eruption recorded in LaMEVE (Crosweller et al., 2012). The main difference between the two datasets is the inclusion of trace element data in Dataset 1.

4.2.2 Classification workflow

Supervised classification is a machine-learning task that sorts samples within a dataset into known classes. In this case, the classifier aims to accurately predict the volcanoes with a prior large-magnitude eruption ($M \geq 6$, $n_{total} = 62$; $M = \log_{10}$[erupted mass in (kg)] – 7, Pyle, 2000). We tested an ensemble and a boosting algorithm for classification—random forest and gradient boosting—as these algorithms have proven effective at preventing model overfitting on smaller datasets (e.g., Qi, 2012; Robinson et al., 2020; Luan et al., 2020). The random forest algorithm combines the output of numerous decision trees (i.e., a “forest”) to reach an overall outcome (Talekar and Agrawal, 2020). In contrast, gradient-boosting is an iterative decision tree algorithm that builds a strong model by sequentially adding weak trees, each aiming to correct the errors of the previous trees (Biau et al., 2019). The algorithms were implemented using the ‘ranger' package (Wright and Ziegler, 2017) and the 'GBM (Gradient Boosting Machine)' package (Greenwell et al., 2019), both within the 'Caret' framework (Kuhn, 2008).

A key component of building classification models is selecting an optimal range of features (e.g., eruptive record, morphological, tectonic, and geochemical variables) to assist the model in predicting the target class (e.g., a volcano with records of an $M \geq 6$ eruption). To reduce the number of features, we used the Recursive Feature Elimination (RFE) method in the Caret package (Kuhn, 2008) with the random forest algorithm. This technique systematically eliminates less important features, concentrating on those that enhance predictive accuracy. RFE was performed 30 times with each dataset to account for variance in model performance metrics.

The primary workflow for developing classification models using the random forest and GBM algorithms involves the following steps: 1) partitioning the dataset into

training and testing sets with an 80/20 ratio and stratified sampling, ensuring that the testing set is not used during model calibration. Stratified sampling guarantees a balanced distribution of target classes in both the training and testing sets. The models also undergo 10-fold cross-validation, where the training set is divided into 10 subsets (or folds). Each fold is iterated by treating one as the testing set while the remaining folds serve as the training data. The model is trained and evaluated in each iteration, with performance measured as the average across all iterations. It is worth noting that model performance with k-fold cross-validation may be prone to bias when using small sample sizes, particularly in the case of Dataset 1. 2) Models can be optimised further by tuning various hyperparameters with each algorithm; here, we use the automatic hyperparameter tuning in the Caret package. 3) To evaluate the models, steps 1 and 2 were performed 30 times to allow for different testing and training set partitioning splits and to average the variance of the final performance metrics. The primary metric used to quantify classification model performance is accuracy, with scores ranging from 0 to 1, where 1 indicates that all predictions match the observed classification:

$$Accuracy = \frac{TP+TN}{TP+TN+FP+FN} \quad (1)$$

where TP and TN denote true positives and true negatives, while FP and FN denote false positives and false negatives. While the accuracy metric informs us about the overall performance of the model, we can also compute the number of correct or incorrect predictions. Precision indicates what proportion of true positive classifications were correct (i.e., the volcano has experienced a large-magnitude eruption):

$$Precision = \frac{TP}{TP+FP} \quad (2)$$

Similarly, the model recall tells us what proportion of TP classifications were identified:

$$Recall = \frac{TP}{TP+FN} \quad (3)$$

Commonly, precision and recall scores are combined into one metric named the F_1 score:

$$F_1 = 2\frac{Precision \cdot Recall}{Precision+Recall} \quad (4)$$

4.2.3 Agglomerative hierarchical clustering

Due to the small size of the input datasets, we do not have an independent test set to thoroughly evaluate the classifiers. Instead, using the most effective classifier model, we filter the volcanoes that have been consistently classified accurately (i.e., true positives) from all test sets and use them to identify analogue volcanoes with comparable features using agglomerative hierarchical clustering (e.g., Burgos et al., 2023). We have adopted this unsupervised approach as clustering may identify other volcano candidates that have not experienced prior M≥6 eruptions but still exhibit M≥6 eruption-associated characteristics recognised by the classifier. Furthermore, clustering could reveal a wider range of volcano candidates with prior M≥6 eruptions that may not have been included in any test set partitioning splits. One key benefit of hierarchical clustering is that it eliminates the need to pre-define the number of

clusters (i.e., the analysis is unsupervised). Agglomerative hierarchical clustering starts with each observation (volcano) as an individual cluster. To cluster the data, we calculate a measure of dissimilarity (or distance), which in this case is the Euclidean distance. The algorithm then merges the two clusters closest to each other based on the Euclidean distance, continuing this process until all clusters converge into one large cluster. Next, we select a linkage method that defines the dissimilarity between clusters, testing four methods: single, complete, average, and Ward's. The method with the highest agglomerative coefficient is retained, indicating the strength of the clustering structure, with values nearer to 1 signifying a robust clustering structure (Kaufman and Rousseeuw, 1991). The clustering tendency of the input data can also be assessed using the Hopkins statistic, which estimates the likelihood that the dataset was generated by a random uniform distribution (Lawson and Jurs, 1990). Values close to 1 indicate that the input dataset is easy to cluster. The clustering analysis was performed with the 'hclust' function from the 'stats' package in R.

4.3 Results

4.3.1 Feature selection

The optimal number of features used by the classifier for Dataset 1 (n_{total} = 67 volcanoes; 49 variables) is 46, achieving a median accuracy of 0.60. In contrast, Dataset 2 (n_{total} = 150 volcanoes; 22 variables) displays the best results with just three features and a median accuracy of 0.67 (Figure 4.2). As a result, we will concentrate on developing a classifier using Dataset 2. The top features in Dataset 2 used by the classifier are determined through feature importance using Gini impurity in Caret, which evaluates each feature's role based on its ranking in the decision

nodes of a tree and its effect on the target class's predictability (Louppe et al., 2013). Features positioned higher in the tree have a greater influence on the final classification compared to those at lower levels. The classifier consistently uses three main features across the 30 recursive feature elimination runs: the number of Pleistocene eruptions, the SiO_2 95th percentile range, and the basal area of the volcano (Table 4.1).

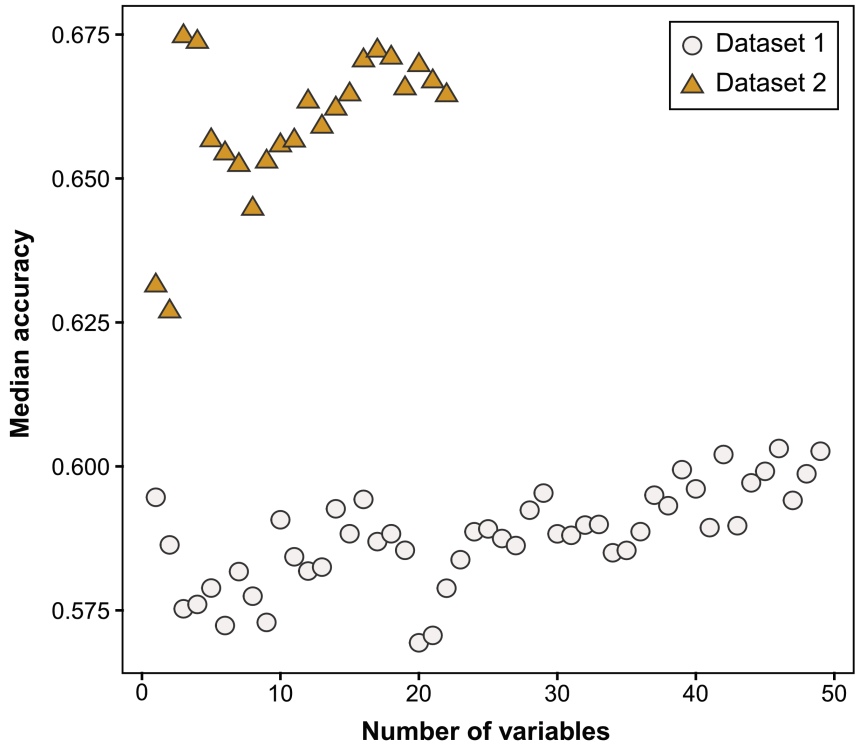

Figure 4.2 Median accuracy scores of all 30 recursive feature elimination runs for each dataset. The random forest classifier performs optimally with three variables using Dataset 2, yielding the highest median accuracy of 0.67.

4.3.2 Classification model performance

Figure 4.3 displays the cross-validation and test set performance of the random forest and gradient-boosted machine models. The gradient-boosted machine outperformed the random forest algorithm, achieving higher median cross-validation

accuracy (0.75) and test set scores (0.70) compared to the random forest's cross-validation accuracy and test set scores of 0.73 and 0.67, respectively. The test sets' precision, recall and F1 scores are also higher for GBM, with values of 0.67, 0.61 and 0.63, respectively (Figure 4.4a, 4.4b, 4.4c).

Filtering the test sets to determine the true positive volcanoes (i.e., those accurately classified) reveals Newberry, Gorely, and Okmok as the top three among 43 volcanoes, each with ≥10 correct classifications across 30 model runs (Table 4.2). All 43 volcanoes exhibit common traits, including large basal edifice areas (mean: 204 km²), elevated SiO_2 95th percentile range values (mean: 18.0 wt.%), and an average of two Pleistocene eruptions (Figure 4.5). In contrast, the top volcanoes labelled as false positives (i.e., volcanoes predicted to have experienced M≥6 eruptions, but there are no records of them having done so) (n_{total} = 20; Table 4.3), include Mount Jefferson, Kirishimayama, Fuji, Hachijojima, and Zaozan, and have ≥7 incorrect classifications across the 30 model runs. They exhibit high SiO_2 range values akin to the true positives (mean: 18.0 wt.%) and an average of 3 Pleistocene eruptions, yet have smaller basal edifice areas (mean: 88 km²). Raung, Doña Juana, and San Salvador represent the top three true negative volcanoes (i.e., volcanoes that the model has accurately classified as not having produced M≥6 eruptions, n_{total} = 73; Table 4.4) with ≥11 correct classifications across all model runs. These volcanoes typically share traits of lower SiO_2 range values (mean: 12.6 wt.%), smaller basal edifice areas (mean: 70.0 km²), and an average of one Pleistocene eruption. The top volcanoes identified as false negatives (i.e., volcanoes that have produced M≥6 eruptions but the model incorrectly classifies them, n_{total} = 31; Table 4.5) —Quizapu, Pacaya, Cosigüina, Santa María, and Villarrica—account for ≥8 incorrect classifications across the 30 model runs. Similar to the true negative

volcanoes, the false negative volcanoes have low SiO_2 range values (mean: 13.1 wt.%) and small basal edifice areas (mean: 103 km²), but have a higher average record of two Pleistocene eruptions.

Table 4.1 Results of recursive feature elimination. All 22 features are ranked in descending order based on how frequently they are selected as the features for the optimal model across the 30 RFE runs.

Feature	n
Pleistocene eruptions	30
SiO_2	29
Basal area (km^2)	28
Summit area (km^2)	20
Slab dip	20
Edifice height (m)	19
Edifice volume (km^3)	17
Obliquity of the trench velocity	17
Crustal thickness (km)	15
No of peaks	15
Holocene eruptions	14
Slab strike	14
Slab thickness	14
Obliquity of the convergent velocity	13
Normal component of the convergent velocity	13
Normal component of the subducting velocity	13
Slab depth	13
Obliquity of the subducting velocity	12
Subducting plate age (Ma)	7
Normal component of the trench velocity	5
Minimum effective elastic thickness (km)	3
Normal component of the back-arc strain rate	3

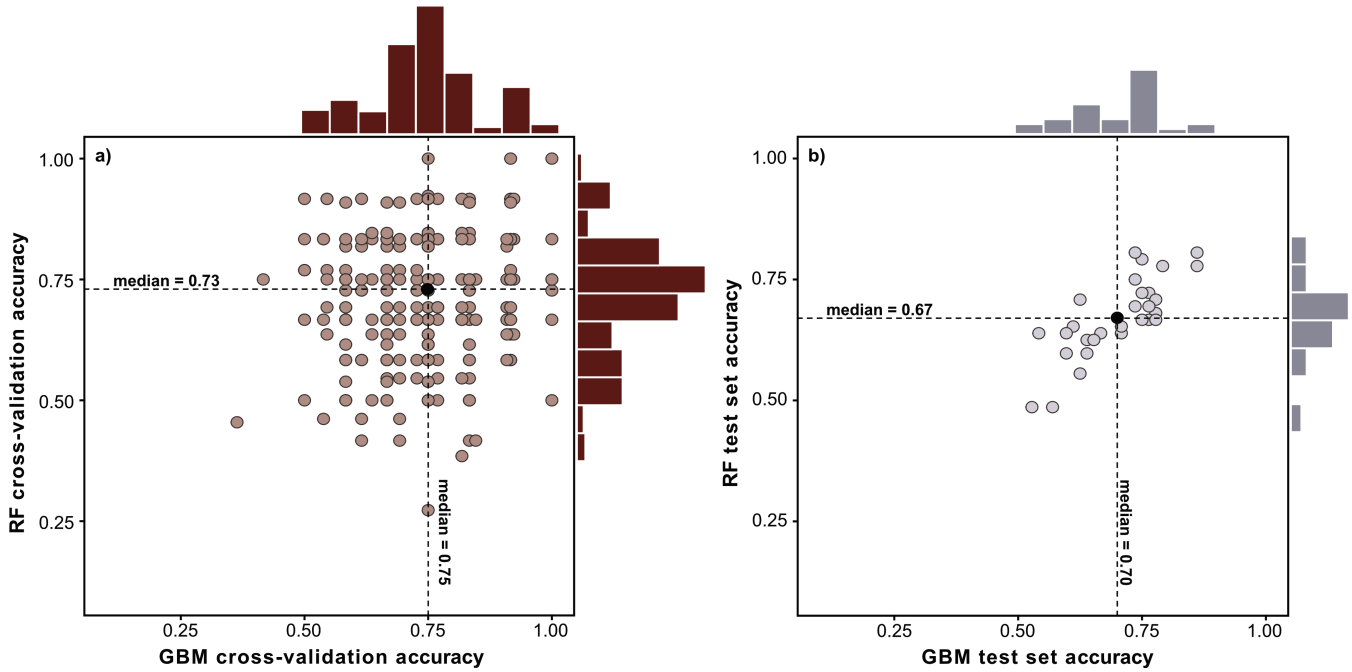

Figure 4.3 Cross-validation training (**a**) and test set accuracy (**b**) scores for the random forest (RF) and gradient-boosted machine (GBM) models.

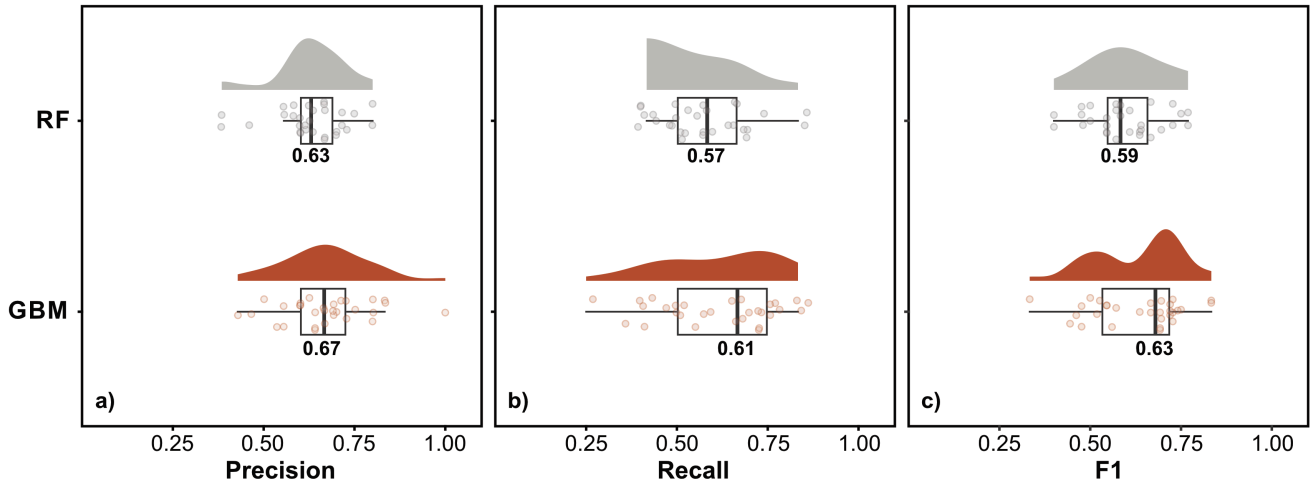

Figure 4.4 Test set precision (**a**), recall (**b**), and F1 scores (**c**) for the random forest (RF) and gradient-boosted machine (GBM) models.

4.3.3 Analogues from clustering

We used Newberry Volcano as an example to identify analogues, as it was the most accurately classified volcano (Table 4.2). Newberry is a broad shield-shaped composite volcano in central Oregon, located ~50 km east of the main Cascades arc. Figure 4.6 illustrates the dendrogram from the hierarchical cluster analysis based on the number of Pleistocene eruptions, SiO_2 range, and basal area features from Dataset 2. Ward's linkage method achieves the highest agglomerative coefficient of 0.98 (Ward, 1963), highlighting a strong clustering structure in the dendrogram. The Hopkins statistic of 0.82 also corroborates this result, indicating that the dataset is conducive to clustering. Medicine Lake is the volcano most similar to Newberry, as seen by the grouping on the dendrogram (Figure 4.6), followed closely by Ksudach. Nine other volcanoes appear in the same cluster (e.g., Ambrym, Pinatubo, Puyehue-Cordón Caulle, Tambora, Veniaminof, Westdahl, Barva, Long Island, Guagua Pichincha), with all volcanoes in the cluster sharing the key characteristic of a large edifice basal area (390–909 km^2). Out of the twelve volcanoes, ten have recorded at least one eruption of magnitude 6 or greater in the past, with the exceptions being Westdahl (USA) and Guagua Pichincha (Ecuador).

Table 4.2 Volcanoes classified as true positives (i.e., volcanoes with a prior M≥6 eruption that the model correctly identifies) and their frequency across the 30 GBM model runs.

Volcano	Frequency
Newberry	11
Gorely	10
Okmok	10
Galeras	9
Long Island	9
Puyehue-Cordón Caulle	9
Moyorodake//Medvezhya	7
North Vate//Nguna-Emau	7
Aira//Sakurajima	6
Avachinsky	6
Bulusan	6
Katmai	6
Ksudach	6
Maipo	6
Rincón de la Vieja	6
Semisopochnoi//Mt Cereberus	6
St Helens//Lawetlat'la	6
Emmons Lake	5
Opala	5
Pinatubo	5
Toya//Usu	5
Akita-Yakeyama	4
Ambrym	4
Atitlán	4
Harunasan	4
Krasheninnikov	4
Miravalles	4
Mt Baker/Kulshan	4
Nevado de Toluca	4
Popocatépetl	4
Tambora	4
Barva	3
Copahue	3
Khangar	3
Nemo Peak	3
Nevados de Chillán	3
Apaneca Range	2
Chiltepe//Apoyeque	2
Láscar	2
Medicine Lake	2

Ontakesan	2
Raususan//Mendeleev	2
Shiveluch//Sheveluch	2

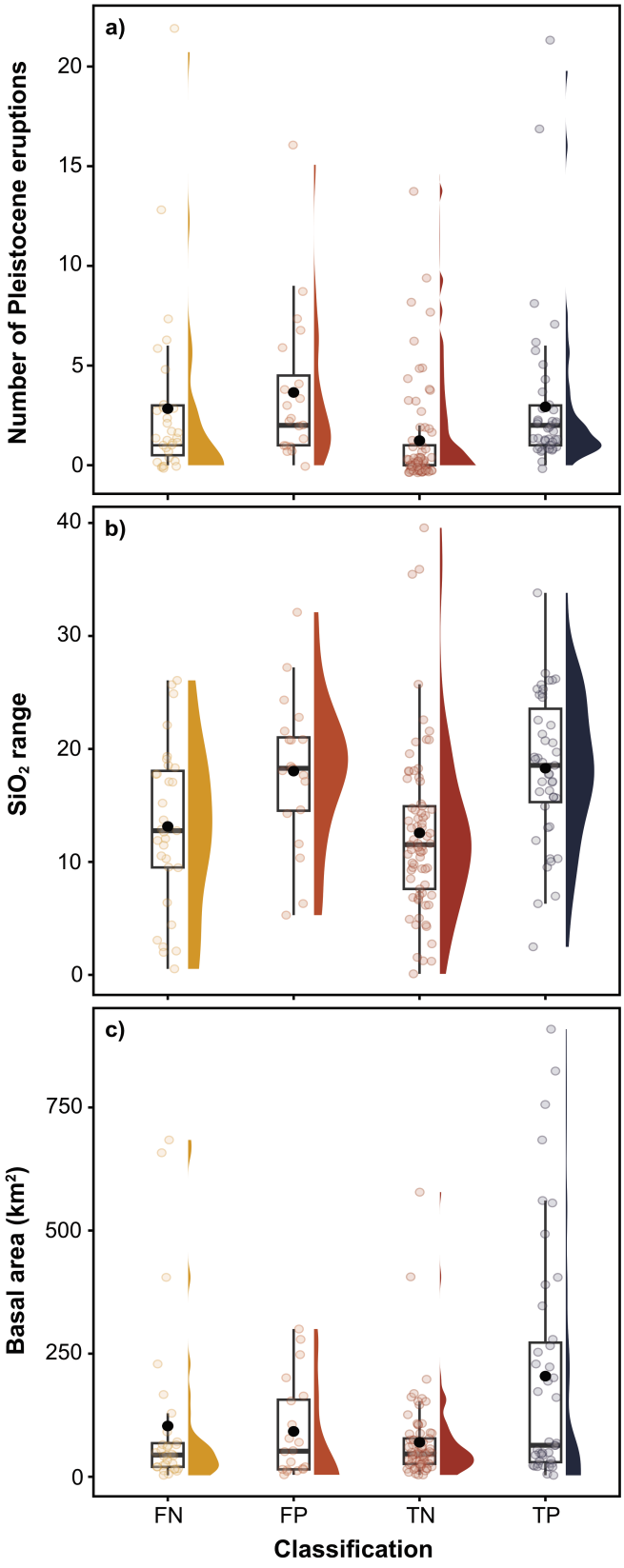

Figure 4.5 Raincloud plots illustrate the variation in the number of Pleistocene eruptions (**a**), the SiO_2 95th percentile range (**b**), and the basal area of volcanoes (km^2; **c**) across all classifications (TP, true positive; FP, false positive; TN, true negative; FN, false negative). The black horizontal lines are the median values, and the black circles are the mean values.

Table 4.3 Volcanoes classified as false positives (i.e., volcanoes predicted to have a prior M≥6 eruption, but do not have one) and their frequency across the 30 GBM model runs.

Volcano	Frequency
Mount Jefferson	11
Kirishimayama	9
Fujisan	7
Hachijojima	7
Zaozan	7
Myokosan	6
Tolbachik	6
Bandaisan	5
Citlaltépetl//Pico de Orizaba	5
Hokkaido-Komagatake	5
Ilyinsky	5
Cerro Tuzgle	4
Karymsky	4
Mount Rainier	4
Nevado del Ruiz	4
Takaharayama	4
Asamayama	3
Mt Shasta//Úytaahkoo	3
Mikurajima	2
Mocho-Choshuenco	2

Table 4.4 Volcanoes classified as true negatives (i.e., volcanoes with no record of a previous M≥6 eruption that the model correctly identifies) and their frequency across the 30 GBM model runs.

Volcano	Frequency
Raung	12
Doña Juana	11
San Salvador	11
Arenal	10
Hakusan	10
Suwanosejima	10
Three Sisters	10
Aogashima	9
Izu-Oshima	9
Liamuiga	9
Lonquimay	9
Turrialba	9
Agung	8
Akutan	8
Glacier Peak	8
Makushin	8
Sarychev Peak	8
Bezymianny	7
Corcovado	7
Fuego	7
Guagua Pichincha	7
Kanaga	7
Llaima	7
Mayon	7
Melimoyu	7
Raikoke	7
Yanteles	7
Alaid	6
Alamagan	6
Atacazo	6
Babuyan Claro	6
Chachadake/Tiatia	6
Kharimkotan	6
Momotombo	6
San Martín	6
Tacaná	6
Ubinas	6
Yakedake	6
Adatarayama	5

Awu	5
El Misti	5
Iwatesan	5
Kizimen	5
Kujusan	5
Miyakejima	5
Westdahl	5
Augustine	4
Cayambe	4
Concepción	4
Kasatochi	4
Kelut	4
Mocho-Choshuenco	4
Nantaisan	4
Norikuradake	4
Pavlof	4
Puracé	4
Rishirizan	4
Yucamane	4
Colima	3
Fonualei	3
Kuchinoerabujima	3
Merapi	3
Mikurajima	3
Osorno	3
Reventador	3
Soche	3
Takaharayama	3
Fujisan	2
Galunggung	2
Hachijojima	2
Myokosan	2
Ulawun	2
Yoteizan	2

Table 4.5 Volcanoes classified as false negatives (i.e., volcanoes with a prior M≥6 eruption, but are predicted not to have one) and their frequency across the 30 GBM model runs.

Volcano	Frequency
Cerro Azul	10
Pacaya	9
Cosigüina	8
Santa María	8
Villarrica	8
Karkar	6
Taisetsuzan	6
Tecapa	6
North Vate//Nguna-Emau	5
Purico Complex	5
Tao-Rusyr Caldera//Krenitsyn Peak	5
Katmai	4
Nasudake	4
Veniaminof	4
Ambrym	3
Apaneca Range	3
Copahue	3
Krasheninnikov	3
Lassen Volcanic Center	3
Ontakesan	3
Oshima-Oshima	3
Rinjani	3
Cotopaxi	2
Khangar	2
Láscar	2
Long Island	2
Nemo Peak	2
Nevado de Toluca	2
Nikko-Shiranesan	2
Opala	2
St Helens//Lawetlat'la	2

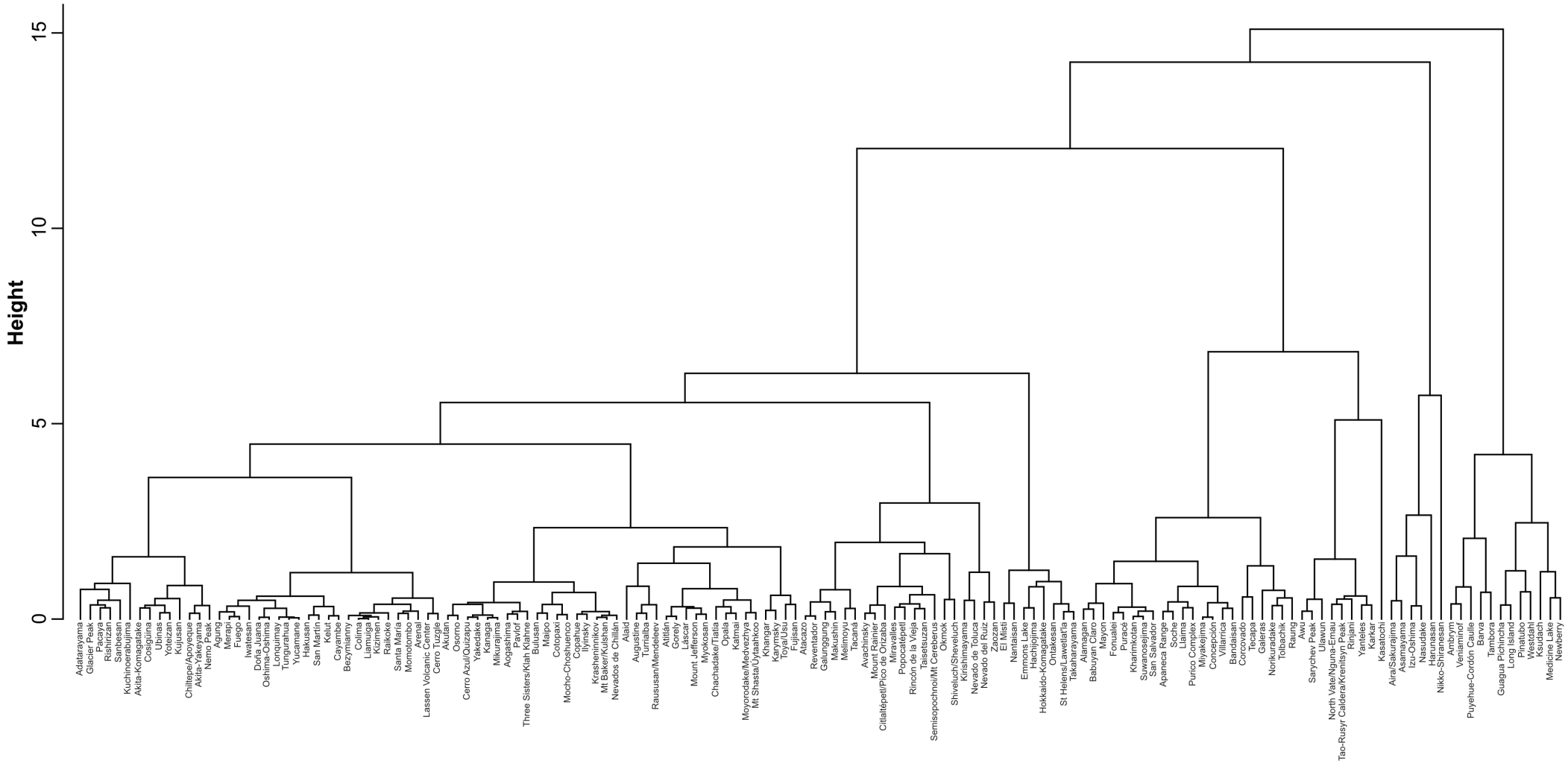

Figure 4.6 Dendrogram generated from agglomerative hierarchical clustering using Ward's linkage method to Dataset 2.

4.4 Discussion

4.4.1 Criteria for volcanoes with large-magnitude eruption potential

Our classification model identifies three key features—the number of Pleistocene eruptions, the SiO_2 95th percentile range, and the basal volcano area—that could serve as key criteria for predicting which volcanoes are likely to produce large-magnitude eruptions. The true positive classifications suggest that greater geochemical variability, along with larger and more mature volcanoes, contribute to such eruptions. An analysis was performed using the true positive volcanoes to examine the classifier's sensitivity to errors related to basal areas and SiO_2 ranges. We applied a 20% error margin to both features to account for subjectivity in defining basal areas (e.g., Grosse et al., 2014) and the number of samples used for each SiO_2 range calculation. The total number of Pleistocene eruptions was fixed, even though records for most volcanoes are likely incomplete; this incompleteness makes it difficult to estimate a rough error margin. The analysis indicates that <3% of true positives were misclassified, with these misclassifications attributed to lower basal areas and/or SiO_2 ranges (Supplementary Table 4.2), which also explains the misclassification of the false negatives (Table 4.4).

Large volumes of magma must accumulate to generate eruptions capable of ejecting vast amounts of tephra (>100 km³), which can only occur when magma injection rates are high (Caricchi et al., 2014). Thermal modelling of stochastic magma injection into the crust by Weber and Sheldrake (2022) shows that broad compositional ranges (i.e., larger SiO_2 95th percentile ranges) at arc volcanoes can be associated with elevated magma fluxes. High magma injection rates promote the formation of large silicic mushes, leading to greater temperature heterogeneity and more vertically extensive plumbing systems (Weber and Sheldrake, 2022). The

morphology of a volcano can also be used to indicate long-term magmatic fluxes; a geophysical survey compilation (i.e., seismic, magnetotelluric, geodetic) of 56 arc volcanoes shows that magma reservoirs tend to be laterally offset, with the size of the edifice inversely correlated to the extent of reservoir offset (Lerner et al., 2020). Volcanoes with smaller edifices tend to have larger calculated lateral offsets of their magma reservoirs, indicating that small volcanoes are likely low-flux or thermally immature systems (Lerner et al., 2020). Arc volcanoes with larger edifice volumes suggest systems characterised by high magma fluxes or long histories of volcanism, making them more likely to overprint upper crustal heterogeneities through repeated cycles of heating, changes in deviatoric stress, and magma intrusion (e.g., Karlstrom et al., 2017), resulting in spatially extensive yet centralised magmatic systems (Lerner et al., 2020). This is consistent with true positive classifications, such as Newberry, Gorely, and Okmok, which have minimal lateral offset of magma reservoirs (Lerner et al., 2020). Although the classifier uses basal area rather than edifice volume, the two variables are correlated (R^2=0.66). Table 4.1 also indicates that 50% of the top ten features used during the recursive feature elimination runs relate to edifice morphology. While the algorithm has recognised basal area as a key feature, it may not be an absolute causal factor for large-magnitude eruptions. However, the algorithm has identified an overarching pattern involving larger edifice morphologies, which can be linked more broadly to geochemical variance, higher magma fluxes, long-lived magmatic systems and eruptive magnitude (e.g., Caricchi et al., 2014; Karakas et al., 2017; Weber and Sheldrake, 2022; Higgins and Caricchi, 2023).

The classifier features align with two criteria (i.e., high magma supply and large, mature stratovolcanoes) proposed by Newhall et al. (2018) for identifying potential

volcano candidates, with 51% of the true positive classifications corresponding to volcanoes included in their suggested list (Figure 4.7). However, the classifier also identifies volcanoes capable of M≥6 eruptions, even if there are no prior records of

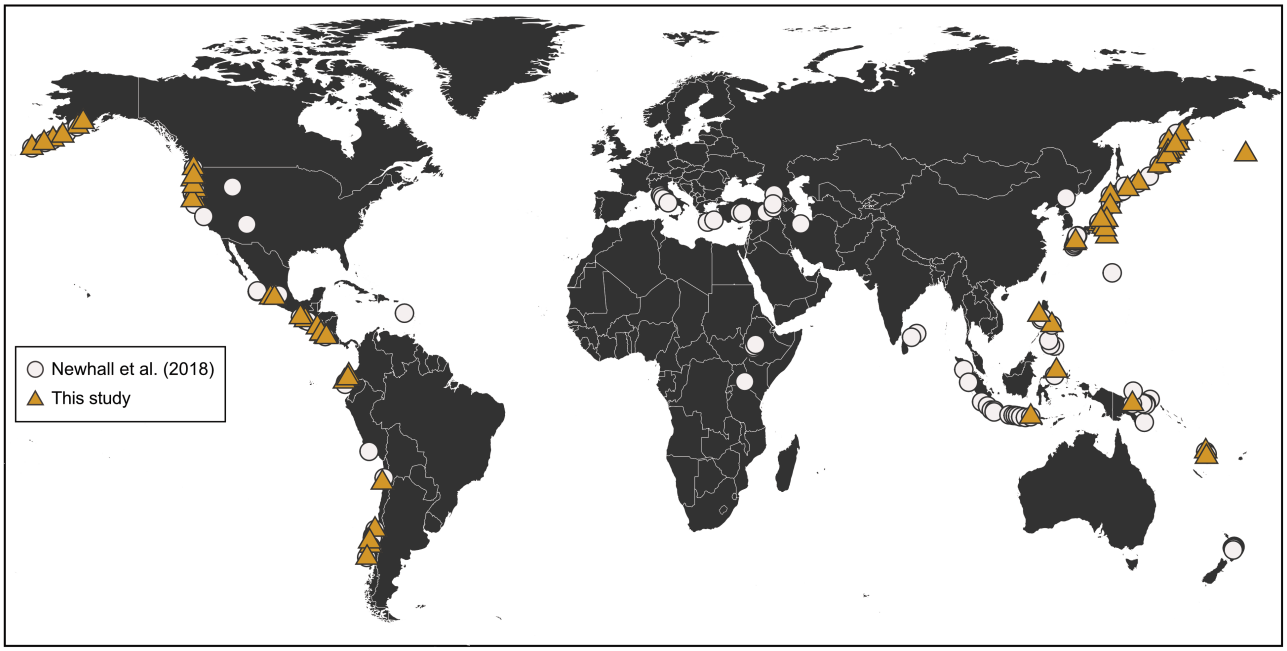

Figure 4.7 Distribution of volcanoes with the potential for large-magnitude eruptions identified from Newhall et al. (2018; grey circles) and this study (yellow triangles). The yellow triangles display the true positive volcanoes from the classifier and their analogues derived from hierarchical clustering.

such eruptions (i.e., false positives), as they exhibit similar traits to the true positives of large geochemical variability (mean 18 wt.% SiO_2 range) and mature volcanic systems (>2 Pleistocene eruptions). Although there is a tendency to monitor volcanoes that have previously had M≥6 eruptions, monitoring should prioritise updating edifice morphometric data to account for any significant changes associated with the lateral collapse of an edifice (McGuire, 2003). In addition, increasing sampling will help to evaluate the geochemical variability of data-limited volcanoes. Both will enable more accurate estimates of the spatial distribution and volume of underlying magma storage for a given volcano.

4.4.2 Analogue volcanoes

According to our hierarchical clustering dendrogram, Medicine Lake is the best analogue for Newberry Volcano. We compare the results of the cluster analysis to the top analogue obtained from PyVOLCANS (Tierz et al., 2019; Tierz et al., 2021). PyVOLCANS combines five weighted criteria of tectonic setting, rock geochemistry, eruption size, and eruption style from the GVP database, alongside volcano morphometry from the Grosse et al. (2014) and Pike and Clow (1981) databases to attain an analogy metric. This metric is then used to assess the similarity between volcanic systems in the PyVOLCANS database and the target volcano. Using an equal weighting for the PyVOLCANS criteria, Medicine Lake emerges as the top analogue for Newberry Volcano. In this case, despite using different parameters to identify analogues, both PyVOLCANS and our hierarchical clustering approach have the exact top analogue. Medicine Lake is a shield-shaped composite volcano in the Cascades arc, located ~330 km away from Newberry. Both volcanoes share similar basal areas (~560 km^2) and SiO_2 ranges (~25 wt.%; Supplementary Table 4.1).

Additionally, the LaMEVE database records 4 Pleistocene eruptions for Newberry and 2 for Medicine Lake. The most recent eruptions at Newberry and Medicine Lake are both obsidian lava flows that occurred 1300 and 900 years ago, respectively (MacLeod and Sherrod, 1988; Donnelly-Nolan et al., 1990). The USGS National Volcanic Threat Assessment classified Newberry as a "Very High Threat," while Medicine Lake is considered a "High Threat"; both pose risks to populations of <200,000 within 100 km, as well as to aviation (Donnelly-Nolan et al., 2011; Ewert et al., 2018). This example demonstrates how integrating the results of a supervised classifier with unsupervised hierarchical clustering can establish a framework for identifying volcanoes with the potential for M≥6 eruptions. This approach has been successful, as it has reaffirmed the outcomes of previous studies (e.g., Weber and Sheldrake, 2022; Newhall et al., 2018) and identified the primary proxies (e.g., geochemical variability, edifice morphology) that future studies should focus on, especially at data-limited volcanoes. Although PyVOLCANS has a larger dataset (n_{total} = 1432) for detecting analogues, the hierarchical clustering analysis allows more effective tailoring of input parameters. By using the top three features identified from recursive feature elimination, this method enables clustering of volcanoes that may share similar magmatic system configurations. Overall, 79% of the analogues for the true positive volcanoes are included in either the true positive or false positive volcano lists (Supplementary Table 4.3). The quantitative and objective nature of classification and clustering has also identified potential volcanoes (i.e., true positives and analogues) that correspond to 22% of the arc volcanoes compiled by Newhall et al. (2018; n_{total} = 112) based on expert knowledge. Further work could explore our volcano compilation (Supplementary Table 4.3) and investigate eruption frequency-magnitude relationships to fine-tune the list.

One significant limitation of this classifier and hierarchical clustering approach is the small size of the input dataset, resulting from removing features with missing values. Even after using recursive feature elimination to reduce the number of variables to three, many volcanoes could not be included within the dataset due to limited or no whole-rock data available to calculate SiO_2 95th percentile ranges. Even if the dataset incorporates additional parameters like magmatic water or crystallinity content, which have been linked to explosive eruptions (Popa et al., 2021; Castruccio et al., 2025), it will remain limited in size. Future work should focus on identifying an input dataset that maximises both the number of variables and the number of volcanoes. This will optimise recursive feature elimination to refine the list of the most important factors contributing to M≥6 eruptions and likely improve the overall classifier metrics. In addition, having a larger dataset will help evaluate the classifier more robustly by creating an independent test set that is isolated during the model training and validation stages. This test set helps assess how the model performs on new, unseen data and avoids overconfidence in the model, which can happen if the test dataset is used at any stage of model tuning (e.g., Wujek et al., 2016).

4.5 Conclusions

We have developed a classifier to predict whether an arc volcano has experienced an M≥6 eruption. Recursive feature elimination identified three essential features—the number of Pleistocene eruptions, SiO_2 95th percentile range, and basal volcano area—for building an optimal classifier, as well as key criteria for identifying potential M≥6 eruption volcanoes. Further cross-validation and testing using two ensemble classification algorithms (random forest and gradient-boosting machine)

revealed that the gradient-boosting machine algorithm yields the best model (test set accuracy: 0.70, precision: 0.67). The true positive volcano classifications (n_{total} = 43; Table 4.2) from the test sets suggest that greater geochemical variability, along with larger and more mature volcanic systems, could act as proxies for the size, distribution and thermal maturity of underlying magmatic systems (Karakas et al., 2017; Weber and Sheldrake, 2022; Lerner et al., 2020). An unsupervised hierarchical clustering analysis was also performed to identify relevant analogues for the true positive volcanoes, resulting in a total list of 64 volcanoes (e.g., Newberry and Medicine Lake; Supplementary Table 4.3) that could be further investigated to improve short-term eruption forecasting and hazard assessments.

References

Aitchison, J. (1982). The statistical analysis of compositional data. *Journal of the Royal Statistical Society: Series B (Methodological), 44*(2), 139-160. DOI: https://doi.org/10.1111/j.2517-6161.1982.tb01195.x

Biau, G., Cadre, B., & Rouvière, L. (2019). Accelerated gradient boosting. *Machine Learning*, *108*, 971-992. DOI: https://doi.org/10.1007/s10994-019-05787-1

Brown, S. K., Crosweller, H. S., Sparks, R. S. J., Cottrell, E., Deligne, N. I., Guerrero, N. O., ... & Takarada, S. (2014). Characterisation of the Quaternary eruption record: analysis of the Large Magnitude Explosive Volcanic Eruptions (LaMEVE) database. *Journal of Applied Volcanology, 3*, 1-22. DOI: https://doi.org/10.1186/2191-5040-3-5

Burgos, V., Jenkins, S. F., Bono Troncoso, L., Perales Moya, C. V., Bebbington, M., Newhall, C., ... & Taisne, B. (2023). Identifying analogues for data-limited volcanoes using hierarchical clustering and expert knowledge: a case study of Melimoyu (Chile). *Frontiers in Earth Science, 11*, 1144386. DOI: https://doi.org/10.3389/feart.2023.1144386

Caricchi, L., Annen, C., Blundy, J., Simpson, G., & Pinel, V. (2014). Frequency and magnitude of volcanic eruptions controlled by magma injection and buoyancy. *Nature Geoscience, 7*(2), 126-130. DOI: https://doi.org/10.1038/ngeo2041

Cassidy, M., & Mani, L. (2022). Huge volcanic eruptions: time to prepare. *Nature, 608*(7923), 469-471. DOI: https://doi.org/10.1038/d41586-022-02177-x

Castruccio, A., Rebolledo, A., & Gómez, I. (2025). The influence of melt composition, temperature, crystallinity and water content on eruptive style and eruption rate: Insights from a conduit model of magma ascent. *Journal of Geophysical Research: Solid Earth*, *130*(6), e2024JB030599. DOI: https://doi.org/10.1029/2024JB030599

Colombier, M., Wadsworth, F. B., Scheu, B., Vasseur, J., Dobson, K. J., Cáceres, F., ... & Dingwell, D. B. (2020). In situ observation of the percolation threshold in

multiphase magma analogues. *Bulletin of volcanology*, *82*(4), 32. DOI: https://doi.org/10.1007/s00445-020-1370-1

Crosweller, H. S., Arora, B., Brown, S. K., Cottrell, E., Deligne, N. I., Guerrero, N. O., Hobbs, L., Kiyosugi, K., Loughlin, S. C., Lowndes, J., Nayembil, M., Siebert, L., Sparks, R. S. J., Takarada, S., & Venzke, E. (2012). Global database on large magnitude explosive volcanic eruptions (LaMEVE). *Journal of Applied Volcanology*, *1*(1). DOI: https://doi.org/10.1186/2191-5040-1-4

Donnelly-Nolan, J. M., Stovall, W. K., Ramsey, D. W., Ewert, J. W., & Jensen, R. A. (2011). *Newberry Volcano—Central Oregon's Sleeping Giant* (No. 2011-3145). US Geological Survey.

Elliott, T. (2003). Tracers of the slab. *Geophysical Monograph-American Geophysical Union*, *138*, 23-46.

Ewert, J. W., Diefenbach, A. K., & Ramsey, D. W. (2018). *2018 update to the US Geological Survey national volcanic threat assessment* (No. 2018-5140). US Geological Survey.

Freire, S., Florczyk, A. J., Pesaresi, M., & Sliuzas, R. (2019). An improved global analysis of population distribution in proximity to active volcanoes, 1975–2015. *ISPRS International Journal of Geo-information, 8*(8), 341. DOI: https://doi.org/10.3390/ijgi8080341

Greenwell, B., Boehmke, B., Cunningham, J., Developers, G. B. M., & Greenwell, M. B. (2019). Package 'gbm'. R package version, 2(5). DOI: https://citeseerx.ist.psu.edu/document?repid=rep1&type=pdf&doi=4a4fc4fe7ecc5e333c227b56ce4dfccbd34a91d3

Grosse, P., Euillades, P. A., Euillades, L. D., & Van Wyk de Vries, B. (2014). A global database of composite volcano morphometry. *Bulletin of Volcanology, 76*, 1-16. DOI: https://doi.org/10.1007/s00445-013-0784-4

Grosse, P., & Kervyn, M. (2018). Morphometry of terrestrial shield volcanoes. *Geomorphology, 304*, 1-14. DOI: https://doi.org/10.1016/j.geomorph.2017.12.017

Hayes, G. P., Moore, G. L., Portner, D. E., Hearne, M., Flamme, H., Furtney, M., & Smoczyk, G. M. (2018). Slab2, a comprehensive subduction zone geometry model. *Science, 362*(6410), 58-61. DOI: https://doi.org/10.1126/science.aat4723

Heuret, A. (2006). *Dynamique des zones de subduction: étude statistique globale et approche analogique* (Doctoral dissertation, Université Montpellier II-Sciences et Techniques du Languedoc).

Higgins, O., & Caricchi, L. (2023). Eruptive dynamics reflect crustal structure and mantle productivity beneath volcanoes. *Geology, 51*(11), 1007-1010. DOI: https://doi.org/10.1130/G51355.1

Jordan, M. I., & Mitchell, T. M. (2015). Machine learning: Trends, perspectives, and prospects. *Science*, *349*(6245), 255-260.

Karakas, O., Degruyter, W., Bachmann, O., & Dufek, J. (2017). Lifetime and size of shallow magma bodies controlled by crustal-scale magmatism. *Nature Geoscience, 10*(6), 446-450. DOI: https://doi.org/10.1038/ngeo2959

Karlstrom, L., Paterson, S. R., & Jellinek, A. M. (2017). A reverse energy cascade for crustal magma transport. *Nature Geoscience, 10*(8), 604-608. DOI: https://doi.org/10.1038/ngeo2982

Kaufman, L., and Rousseeuw, P. J. (1991). “Chapter 5: Agglomerative nesting (program AGNES),” in Finding groups in data: An introduction to cluster analysis (John Wiley & Sons), 199–252.

Kuhn, M. (2008). Building predictive models in R using the caret package. *Journal of statistical software, 28*, 1-26. DOI: https://doi.org/10.18637/jss.v028.i05

Lallemand, S., Heuret, A., & Boutelier, D. (2005). On the relationships between slab dip, back-arc stress, upper plate absolute motion, and crustal nature in subduction zones. *Geochemistry, Geophysics, Geosystems, 6*(9). DOI: https://doi.org/10.1029/2005GC000917

Laske, G., Masters, G., Ma, Z., & Pasyanos, M. (2013, April). Update on CRUST1. 0—A 1-degree global model of Earth's crust. In *Geophysical Research Abstracts* (Vol. 15, No. 15, p. 2658).

Lawson, R. G., & Jurs, P. C. (1990). New index for clustering tendency and its application to chemical problems. *Journal of Chemical Information and Computer Sciences*, *30*(1), 36–41. DOI: https://doi.org/10.1021/ci00065a010

Lerner, A. H., O'Hara, D., Karlstrom, L., Ebmeier, S. K., Anderson, K. R., & Hurwitz, S. (2020). The prevalence and significance of offset magma reservoirs at arc volcanoes. *Geophysical Research Letters, 47*(14), e2020GL087856. DOI: https://doi.org/10.1029/2020GL087856

Loughlin, S. C., Sparks, R. S. J., Brown, S. K., Jenkins, S. F., & Vye-Brown, C. (Eds.). (2015). *Global volcanic hazards and risk.* Cambridge University Press.

Louppe, G., Wehenkel, L., Sutera, A., & Geurts, P. (2013). Understanding variable importances in forests of randomized trees. *Advances in Neural Information Processing Systems, 26*.

Luan, J., Zhang, C., Xu, B., Xue, Y., & Ren, Y. (2020). The predictive performances of random forest models with limited sample size and different species traits. *Fisheries Research*, *227*, 105534. DOI: https://doi.org/10.1016/j.fishres.2020.105534

Lubbers, J., Loewen, M., Wallace, K., Coombs, M., & Addison, J. (2023). Probabilistic source classification of large tephra producing eruptions using supervised machine learning: An example from the Alaska-Aleutian arc.

Geochemistry, Geophysics, Geosystems, 24(11), e2023GC011037. DOI: https://doi.org/10.1029/2023GC011037

Mani, L., Tzachor, A., & Cole, P. (2021). Global catastrophic risk from lower magnitude volcanic eruptions. *Nature Communications*, *12*(1). DOI: https://doi.org/10.1038/s41467-021-25021-8

MacLeod, N. S., & Sherrod, D. R. (1988). Geologic evidence for a magma chamber beneath Newberry Volcano, Oregon. *Journal of Geophysical Research: Solid Earth, 93*(B9), 10067-10079. DOI: https://doi.org/10.1029/JB093iB09p10067

McCormick, M. P., Thomason, L. W., & Trepte, C. R. (1995). Atmospheric effects of the Mt Pinatubo eruption. *Nature, 373*(6513), 399-404. DOI: https://doi.org/10.1038/373399a0

McGuire, W. J. (2003). Volcano instability and lateral collapse. *Revista, 1,* 33-45.

Nooren, K., Hoek, W. Z., van Der Plicht, H., Sigl, M., van Bergen, M. J., Galop, D., ... & Middelkoop, H. (2017). Explosive eruption of El Chichón volcano (Mexico) disrupted 6th century Maya civilization and contributed to global cooling. *Geology, 45*(2), 175-178. DOI: https://doi.org/10.1130/G38739.1

Newhall, C., Self, S., & Robock, A. (2018). Anticipating future Volcanic Explosivity Index (VEI) 7 eruptions and their chilling impacts. *Geosphere, 14*(2), 572-603. DOI: https://doi.org/10.1130/GES01513.1

Oppenheimer, J., Rust, A. C., Cashman, K. V., & Sandnes, B. (2015). Gas migration regimes and outgassing in particle-rich suspensions. *Frontiers in Physics*, *3*, 60. DOI: https://doi.org/10.3389/fphy.2015.00060

Parker, D. E., Wilson, H., Jones, P. D., Christy, J. R., & Folland, C. K. (1996). The impact of Mount Pinatubo on world-wide temperatures. *International Journal of Climatology: A Journal of the Royal Meteorological Society, 16*(5), 487-497. DOI: https://doi.org/10.1002/(SICI)1097-0088(199605)16:5<487::AID-JOC39>3.0.CO;2-J

Petrelli, M. (2024). Machine learning in petrology: state-of-the-art and future perspectives. *Journal of Petrology*, *65*(5), egae036. DOI: https://doi.org/10.1093/petrology/egae036

Pike, R. J., & Clow, G. D. (1981). *Revised classification of terrestrial volcanoes and catalog of topographic dimensions, with new results of edifice volume* (No. 81-1038). US Geological Survey.

Popa, R. G., Bachmann, O., & Huber, C. (2021). Explosive or effusive style of volcanic eruption determined by magma storage conditions. *Nature Geoscience*, *14*(10), 781-786. DOI: https://doi.org/10.1038/s41561-021-00827-9

Pyle, D. M. (2015). Sizes of volcanic eruptions. In *The encyclopedia of volcanoes* (pp. 257-264). Academic Press.

Robinson, G. A., Peng, J., Dönnes, P., Coelewij, L., Naja, M., Radziszewska, A., ... & Jury, E. C. (2020). Disease-associated and patient-specific immune cell signatures in juvenile-onset systemic lupus erythematosus: patient stratification using a machine-learning approach. *The Lancet Rheumatology*, *2*(8), e485-e496. DOI: https://doi.org/10.1016/S2665-9913(20)30168-5

R Core Team, R. (2013). R: A language and environment for statistical computing.

Rougier, J., Sparks, R. S. J., Cashman, K. V., & Brown, S. K. (2018). The global magnitude–frequency relationship for large explosive volcanic eruptions. *Earth and Planetary Science Letters, 482*, 621-629. DOI: https://doi.org/10.1016/j.epsl.2017.11.015

Singer, B. S., Jicha, B. R., Leeman, W. P., Rogers, N. W., Thirlwall, M. F., Ryan, J., & Nicolaysen, K. E. (2007). Along-strike trace element and isotopic variation in Aleutian Island arc basalt: Subduction melts sediments and dehydrates serpentine. *Journal of Geophysical Research: Solid Earth*, *112*(B6). DOI: https://doi.org/10.1029/2006JB004897

Stocker, M., Steiner, A. K., Ladstädter, F., Foelsche, U., & Randel, W. J. (2024). Strong persistent cooling of the stratosphere after the Hunga eruption. *Communications Earth & Environment, 5*(1), 450. DOI: https://doi.org/10.1038/s43247-024-01620-3

Talekar, B., & Agrawal, S. (2020). A detailed review on decision tree and random forest. *Bioscience Biotechnology Research Communications*, *13*(14), 245-248.

Tesauro, M., Kaban, M. K., & Cloetingh, S. A. (2012). Global strength and elastic thickness of the lithosphere. *Global and Planetary Change, 90*, 51-57. DOI: https://doi.org/10.1016/j.gloplacha.2011.12.003 s

Tierz, P., Loughlin, S. C., & Calder, E. S. (2019). VOLCANS: an objective, structured and reproducible method for identifying sets of analogue volcanoes. *Bulletin of Volcanology, 81*, 1-22. DOI: https://doi.org/10.1007/s00445-019-1336-3

Tierz, P., Christodoulou, V., Stevenson, J. A., & Loughlin, S. (2021). PyVOLCANS: A Python package to flexibly explore similarities and differences between volcanic systems. *Journal of Open Source Software, 6*(68). DOI: https://doi.org/10.21105/joss.03649

Wang, H., Fu, T., Du, Y., Gao, W., Huang, K., Liu, Z., ... & Zitnik, M. (2023). Scientific discovery in the age of artificial intelligence. *Nature*, *620*(7972), 47-60. DOI: https://doi.org/10.1038/s41586-023-06221-2

Ward Jr, J. H. (1963). Hierarchical grouping to optimize an objective function. *Journal of the American Statistical Association, 58*(301), 236-244. DOI: https://doi.org/10.1080/01621459.1963.10500845

Wright, M. N., & Ziegler, A. (2017). ranger: A fast implementation of random forests for high dimensional data in C++ and R. *Journal of Statistical Software, 77*(1), 1–17. DOI: https://doi.org/10.18637/jss.v077.i01

Weber, G., & Sheldrake, T. E. (2022). Geochemical variability as an indicator for large magnitude eruptions in volcanic arcs. *Scientific Reports, 12*(1), 15854. DOI: https://doi.org/10.1038/s41598-022-19902-1

Wujek, B., Hall, P., & Günes, F. (2016). Best practices for machine learning applications. *SAS Institute Inc*, *3*.

5 | Conclusions and future work

5.1 Machine learning-based thermobarometric and hygrometric models

Chapter Two explored whether existing plagioclase-based thermobarometry, hygrometry, and plagioclase-melt equilibria models could be refined using random forest machine learning. Cross-validation RMSE values suggest we can estimate the intensive variables (T-H_2O-P) of plagioclase-saturated magmas exclusively from the melt composition rather than using both plagioclase and melt compositions, as the variable importance shows that the models predominantly use melt oxides to predict the target variables. To initially use the models, a classifier to test for plagioclase saturation was calibrated, as this model provides a minimum criterion to ensure the input data is appropriate for the subsequent (T/H_2O/P/An) models. The melt input data can also be compared with calibration data in the R script or web application to verify whether the models will yield adequate values for the given melt composition. The test set RMSEs for the T/H_2O-dependent and melt-only models are 25–35 °C, 0.65–1.00 wt.%, and 74–88 MPa for temperature, water content and pressure, respectively. Overall, the T/H_2O/P models offer improved prediction accuracy compared to earlier plagioclase-based thermometers, hygrometers, and barometers, providing estimates that can complement independent estimates when available or work in conjunction with other mineral-based thermobarometers/hygrometers to construct a comprehensive magma storage model for a given magmatic system. Furthermore, the melt-only models allow T/H_2O/P predictions to be made without additional independent constraints, which can often introduce further uncertainties if not propagated – this is particularly the case with previous plagioclase-melt hygrometers (Masotta et al., 2019; Waters et al., 2015). The anorthite content model, which estimates the equilibrium anorthite content in plagioclase, also demonstrates

good performance with a test set RMSE of 5.8 mol%. The main advantage of this model over previous anorthite content models is that it allows for easy calculation of equilibrium anorthite contents using inputs from either hydrous or anhydrous melts. The new models were applied to two case studies from different tectonic settings (Mount St Helens, USA; Bárðarbunga, Iceland), and all estimates are consistent with previous petrological and geophysical estimates. These case studies were selected to illustrate potential ways to use the models with the data accessible to the users. The case studies were also chosen due to the various independent P-T-H_2O estimates and plagioclase compositional data available, which provide a baseline for comparison to test the machine learning models' efficacy. Although the machine learning models' estimates align with previous estimates from various thermobarometric/hygrometric models, melt inclusion analyses, and geophysical methods, testing these models on a broader set of case studies with independent P-T-H_2O estimates is essential. This would help identify which types of systems and conditions yield the most accurate petrological estimates and reveal other potential shortcomings to consider when applying the models (e.g., Wieser et al., 2023). Based on the calibration data, the current models may have difficulty predicting P-T-H_2O-An estimates for tholeiitic volcanic deposits, as well as water and pressure estimates for deposits with records of low water content and high pressures (>300 MPa).

The melt thermometers and hygrometers can be applied to various plagioclase-bearing melts across temperatures of 664–1355°C and water contents of <11.20 wt.%. However, the melt barometers can only be applied to pressures of ≤500 MPa. Chapter Two has shown that we can refine models to a point; however, their effectiveness depends on the quality of the experimental data for calibration. The

compilation of experiments (Figure 2.1) to calibrate the melt models highlights evident discrepancies that necessitate additional experimental work before any further calibration of thermobarometric or hygrometric models can proceed. There is an overabundance of data for barometry at 200 MPa and 1 atm; a series of systematic phase equilibrium experiments at higher pressures between 500 and 1000 MPa would help to improve models substantially, as highlighted by the Subduction Zones in Four Dimensions (SZ4D) initiative (Hilley et al., 2022). In addition, increasing the number of H_2O analyses from low-crystallinity glasses of hydrous experimental runs with independent methods such as FTIR, Raman, or SIMS would refine hygrometry calibrations, as much of the calibration data relies on water content estimates from solubility models. Increasing H_2O analyses to 'anhydrous' experimental runs would also be beneficial, as small amounts of dissolved water can significantly affect liquidus temperatures and phases (e.g. Médard and Grove, 2008). An additional avenue for future research could be to build upon models that incorporate thermodynamic relationships (e.g., hygrometer; Waters and Lange, 2015). However, this will also require additional experiments to acquire updated values for the thermodynamic parameters of albite and anorthite. Machine learning could then be used to identify experiments that are more likely to be in or close to equilibrium.

5.2 Using plagioclase as a NAM hygrometer

Chapter Three looked at conducting hydrogen plagioclase-melt partitioning experiments to determine new partition coefficients for silicic melts. Experiments were performed in cold seal pressure vessels at 780–850 °C under low pressures (<200 MPa) and variable water contents (<6.0 wt.%) using a haplogranitic starting

material. A difficult aspect of this study was producing large enough plagioclase crystals for analysis, so instead, plagioclase seeds were used. Future experiments looking to replicate similar conditions may benefit from using pre-hydrated charges (Da Silva et al., 2017) for longer experimental durations (i.e., 14 to 21 days) to enable analysis of grown plagioclase crystals, as well as the seeds. From analysing the haplogranitic experimental products and a set of rhyolitic phase-equilibrium experiments from Madden-Nadeau (2022), the resulting hydrogen partition coefficients range from 0.002 to 0.008 (± 0.001). H_2O concentrations in plagioclase from partitioning and solubility experiments show a reasonable dependence on water fugacity using a power-law relation (R^2=0.74):

$$C_{H_2O}^{plagioclase} = 51.26 \cdot fH_2O^{0.20} \quad (1)$$

However, to determine melt water concentrations, an independent constraint on XH_2O or pressure is required. An alternative equation was developed, since the new hydrogen partition coefficients combined with other experimental coefficients from the literature show a strong dependence on the H_2O content in the melt (R^2=0.95, Equation 2), resulting in non-Henrian behaviour between H_2O concentrations in plagioclase and the melt.

$$D_{H_2O}^{plagioclase/melt} = 0.0071 \cdot {C_{H_2O}^{melt}}^{-0.80} \quad (2)$$

This can be rearranged into a new H^+-in-plagioclase hygrometer:

$$C_{H_2O}^{melt} = \left(\frac{C_{H_2O}^{plagioclase}}{0.0071}\right)^5 \quad (3)$$

which can be applied to lunar and terrestrial calc-alkaline melts for melt water contents between 0.005 and 6.0 wt.%.

This hygrometer was applied to plagioclase grains from Plinian dacitic deposits of Cerro Machín (Castilla et al., 2024), returning equilibrium melt H_2O contents of 6.4–12.2 $\pm$ 0.4 wt.%. Even though the hygrometer was applied outside of the calibration range, the calculated estimates are consistent with those from other H^+-in-plagioclase hygrometers (Castilla et al., 2024; Mosenfelder et al., 2020), plagioclase- and quartz-hosted melt inclusion data (Castilla et al., 2024), and T-independent melt hygrometry presented in Chapter Two. Overall, the water estimates derived from plagioclase crystals and melt inclusions, along with the presence of high-forsterite olivine and high-Mg# amphibole, suggest that the Cerro Machín system is very hydrous, akin to systems in the Andean magmatic arc (e.g., Laumonier et al., 2017). Although Equation 3 provides an updated H^+-in-plagioclase hygrometer that extends the calibration range to silicic melts, its high sensitivity highlights a significant limitation to using hydrogen in plagioclase as a hygrometer. The method requires precise water measurements, which are more likely to be achieved using SIMS; however, new sets of plagioclase standards need to be developed. As a technique in mass spectrometry, SIMS relies on standards with known water concentrations to precisely determine the absolute water content of unknown samples. Matrix-matched standards should be used whenever possible, as the chemical composition and physical structure of the substrate can greatly influence the ionisation of various elements by the primary ion beam (e.g., Hauri et al., 2002). Not only would establishing new standards provide more accurate and precise hydrogen

calibrations, but it would also make the analysis of plagioclase crystals using SIMS more widely accessible. A compositional range of homogeneous plagioclase crystals needs to be analysed using various techniques similar to the work of Kunamoto et al. (2017), including SIMS and FTIR, as well as independent methods (e.g., manometry) to ensure that all absolute values are equal within error. In addition to improving plagioclase standards, conducting further partitioning experiments would reaffirm whether Equations 5 and 7 from Chapter Three adequately explain partitioning behaviour. FTIR analysis of the experimental products would also help to confirm the speciation of H^+ in plagioclase and could shed light on the mechanisms of H^+ incorporation.

5.3 Refining volcano candidates for future large-magnitude eruptions

Chapter Four developed a classifier to predict whether an arc volcano has experienced an M≥6 eruption in order to investigate the factors contributing to the occurrence of large-magnitude eruptions. Recursive feature elimination identified three features from a total of 22 for developing an optimal classifier with the highest accuracy, as well as potential criteria for identifying volcanoes that could produce an eruption of M≥6. These features are the number of Pleistocene eruptions, the 95th percentile range of SiO_2, and the basal area of a volcano. This is consistent with the findings of previous studies that did not use machine learning methods (Newhall et al., 2018; Weber and Sheldrake, 2022). After reducing the number of variables to three, further cross-validation and testing by comparing two ensemble classification algorithms (random forests and gradient boosting) show that gradient boosting produces the most effective model, with a test set accuracy of 70%. The correctly classified volcanoes (i.e., true positives; n_{total} = 43) from the test sets suggest that

larger, more mature volcanic systems displaying greater geochemical variability could serve as proxies for the size, distribution, and thermal maturity of underlying magmatic systems (Karakas et al., 2017; Weber and Sheldrake, 2022; Lerner et al., 2020). A hierarchical clustering analysis was also performed to identify analogues for the true positive volcanoes. This generated a combined list of 64 volcanoes, taken from the true positive volcano list and clustering, which could be explored further to improve short-term eruption forecasting and hazard assessments.

The main limitation of the classifier is the small dataset size. One of the key proxies identified by the classifier was the SiO_2 95^{th} percentile range; therefore, further efforts to establish tephra stratigraphies and increase sampling would assist in calculating robust geochemical variance estimates. Other useful parameters to include are variance estimates of volatile content, especially H_2O, and crystallinity content, as they are linked to conditions favouring explosive eruptions (e.g., Popa et al., 2021). Improving global datasets of these parameters will help build a dataset that maximises the number of volcanoes and variables, which will improve the results of recursive feature elimination. Once an optimal dataset is identified, subsequent research could explore additional algorithms (e.g., support vector machine; Pisner and Schnyer, 2020) to improve classifier performance. A larger dataset will also be crucial for effectively evaluating the classifier on unseen data using an independent test set derived from the original input dataset, which is not involved in model training or validation (e.g., Tampu et al., 2022).

References

Castilla, S. C., Newcombe, M. E., Piccoli, P. M., & Peterson, L. D. (2024). Crystals and melt inclusions record deep storage of superhydrous magma prior to the largest known eruption of Cerro Machín volcano, Colombia. *Journal of Petrology*, *65*(9), egae095. DOI: https://doi.org/10.1093/petrology/egae095

Da Silva, M. M., Holtz, F., & Namur, O. (2017). Crystallization experiments in rhyolitic systems: The effect of temperature cycling and starting material on crystal size distribution. *American Mineralogist: Journal of Earth and Planetary Materials, 102*(11), 2284-2294. DOI: https://doi.org/10.2138/am-2017-5981

Hauri, E., Wang, J., Dixon, J. E., King, P. L., Mandeville, C., & Newman, S. (2002). SIMS analysis of volatiles in silicate glasses: 1. Calibration, matrix effects and comparisons with FTIR. *Chemical Geology*, *183*(1-4), 99-114. DOI: https://doi.org/10.1016/S0009-2541(01)00375-8

Hilley, G. E., Brodsky, E. E., Roman, D., Shillington, D. J., Brudzinski, M., Behn, M., et al. (2022). SZ4D implementation plan. Stanford digital repository.

Karakas, O., Degruyter, W., Bachmann, O., & Dufek, J. (2017). Lifetime and size of shallow magma bodies controlled by crustal-scale magmatism. *Nature Geoscience, 10*(6), 446-450. DOI: https://doi.org/10.1038/ngeo2959

Kumamoto, K. M., Warren, J. M., & Hauri, E. H. (2017). New SIMS reference materials for measuring water in upper mantle minerals. *American Mineralogist*, *102*(3), 537-547. DOI: https://doi.org/10.2138/am-2017-5863CCBYNCND

Lallemand, S., Heuret, A., & Boutelier, D. (2005). On the relationships between slab dip, back-arc stress, upper plate absolute motion, and crustal nature in subduction zones. *Geochemistry, Geophysics, Geosystems, 6*(9). DOI: https://doi.org/10.1029/2005GC000917

Laumonier, M., Gaillard, F., Muir, D., Blundy, J., & Unsworth, M. (2017). Giant magmatic water reservoirs at mid-crustal depth inferred from electrical conductivity and the growth of the continental crust. *Earth and Planetary Science Letters*, *457*, 173-180. DOI: https://doi.org/10.1016/j.epsl.2016.10.023

Lerner, A. H., O'Hara, D., Karlstrom, L., Ebmeier, S. K., Anderson, K. R., & Hurwitz, S. (2020). The prevalence and significance of offset magma reservoirs at arc volcanoes. *Geophysical Research Letters, 47*(14), e2020GL087856. DOI: https://doi.org/10.1029/2020GL087856

Madden-Nadeau, A. L. (2021). *Silicic caldera volcanism and the 1883 eruption of Krakatau Volcano, Indonesia* (Doctoral dissertation, University of Oxford).

Médard, E., & Grove, T. L. (2008). The effect of H 2 O on the olivine liquidus of basaltic melts: experiments and thermodynamic models. *Contributions to Mineralogy and Petrology*, *155*, 417-432. DOI: https://doi.org/10.1007/s00410-007-0250-4

Mosenfelder, J. L., Andrys, J. L., von der Handt, A., Kohlstedt, D. L., & Hirschmann, M. M. (2020). Hydrogen incorporation in plagioclase. *Geochimica et Cosmochimica Acta*, *277*, 87-110. DOI: https://doi.org/10.1016/j.gca.2020.03.013

Pisner, D. A., & Schnyer, D. M. (2020). Support vector machine. In *Machine learning* (pp. 101-121). Academic Press.

Tampu, I. E., Eklund, A., & Haj-Hosseini, N. (2022). Inflation of test accuracy due to data leakage in deep learning-based classification of OCT images. *Scientific Data*, *9*(1), 580. DOI: https://doi.org/10.1038/s41597-022-01618-6

Weber, G., & Sheldrake, T. E. (2022). Geochemical variability as an indicator for large magnitude eruptions in volcanic arcs. *Scientific Reports, 12*(1), 15854. DOI: https://doi.org/10.1038/s41598-022-19902-1

Wieser, P. E., Kent, A. J., & Till, C. B. (2023). Barometers behaving badly II: a critical evaluation of Cpx-only and Cpx-Liq thermobarometry in variably-hydrous arc

magmas. *Journal of Petrology*, *64*(8), egad050. DOI: https://doi.org/10.1093/petrology/egad050